To the Graduate Council:

I am submitting herewith a thesis written by Yue Zheng entitled "X-Ray Image Processing and Visualization for Remote Assistance of Airport Luggage Screeners." I have examined the final electronic copy of this thesis for form and content and recommend that it be accepted in partial fulfillment of the requirements for the degree of Master of Science, with a major in Electrical Engineering.

Mongi Abidi

Major Professor

We have read this thesis
and recommend its acceptance:

Besma Abidi

Seong Kong

Andreas Koschan

Accepted for the Council:

Anne Mayhew

Vice Chancellor and
Dean of Graduate Studies

(Original signatures are on file with official student records.)

X-Ray Image Processing and Visualization for Remote Assistance of Airport Luggage Screeners

A Thesis
Presented for the
Master of Science
Degree
The University of Tennessee, Knoxville

Yue Zheng

December 2004

Acknowledgements

First and foremost, I would like to express my deepest appreciation to my major research advisor, Dr. Besma Abidi, for all of her help and guidance during my graduate study. Also, I would like to thank my major academic advisor, Dr. Mongi Abidi, for his support and invaluable suggestions.

Many thanks to Dr. Seong Kong and Dr. Andreas Koschan for their serving on my thesis committee, reading this thesis and providing constructive comments. In addition, I would like to thank the other faculty, staff and students in the IRIS laboratory: Dr. David Page, Dr. Andrei Gribok, Vicki Courtney-Smith, Kim Cate and Justin Acuff……who create friendly working environment, encouraging open dialogue and the sharing of ideas.

Finally, I would like to express my great gratitude to my parents Shuangcai Zheng and Wenli Hu for their continuous encouragement and support. There are no words that can show my appreciation to them for all the sacrifices they made to help me foster my lovely daughter. Last but not least, I want to thank my husband, Zhong Du, whose understanding and encouragement kept me going forward through the whole period of this study.

Abstract

X-ray technology is widely used for airport luggage inspection nowadays. However, the ever-increasing sophistication of threat-concealment measures and types of threats, together with the natural complexity, inherent to the content of each individual luggage make x-ray raw images obtained directly from inspection systems unsuitable to clearly show various luggage and threat items, particularly low-density objects, which poses a great challenge for airport screeners.

This thesis presents efforts spent in improving the rate of threat detection using image processing and visualization technologies. The principles of x-ray imaging for airport luggage inspection and the characteristics of single-energy and dual-energy x-ray data are first introduced. The image processing and visualization algorithms, selected and proposed for improving single energy and dual energy x-ray images, are then presented in four categories: (1) gray-level enhancement, (2) image segmentation, (3) pseudo coloring, and (4) image fusion. The major contributions of this research include identification of optimum combinations of common segmentation and enhancement methods, HSI based color-coding approaches and dual-energy image fusion algorithms —spatial information-based and wavelet-based image fusions. Experimental results generated with these image processing and visualization algorithms are shown and compared. Objective image quality measures are also explored in an effort to reduce the overhead of human subjective assessments and to provide more reliable evaluation results.

Two application software are developed − an x-ray image processing application (XIP) and a wireless tablet PC-based remote supervision system (RSS). In XIP, we implemented in a user-friendly GUI the preceding image processing and visualization algorithms. In RSS, we ported available image processing and visualization methods to a wireless mobile supervisory station for screener assistance and supervision.

Quantitative and on-site qualitative evaluations for various processed and fused x-ray luggage images demonstrate that using the proposed algorithms of image processing and visualization constitutes an effective and feasible means for improving airport luggage inspection.

Table of Contents

1 Introduction 1
1.1 Background 1
1.2 Motivation 2
1.3 Contributions 3
1.4 Outline of this Thesis 3
2 Literature Review 6
2.1 Physics of X-Ray Imaging 6
2.2 X-Ray Carry-On Luggage Inspection Systems 7
2.2.1 Conventional Transmission X-Ray Imaging Systems 7
2.2.2 Dual Energy X-Ray Imaging Systems 9
2.3 Image Enhancement and Segmentation 9
2.3.1 Image Enhancement 9
2.3.2 Image Segmentation 15
2.4 Pseudo Coloring 16
2.5 Image Fusion 18
2.5.1 Statistical and Numerical Fusion Methods 19
2.5.2 Multi-Resolution Fusion Methods 19
2.6 Image Quality Measures 20
2.7 Summary 21
3 Gray Level Enhancement 23
3.1 Common Gray-Level Enhancement Techniques 23
3.1.1 Linear Contrast Enhancement 23
3.1.2 Gamma Intensity Adjustment 23
3.1.3 Logarithmic Intensity Adjustment 25
3.1.4 Standard Measure Technique 25
3.1.5 Histogram Equalization 25
3.2 Screener Performance Evaluations 25
3.3 Summary 29
4 Image Segmentation 31
4.1 Image Hashing Algorithms 31
4.1.1 Equal Interval Image Slicing 31
4.1.2 Cumulative Image Slicing 31
4.1.3 H-Domes Image Slicing 34
4.2 Entropy-Based Multilevel Thresholding Approaches 34
4.2.1 The ICM Method 34
4.2.2 The Valley Method 37
4.3 Experimental Results 38
4.3.1 The ICM Method 41
4.3.2 The Valley Method 41
4.3.3 Integration of the Resulting Slices 49
4.4 Summary 49
5 Pseudo Coloring 52
5.1 Aspects of Human Visual Perception 52
5.1.1 Physiological Processing of Color 52
5.1.2 Psychological Processing of Color 53

5.1.3 General Recommendations for Optimum Color Assignment 54
5.2 Theoretical Aspects of Pseudo-Coloring 55
5.2.1 Color Spaces 55
5.2.2 Color Transforms 56
5.3 RGB-Based Color Transforms 59
5.3.1 Perceptually-Based Color Mapping 59
5.3.2 Mathematical Formulations 64
5.4 HSI Based Color Transforms 67
5.4.1 Color Directly Applied to Original Gray Scale Data 67
5.4.2 Color Mapped to Preprocessed Gray Scale Data 69
5.5 Formal Airport Evaluation 72
5.6 Summary 76
6 Dual-Energy X-Ray Image Fusion 78
6.1 Image Fusion using Local Spatial Information 78
6.1.1 Algorithm 78
6.1.2 Noise Analysis and Noise Reduction 80
6.2 Wavelet Based Image Fusion 83
6.2.1 Image Fusion with Wavelet Transform 83
6.2.2 Wavelet Based Fusion Algorithm for Dual-Energy X-Ray Images 85
6.2.3 Noise Analysis and Reduction 86
6.3 Color-Coding of Fused Images 89
6.4 Experimental Results 89
6.4.1 Image Fusion Using Local Spatial Information 89
6.4.2 Wavelet-Based Dual-Energy X-Ray Image Fusion Approach 89
6.4.3 Color Coding of Fused Images 95
6.5 Objective Evaluation of Fused Images 95
6.6 Summary 103
7 Application Software Development 104
7.1 X-ray Image Processing (XIP) 104
7.2 Wireless Tablet PC-Based Remote Supervision 104
7.2.1 Introduction 106
7.2.2 RSS Framework 106
7.2.3 Communication of Server and Client 106
7.2.4 RSS Functions 108
7.2.5 RSS GUIs 111
8 Conclusions 112
8.1 Summary of Contributions 112
8.2 Future Work 113
Bibliography 114
Vita 122

List of Tables

Table 2.1 Effects of the Decrease of Grayness Ambiguity of five fuzzy theory based algorithms. 14
Table 4.1 Initial and final states obtained for the image shown in Figure 4.6 (a) for the case of 5 classes. 42
Table 4.2 Initial and final states obtained for the image shown in Figure 4.6 (b) for the case of 5 classes. 43
Table 4.3 Initial and final states obtained for the image shown in Figure 4.6 (c) for the case of 5 classes. 44
Table 4.4 Thresholds obtained by using the Valley method to segment (a) the image shown in Figure 4.6 (a), (b) the image shown in Figure 4.6 (b), (c) the image shown in Figure 4.6 (c), for the case of 5 classes. 44
Table 6.1 Means and standard deviations of gray levels of the small region shown in Figure 6.4 (a), computed by using data from the low-energy x-ray image, the high-energy x-ray image, and the fused image generated using wavelet-based fusion method before and after noise reduction. 88

List of Figures

Figure 1.1 Image processing techniques involved in the improvement of raw x-ray luggage scans. 2
Figure 1.2 Algorithms selected and proposed (in bold) for the improvement of raw x-ray luggage scans. 4
Figure 2.1 The electromagnetic spectrum. 6
Figure 2.2 Siements-Heimann transmission x-ray imaging system 8
Figure 2.3 Example single-energy x-ray images 8
Figure 2.4 Two pairs of example dual-energy x-ray images, low-energy x-ray images (left) and high-energy x-ray images (right). 10
Figure 2.5 Block diagram of single HP channel and fixed image enhancement 12
Figure 2.6 Block diagram of multiple HP channels and adaptive image enhancement 12
Figure 3.1 Linear contrast enhancement.. 24
Figure 3.2 Gamma correction. 26
Figure 3.3 Logarithmically enhanced synthetic and x-ray scenes. 26
Figure 3.4 Standard measure technique. 27
Figure 3.5 Histogram equalization performed on (a) synthetic data and (c) x-ray data with corresponding resulting images shown in (b) and in (d), respectively. 27
Figure 3.6 (a) Snapshot of screener evaluation application, (b) binary mask of threat object in image (a) used for confirmation of threat detection. 28
Figure 3.7 Mean opinion scores (10 being best) by screeners of original image and each of the differently-processed images 30
Figure 3.8 Percent of screeners who actually detected the right threat, sorted by image type. 30
Figure 4.1 Equal interval image slicing. (a) Illustrative schematic for the equal interval image hashing algorithm, (b) result of a six-slice equal interval image hashing applied to the original image shown on top. 32
Figure 4.2 Result of six-slice cumulative image hashing of original images shown in Figure 4.1. 33
Figure 4.3 Graphical representation of the h-domes methodology. 35
Figure 4.4 Result (b) of the H-domes algorithm applied to the negative of an 8-bit original x-ray image (a) with 50 gray levels for the domes. 35
Figure 4.5 Form "*N*" on the left and form "*H*" on the right. 37
Figure 4.6 Three representative x-ray luggage scans used for segmentation. 39
Figure 4.7 Histograms of x-ray scans.. 40
Figure 4.8 Resulting slices generated by using the resulting thresholds shown in Table 4.1 for the case of 5 classes. 42
Figure 4.9 Resulting slices per class generated using the resulting thresholds shown in Table 4.2 for the case of 5 classes. 43
Figure 4.10 Resulting slices generated by using the final state of the thresholds shown in Table 4.3 for the case of 5 classes. 44
Figure 4.11 Simulated image with 5 gray level objects, 0,128, 166, 192 and 255. 45
Figure 4.12 Resulting slices per class produced by using the valley method. 45
Figure 4.13 Resulting slices produced by using the ICM method. 45
Figure 4.14 Resulting slices per class generated by using the thresholds shown in Table 4.4(a) for the case of 5 classes. 46

Figure 4.15 Resulting slices per class generated by using the thresholds shown in Table 4.4(b) for the case of 5 classes. 47
Figure 4.16 Resulting slices per class generated by using the thresholds shown in Table 4.4(c) for the case of 5 classes. 48
Figure 4.17 (a) Original image containing a low-density threat, a narrow soft wood knife, (b) color counterpart composed by using the 5 slices shown in Figure 4.8 and applying a selected color map. 49
Figure 4.18 (a) Original image containing high-density threats, gun and grenade, (b) color counterpart composed by using the 5 slices shown in Figure 4.9 and applying a selected color map. 50
Figure 4.19 (a) Original image containing various low-density knives, (b) color counterpart composed by using the 5 slices shown in Figure 4.10, (c) color counterpart composed by using 7 slices and applying a selected color map. 50
Figure 5.1 Simultaneous contrast: colors look darker and corresponding objects smaller against a white background and lighter and larger against a dark background 53
Figure 5.2 Simultaneous contrast can make (a) the same colors look different, or (b) different colors look the same. 54
Figure 5.3 General approach for color mapping of gray level images. 57
Figure 5.4 Original x-ray luggage scans containing knives made of (a) soft wood, (b) light-purple glass, and (c) aluminum. 59
Figure 5.5 (a) The "Hot" color scale and (b) the "Jet" color scale. 60
Figure 5.6 (a) R, G and B values versus gray level for the "Hot" scale, (b) R, G and B values versus gray level for the "Jet" scale. 61
Figure 5.7 Enhanced version of Figure 5.4 produced by using original + negative + h-dome + contrast stretching. 62
Figure 5.8 Colored version of Figure 5.7 generated by applying color scale "Hot". 62
Figure 5.9 Colored version of Figure 5.7 generated by applying color scale "Jet". 62
Figure 5.10 The 16-step "Warm" color scale. 63
Figure 5.11 (a) R, G and B values versus gray level obtained by linearly fitting 256 steps to the16-step scale, (b) the 256-step "Warm" color scale. 63
Figure 5.12 Colored version of Figure 5.7 generated by applying the designed color scale "Warm" shown in Figure 5.11(b). 63
Figure 5.13 Varying the number of colors using the mathematical expression of equation (5.6) for color mapping; (a) through (f) represent color maps using 4, 8, 12, 16, 64, and 256 colors respectively. 65
Figure 5.14 Colored version of Figure 5.4 generated using the sine transform. 66
Figure 5.15 (a) The rainbow color scale; (b) the three periodic functions used for the rainbow transformation. Red, green and blue curves represent the R, G, and B vs. gray level transform functions, respectively. 67
Figure 5.16 General process producing the second-subcategory of HSI-based color transforms. 68
Figure 5.17 (a) Intensity, hue and saturation transforms, (b) color scale "Springtime" produced by using the concave part (solid curve) of the semi-ellipse for the hue transform, and (c) color scale produced by using the convex part (dotted curve) of the semi-ellipse for the hue transform. 69
Figure 5.18 Colored version of Figure 5.7 generated by applying the "Springtime" color scale. 70
Figure 5.19 Colored version of Figure 5.4 generated by using color map *CS1* with constant saturation. 71

Figure 5.20 Colored version of Figure 5.4 generated by using color map *CS2* with constant saturation. 71
Figure 5.21 Color-coded version of Figure 5.4 obtained after segmentation, using a constant saturation and 5 different hues (complementary colors), (a) and (b) blue, green, red, cyan and yellow, (c) blue, yellow, cyan, red and green. 72
Figure 5.22 Colored version of Figure 5.4 generated by using color map *VS1* with variable saturation. 73
Figure 5.23 Colored version of Figure 5.4 generated by using color map *VS2* with variable saturation. 73
Figure 5.24 Montage of original and all color coded images for comparative rating. 75
Figure 5.25 Percent of screeners able to correctly identify threat objects on each type of images. 75
Figure 5.26 Mean ratings of eight pseudo-coloring approaches and gray level original obtained from screeners' evaluation. 76
Figure 6.1 Categorization of the pixels in a given luggage scene as local background pixels or detail pixels. 79
Figure 6.2 Flow chart of the developed approach for dual-energy x-ray image fusion. 80
Figure 6.3 Dual-energy x-ray images and fused results generated using the local spatial information based fusion algorithm, (a) low-energy image, (b) high-energy image, (c) combined grayscale image, and (d) noise-reduced combined version. 81
Figure 6.4 Noise analysis. (a) A selected small patch of size 160×60, (b) and (c) histograms of the small patches taken from the low-energy and the high-energy images. 82
Figure 6.5 Noise reduction. (a) Histogram of the noise-reduced version of the same small patch as used in Figures 6.4 (b), (b) histogram of the noise-reduced version of the same small patch as used in Figures 6.4 (c). 82
Figure 6.6 Noise reduction. (a) Histogram of the small patch taken from the combined version, (b) histogram of the small patch taken from the noise-reduced combined version. 83
Figure 6.7 General procedure of image fusion with the wavelet transform. 84
Figure 6.8 Two commonly used fusion rules: pixel based fusion rule (green) and region based fusion rule (red). 84
Figure 6.9 Results of wavelet-based fusion algorithm, (a) and (b) low-energy and high-energy x-ray images, and (c) and (d) fused image generated using wavelet-based fusion algorithm, before and after the application of noise reduction. 87
Figure 6.10 Noise analysis. (a) and (b) Wavelet transforms of Figure 6.9 (a) and (b). 88
Figure 6.11 Dual-energy x-ray images and fused results generated using the algorithms presented in Section 6.1 (a) low-energy image, (b) high-energy image, (c) combined grayscale image, and (d) noise-reduced combined version. 90
Figure 6.12 Dual-energy x-ray images and fused results generated using the algorithms presented in Section 6.1 (a) low-energy image, (b) high-energy image, (c) combined grayscale image, and (d) noise-reduced combined version. 91
Figure 6.13 Dual-energy x-ray images and fused results generated using the algorithms presented in Section 6.1 (a) low-energy image, (b) high-energy image, (c) combined grayscale image, and (d) noise-reduced combined version. 92
Figure 6.14 Results of wavelet-based fusion algorithm, (a) low-energy x-ray image (b) high-energy x-ray image, (c) fused image generated by using wavelet-based fusion algorithm. 93

Figure 6.15 Results of wavelet-based fusion algorithm, (a) low-energy x-ray image (b) high-energy x-ray image, (c) fused image generated by using wavelet-based fusion algorithm, and (d) fused image version generated by incorporating noise-reduction step into the wavelet-based fusion algorithm. 94
Figure 6.16 Color versions (a) manufacturer's color image, (b) & (c) color versions obtained by applying "Warm" scale to Figure 6.17 (c) and (d), respectively, (d) color version obtained by applying Set 1 to Figure 6.17 (c). 96
Figure 6.17 Color versions (a) manufacturer's color image, (b) & (c) color versions obtained by applying "Warm" scale to Figure 6.3 (c) and (d), respectively, (d) color version obtained by applying Set 1 to Figure 6.3 (c). 97
Figure 6.18 Histograms of difference images 98
Figure 6.19 Color versions, (a) and (b) color images produced using color Scheme 3, (c) and (d) manufacturer's color images. 99
Figure 6.20 IQM vs. Visual National Imagery Interpretability Rating Scale (NIIRS) 100
Figure 6.21 Evaluation results by applying the IQM of Nill et al. to the luggage scene in Figure 6.3 101
Figure 6.22 Evaluation results by applying the IQM of Nill et al. to the luggage scene in Figure 6.13 102
Figure 7.1 (a) The GUI of XIP, (b) XIP drop-down menus showing image enhancement and visualization algorithms implemented. 105
Figure 7.2 Schematic diagram of the Remote Supervision System (RSS). 107
Figure 7.3 A typical interaction between a client and a server using connection-oriented sockets. 109
Figure 7.4 Flow of loading an image from the server. 110
Figure 7.5 Flow of sending a processed image version back to the server. 110
Figure 7.6 GUI of the client-end application. 111
Figure 8.1 Main procedure used to process single-energy and dual-energy x-ray images. 113

1 Introduction

Achieving higher detection rates of threat objects during airport luggage inspection is a pressing and sought-after goal for airport and airplane security personnel.

1.1 Background

Airport luggage inspection has always been a challenge because of (1) the complexity naturally present in knowing the content of each individual bag, (2) the constant increase in the level of sophistication and methods of device concealment by terrorists, and (3) the decrease in screeners' alertness when constantly gazing at a screen and seeing almost the same type of objects over and over again.

Traditionally, potential threats are thought of as metallic guns and knives; that is, objects made from high-density materials. After September 11, 2001, the Transportation Security Administration (TSA) made public a lot of newly prohibited threat items—among others, plastic, glass, and wooden sharp objects that can be used as knives. These objects are made of low-density materials. This increase in the types of potential threat objects significantly compounded luggage inspection problems.

A number of techniques based on x-rays, gamma rays, electromagnetic field, and millimeter waves have been employed for detecting weapons and explosives [Singh and Singh, 2003]. X-ray based techniques are the most common means used in airports for luggage inspection for the following reasons: (1) x-ray technology can help provide information on the objects' density and their effective atomic number (The "effective atomic number" is the estimate of a hypothetical single element that will give the same x-ray attenuation as the substance being evaluated); (2) x-ray technology has been developed for over a century; (3) x-ray technology is safer to human beings and luggage contents than other radiations such as nuclear magnetic resonance; (4) x-ray physics is well understood; and (5) x-rays are less expensive and easy to operate [Singh and Singh, 2003].

Different x-ray techniques are used in airports for the inspection of luggage. Among the most popular methods are conventional transmission imaging, dual energy x-ray imaging, scatter imaging and 3D imaging [Singh and Singh, 2003]. In this thesis, the focus will be on conventional single energy and dual energy x-ray luggage detection systems. Conventional x-ray systems are effective in detecting objects of metallic composition (knives and guns), while low-density weapons could easily go unchecked. Objects such as metallic guns and knives, which are characterized by high-density responses in x-ray images, are also easily spotted by screeners. However, objects like plastic, glass, and

wooden sharp items are characterized by very faint, low-density responses in x-ray projections and are very hard to distinguish by screeners. Commercial dual energy x-ray systems are used to identify materials in luggage by comparing two images of the luggage obtained at two different x-ray energy levels and estimating the atomic number of the materials. However, the real density of objects is poorly known and only an estimate of atomic number can be generated, i.e. effective atomic number. As a result of these limitations, the false alarm rate of dual energy x-ray luggage detection systems reaches to roughly 30% [Singh and Singh, 2003].

1.2 Motivation

Our motivation for this research develops as a result of realizing the potential of image processing and visualization algorithms to clearly increase the rates of detecting concealed and low-density threat items in luggage inspection as compared to raw images.

During the research and design of these algorithms, considerations were given to the following aspects:

1. Increase operators' alertness, without decreasing inspection speed or customer satisfaction.
2. Minimize the role of human operators in monitoring and detection by automating or semi-automating the process of inspection at carry-on luggage stations.

This research, as introduced in Section 1.1, focuses on processing x-ray luggage scans generated by using conventional transmission imaging, referred to as single-energy x-ray images, and x-ray luggage scans generated by using dual energy x-ray imaging, referred to as dual-energy x-ray images. Gray-level image enhancement, image segmentation, pseudo coloring and image fusion, shown in Figure 1.1, are the major techniques investigated to improve single-energy and dual-energy x-ray images.

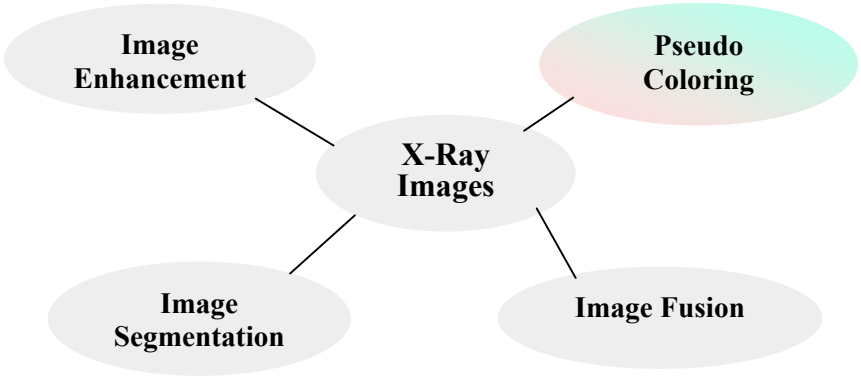

Figure 1.1 Image processing techniques involved in the improvement of raw x-ray luggage scans.

1.3 Contributions

The primary contribution of our research, as shown in Figure 1.2, includes (1) optimized combinations of common segmentation and enhancement methods, (2) novel HSI based color coding methods, and (3) dual-energy image fusion algorithms—spatial information-based and wavelet-based image fusion.

Best combinations of common segmentation and enhancement methods: Several combinations of selected common image segmentation and enhancement methods were designed and applied to single-energy x-ray images. Two combinations, *logarithm transform + contrast stretching* and *image negative + hdome + contrast stretching*, are particularly effective in enhancing single-energy x-ray luggage images.

HSI based color-coding methods: A color scale called "Springtime" is designed to reveal both value and shape information by decreasing the perceptual artifacts of the human visual system in general and simultaneous contrast in particular. Additionally, constant saturation and variable saturation schemes based on the HSI color space are proposed in order to apply color to preprocessed gray scale data.

Dual-energy image fusion algorithms:
Local spatial information-based image fusion: classify each pixel in a luggage scene into either background pixel or detail pixel, and then highlight detail pixels with the assumption that detail pixels carry the features of interest in the luggage scene.

Wavelet based image fusion: One of the most important features of dual-energy x-ray images is used as a basis of the wavelet based image fusion − distinct objects in a given luggage scene show similar general contours in both the high-energy image and the low-energy image. This algorithm have details, uniquely exhibited in the low-energy or high-energy x-ray image, be incorporated into the fused version, and details existing in both low-energy and high-energy x-ray images be more visible in the fused version.

For each of the preceding algorithms, qualitative and quantitative results demonstrate their effectiveness in improving x-ray luggage images.

1.4 Outline of this Thesis

The remainder of this thesis is organized as follows. Chapter 2 presents the state of the arts in x-ray carry-on luggage inspection systems, gray scale image enhancement, image segmentation, pseudo coloring and image fusion. Gray scale enhancement techniques applied to x-ray luggage scenes and experimental results are introduced in Chapter 3. Chapter 4 deals with image hashing algorithms and entropy-based image decluttering methods, their variations, and applications to single-energy x-ray luggage images. Chapter 5 describes a series of linear and non-linear pseudo-coloring maps designed and

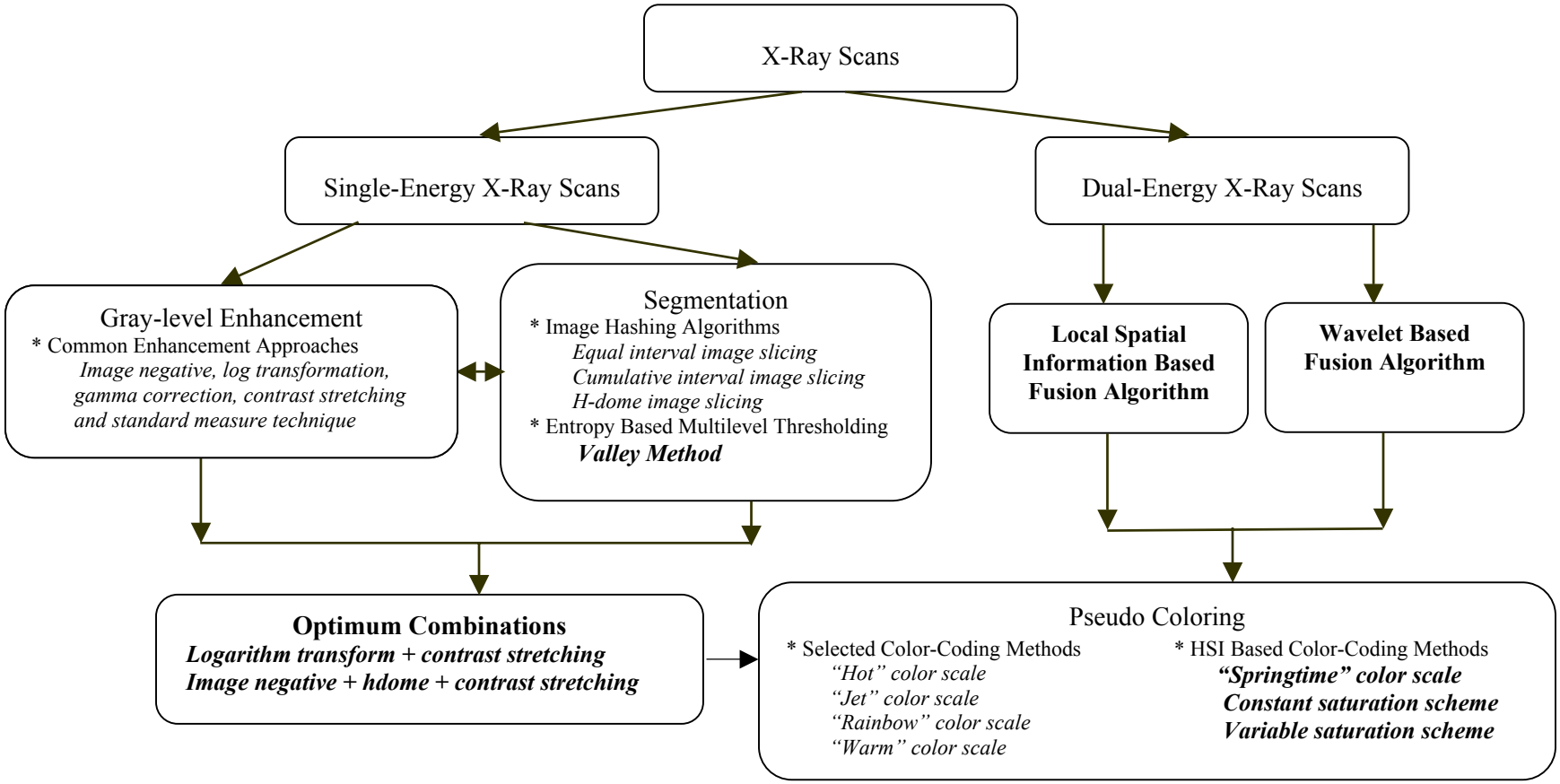

Figure 1.2 Algorithms selected and proposed (in bold) for the improvement of raw x-ray luggage scans.

applied to single-energy x-ray luggage scans. Two image fusion algorithms, local spatial information-based and wavelet-based fusion methods are proposed to integrate dual-energy x-ray images, and their experimental results are presented in Chapter 6. Chapter 6 also discusses objective image quality measures used for the evaluation of fused x-ray images and shows their evaluation results. Two application software, (1) x-ray image processing (XIP) developed to integrate and apply various image processing and visualization algorithms to x-ray luggage images, and (2) wireless tablet PC-based remote supervision system (RSS) designed and developed to provide a mobile station in airport setting, are introduced in Chapter 7. This thesis is concluded with the merits of image processing and visualization algorithms, which are demonstrated by experimental results, on-site subjective and objective evaluations, major contributions and potential research extensions in Chapter 8.

2 Literature Review

This chapter presents a review of the research literature and background on x-ray imaging. It begins with the principles of x-ray imaging for airport luggage inspection and the characteristics of single-energy and dual-energy x-ray images. The review then focuses on image processing and visualization techniques involved in our study. Sections 2.3 through 2.6 present the state of arts in gray-level enhancement, image segmentation, pseudo coloring, image fusion, and image quality measure. This chapter is concluded with a summary that highlights key theories and methods, serving as the basis of our research, and our research direction.

2.1 Physics of X-Ray Imaging

As shown in Figure 2.1, x-rays are electromagnetic radiations ranging in wavelength from 10^{-8} m to 10^{-12} m. The energy, E of an x-ray is computed as:

$$E = h\frac{c}{\lambda} \quad , \tag{2.1}$$

where c is the speed of light (2.998×10^{8}m/s), h Plank's constant, and λ the wavelength of the x-ray radiation. The penetrability of x-ray is generally proportional to the power of its energy.

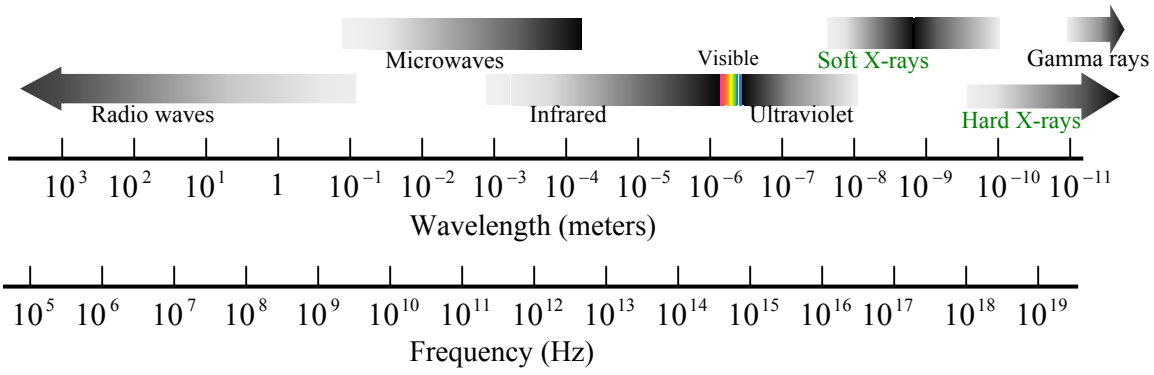

Figure 2.1 The electromagnetic spectrum.

X-rays can be seen as beams of x-ray photons. An x-ray photon moves in a straight line until it undergoes a collision with a nucleus. As the result of a collision, the x-ray photon may disappear (absorption) or change its velocity (scattering). Conventional x-ray luggage detection systems measure x-ray absorption. The absorption of x-ray radiation by a material is proportional to the degree of x-ray attenuation and is dependent on the energy of the x-ray radiation and the thickness, density and atomic number of the material. The intensity of the x-ray radiation after passing through a material can be described by (2.2).

$$I = I_0 e^{-\mu x}, \tag{2.2}$$

where I is the intensity of the x-ray radiation after passing through a material; I_0 the intensity of the narrow beam mono-energetic x-ray radiation before passing through a material; x object thickness; and μ object attenuation coefficient whose value depends strongly on the x-ray energy E, the atomic number Z, the density ρ, and atomic mass A as given by (2.3).

$$\mu \approx \frac{\rho Z^4}{AE^3}, \tag{2.3}$$

2.2 X-Ray Carry-On Luggage Inspection Systems

As mentioned in Section 1.2, this research concentrates on processing and visualizing x-ray image scans generated by using conventional transmission x-ray imaging and dual energy x-ray imaging. In this section the two kinds of x-ray carry-on luggage inspection systems, conventional transmission x-ray imaging systems and dual energy x-ray imaging systems, commonly used in airports are introduced.

2.2.1 Conventional Transmission X-Ray Imaging Systems

A conventional transmission x-ray imaging system has a fan shaped or scanning x-ray beam that is transmitted through the luggage to be inspected. The absorption of the x-ray is measured by a line of detectors and a high-resolution image, derived from the degree of absorption of the x-ray, is generated. Figure 2.2 depicts a commercial conventional transmission x-ray carry-on luggage detection system from Siements-Heimann. Two example single-energy x-ray images generated by this type of detection systems are shown in Figure 2.3. Higher pixel intensities in the images in Figure 2.3 correspond to high-density material, whereas lower pixel intensities correspond to low-density material in luggage.

As shown in the two examples of single-energy x-ray images, especially in Figure 2.3 (b), different objects in a luggage scene are hard to distinguish by just observing the raw images directly acquired from luggage detection systems. In addition, conventional

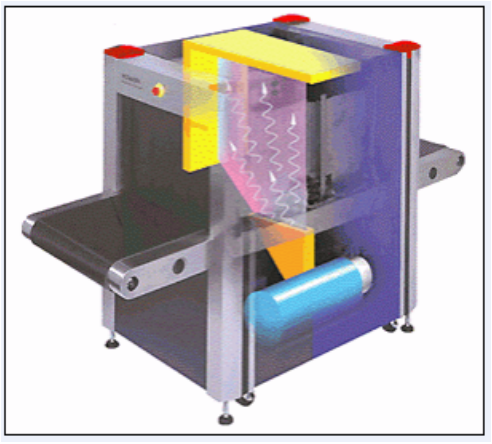

Figure 2.2 Siements-Heimann transmission x-ray imaging system [Heimann, 2004].

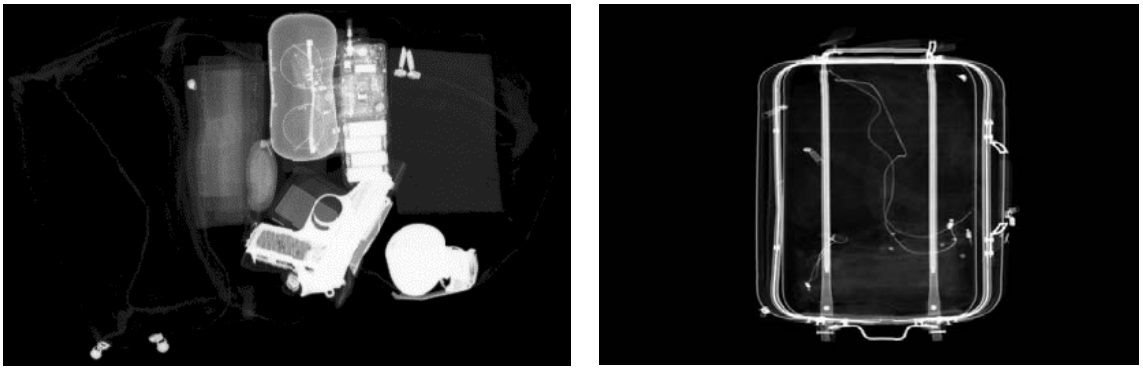

(a) (b)

Figure 2.3 Example single-energy x-ray images containing, (a) high-density potential threats, and (b) low-density potential threats.

transmission x-ray imaging systems cannot differentiate between a thin sheet of strong absorber and a thick slab of a weak absorber [Singh and Singh, 2003].

2.2.2 Dual Energy X-Ray Imaging Systems

A dual energy x-ray imaging system uses two x-ray energy levels, one high and one low energy, for the detection of weapons. At higher energy levels, over 100 kV, the absorbed energy depends primarily on the density of the material. The higher the density, the more the energy absorbed by the object and therefore the darker the image. At lower energy levels, around 80 kV, the absorption depends primarily on the effective atomic number as well as the thickness of the material. While areas of heavy metal are dark in both low-energy and high-energy images, areas of light elements are darker in the low-energy image. Light-elements such as carbon, nitrogen and oxygen can be detected by comparing both images [Singh and Singh, 2003]. Two pairs of example dual-energy x-ray images are shown in Figure 2.4.

Certain commercial dual energy x-ray luggage detection systems feature dual-energy analysis to estimate the atomic number of materials in luggage. The problem of differentiating between a thin sheet of strong absorber and a thick slab of a weak absorber, that faces conventional transmission x-ray imaging systems, is solved in dual energy x-ray luggage detection systems. However, dual energy x-ray luggage detection systems have a main limitation that the real density of objects is poorly known for real luggage items and the system only generates an estimate of atomic number, i.e. effective atomic number [Singh and Singh, 2003]. As a result of the limitation, the false alarm rate of dual energy x-ray luggage detection systems reaches to roughly 30%.

The remaining sections of this chapter, Sections 2.3 through 2.6, introduce the image processing and visualization techniques reviewed in out research to improve single-energy and dual-energy x-ray images using image processing and visualization techniques and thus increase the rates of detecting concealed and low-density threat items in luggage inspection.

2.3 Image Enhancement and Segmentation

2.3.1 Image Enhancement

Image enhancement approaches can be grouped into three categories, point enhancement, spatial domain enhancement and frequency domain enhancement.

2.3.1.1 Point Enhancement

Most widely used techniques in point enhancement include contrast stretching and histogram modeling. A principal advantage of this kind of enhancement methods is that they are automatic methods. However, since in general they use global information of images to do enhancement, they are not able to differentiate between several areas of an image that might require different levels of contrast enhancement or special treatments [Munteanu and Rosa, 2004].

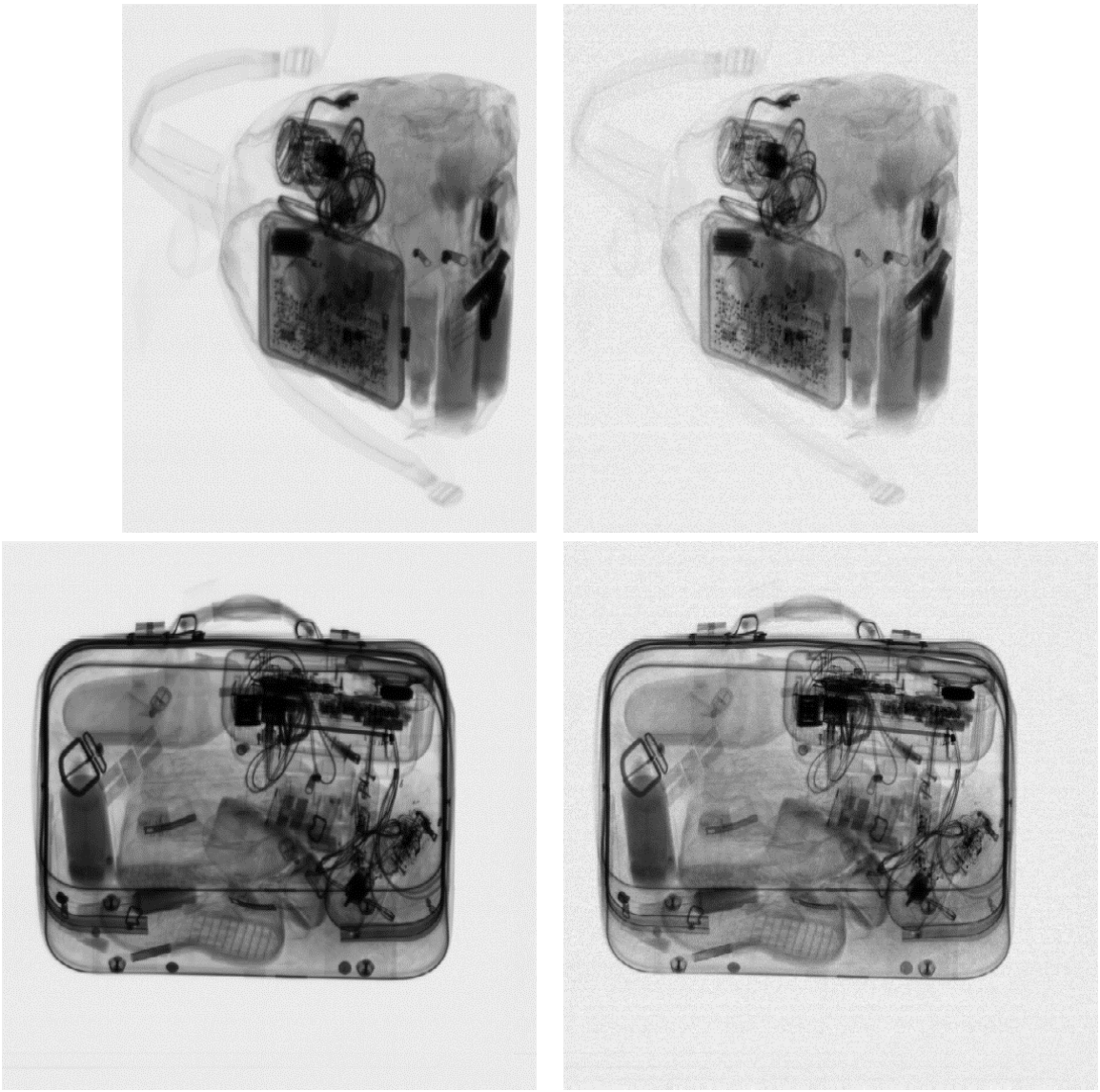

Figure 2.4 Two pairs of example dual-energy x-ray images, low-energy x-ray images (left) and high-energy x-ray images (right).

2.3.1.2 Spatial Domain Enhancement

Spatial domain enhancement techniques modify pixel values based on the values of their surrounding pixels. Several representative spatial enhancement methods proposed in the recent decade are presented as follows.

1) Adaptive Enhancement Method Based on Human Visual Properties

[Hadhoud, 2001] proposed an adaptive image enhancement system that implements the human visual properties for the contrast enhancement of x-ray images. The human visual properties that are considered to benefit contrast enhancement are the adaptive nature, multi-channel and highly non-linearity. Therefore, this enhancement method exhibits adaptive, multi-channel and non-linear properties.

The simple imaging model stated below is the basis of Hadhoud's enhancement method. This model assumes that the radiation from a scene is the product of a low spatial frequency illumination component and a high spatial frequency reflectance component from the objects in the scene. The mathematical form of the simple model is given in (2.4), in which *i(m,n)* represents the illumination and *r(m,n)* the reflectance. For x-ray imaging, *i(m,n)* can be considered as the incident x-ray energy and *r(m,n)* is the change in object absorption of the penetrating x-ray energy.

$$f(m,n) = r(m,n) \times i(m,n)\,, \tag{2.4}$$

Performing the logarithm of (2.4) yields

$$\log(\, f(m,n)) = \log(\, r(m,n)) + \log(\, i(m,n))\,, \tag{2.5}$$

Thus, as shown in (2.6), low pass filtering of (LPF) *f(m,n)* will result in *log(i(m,n))* which corresponds to the low varying part of an image while high pass filtering (HPF) of *f(m,n)* will result in *log(r(m,n))* which corresponds to the high varying part of the image.

$$\hat{g}(f(m,n)) = \alpha(H_{lp}\{\hat{g}(f(m,n)\}) + \beta(H_{hp}\{\hat{g}(f(m,n)\})\,, \tag{2.6}$$

Where $\alpha < 1$ and $\beta > 1$ are used to enhance contrast. Figure 2.5 shows the block diagram of a spatial enhancement method called single HP channel and fixed image enhancement that are developed based on the imaging model above.

Considering the adaptive and multiple channel properties of the human visual system, [Hadhoud, 2001] proposes using adaptive HPF and LPF instead of fixed ones and using multiple HP channels other than single HP channels for contrast enhancement of x-ray images. Figure 2.6 shows the block diagram of the proposed algorithm.

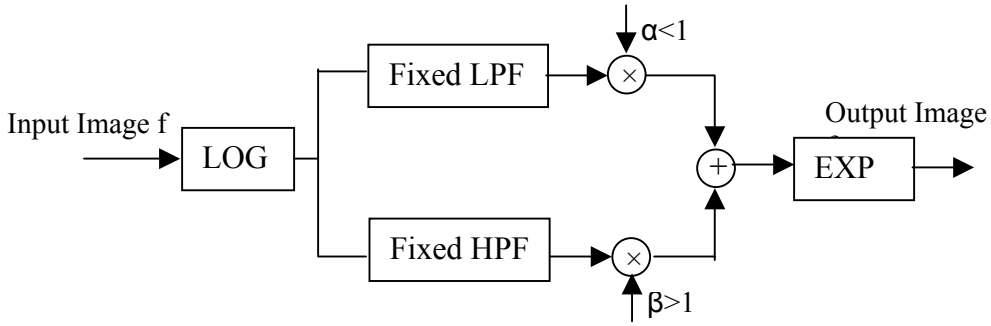

Figure 2.5 Block diagram of single HP channel and fixed image enhancement [Hadhoud, 2001].

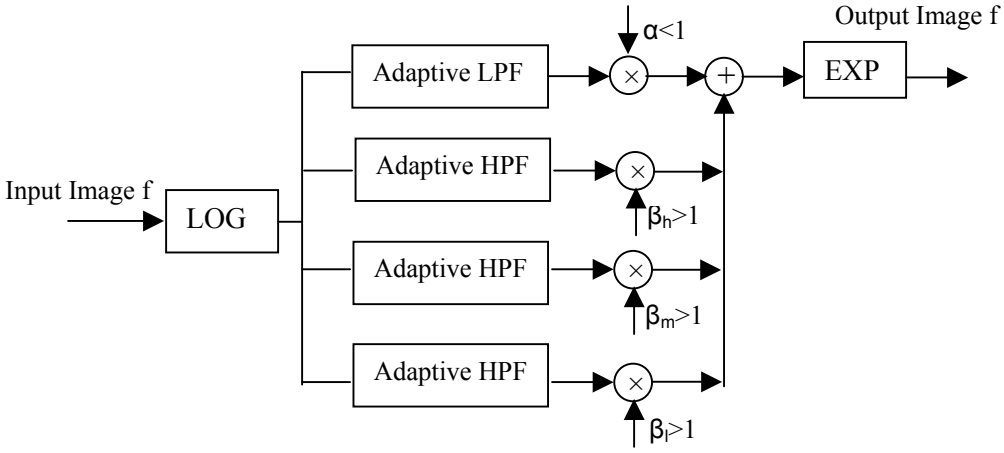

Figure 2.6 Block diagram of multiple HP channels and adaptive image enhancement [Hadhoud, 2001].

Mathematically (2.7) expresses the use of multiple HP channels and adaptive image enhancement.

$$\hat{g}(f(m,n)) = (\alpha_{hpl} + \alpha_{hpm} + \alpha_{hph})(H_{lp}\{\hat{g}(f(m,n)\}) + \beta_{hpl}(H_{hpl}\{\hat{g}(f(m,n)\}) + \beta_{hpm}(H_{hpm}\{\hat{g}(f(m,n)\}) + \beta_{hph}(H_{hph}\{\hat{g}(f(m,n)\} \quad (2.7)$$

where α 's and β 's are adaptively adjusted according to the image local contrast information. Results in [Hadhoud, 2001] show that this adaptive spatial enhancement method outperforms its fixed counterpart.

2) Enhancement Method Driven by Evolutionary Algorithm (EVOLEHA)

Evolutionary algorithms (EAs) are search and optimization methods that use a fixed size population of individuals representing potential solutions to an optimization problem.

In [Munteanu and Rosa, 2004], authors use a local enhancement technique based on a variation of a statistical scaling method [Jain, 1991, Pratt 2000]. The enhancement kernel applied to each pixel at location *(x, y)* is given by (2.8).

$$g(x,y) = T(f(x,y)) \equiv \left(k\frac{M}{\sigma(x,y)+b}\right).\left[f(x,y) - c.m(x,y)\right] + m(x,y)^a, \quad (2.8)$$

where *f(x,y)* is an input image; *g(x,y)* is an output image; *m(x,y)* and $\sigma(x,y)$ are the graylevel mean and standard deviation computed for pixels inside a neighborhood centered at *(x,y)* and having $n \times n$ pixels; *a, b, c* and *k* are parameters of the enhancement kernel whose values are the same for all pixels and are taken as positive real values. The task of the EA in EVOLEHA is to find the best combination of the four parameters according to an objective criterion describing the quality of the enhancement.

The enhancement evaluation objective criterion proposed by [Munteanu and Rosa, 2004] is the one that maximizes $H(I), \eta(I), E(I)$ given in (2.9).

$$Eval(I) \sim \quad H(I), \eta(I), E(I), \quad (2.9)$$

where I is a enhanced image being evaluated; *H(I)* is a entropic measure proportional to the number of gray levels present in the image; $\eta(I)$ represents the number of edge pixels in the image; and *E(I)* denotes the intensity values of the edges. Thus, the best-enhanced resulting image has the maximum number of edges, higher intensities of the edges and a histogram with an approximately uniform distribution.

Using EA, the enhancement process is automated and achieves a combined goal of robustness and wide applicability. But the drawback of EVOLEHA is its heavy load of computation, which makes the method unsuitable for real-time applications. This results from the fact that the method requires a series of trial enhancements until producing the final good solution. Therefore, how to decrease the computational complexity or reduce the population size of individuals and the maximum number of generations is a topic of continued research in this kind of enhancement methods.

3) Fuzzy Theory Based Algorithms

Fuzzy logic theory is applied for image enhancement mainly for the following two reasons [Hassanien and Bader, 2003]:

- Fuzzy techniques are powerful tools for knowledge representation and processing
- Fuzzy techniques can manage the vagueness and ambiguity efficiently.

Fuzzy image enhancement is based on mapping intensity values into a fuzzy plane, using a membership transformation function. The goal is to generate an image of higher contrast than the original image by giving a larger weight to the intensity values that are closer to the mean value of the image.

Five classes of fuzzy theory based algorithms are introduced in [Hassanien and Bader, 2003]. They are possibility distribution algorithm, contrast improvement with intensification operator, contrast improvement with fuzzy histogram hyperbolization, contrast improvement based on fuzzy if-then rules, and locally adaptive contrast enhancement. Five specific methods separately corresponding to the above five classes of fuzzy theory based algorithms are implemented and applied to mammogram images to increase their contrast in [Hassanien and Bader, 2003]. The effect of the decrease in grayness ambiguity for the five specific methods is shown in Table 2.1.

Table 2.1 Effects of the Decrease of Grayness Ambiguity of five fuzzy theory based algorithms.

Algorithm	Conclusion
Algorithm 1	Decreases both the index of fuzziness and the entropy, and the resulting image is appropriate for visual perception and future tacking.
Algorithm 2	Increased both grayness ambiguity, and therefore the resulting image is not appropriate for visual perception.
Algorithm 3	Compared to other algorithms, it gives the lowest grayness ambiguity, and its results are appropriate for visual perception.
Algorithm 4	Gives lower grayness ambiguity than the first algorithm, although the later are more appropriate for visual perception.
Algorithm 5	Does not decrease the grayness ambiguity much, and the resulting image is not appropriate for visual perception nor future tracking.

4) Wavelet-based Enhancement Algorithms

In general, wavelet-based enhancement techniques use a reversible wavelet decomposition, which may be redundant or not and then perform enhancement by selective modification (amplification) of certain wavelet coefficients prior to reconstruction [Unser and Aldrouri, 1996]. That is, accentuate useful weak image features. Wavelet-based enhancement techniques have been extensively used in medical applications, especially in mammography. In mammography many researchers report that the improvement in performance obtained by wavelet-based enhancement techniques is superior to that of the standard enhancement techniques.

Many enhancement techniques suffer from the tendency to increase the visibility of noise at the same time as they enhance the visibility of the underlying signal. Therefore some researchers are focused on noise reduction. [Brown] proposed an adaptive strategy for wavelet-based image enhancement. The method processes wavelet coefficients individually and treats the correlation between wavelet planes as providing an indication of the likelihood that noise is present. The indication is then used to control the application of gain so as to suppress noise and enhance other wavelet coefficients.

2.3.1.3 Frequency Domain Enhancement

The frequency domain image enhancement is based on Fourier theory. Image information can be divided into high frequency information and low frequency information. Low-frequency information in an image represents background and high-frequency information in the image represents detail. Image enhancement methods in the frequency domain are based on changing the ratio of the high frequency and the low frequency components.

Images processed using frequency domain techniques are first transformed to the frequency domain by performing a Fourier transform. Different weights can then be chosen for the high frequency and low frequency parts to smooth or sharpen background(s) or/and detail(s). After performing the processing in the frequency domain, the images must be transformed back into the spatial domain by applying the inverse Fourier transform for display. Analogous to spatial domain approaches, frequency domain techniques can process frequency information of images globally or locally, thus various global frequency filters and adaptive frequency filters are proposed for image enhancement.

2.3.2 Image Segmentation

Image segmentation is performed in many applications of image processing to either separate an image into its constituent regions/objects or to extract objects/features of interest. The application of image segmentation in our research aims at easing the screeners' task by reducing the interference of harmless items and making potential threats more visible.

Image thresholding enjoys a central position in image segmentation due to its simplicity and effectiveness. Based on the information exploited, image thresholding techniques can be categorized into six groups, histogram based methods, clustering-based methods, entropy-based methods, object attribute-based methods, spatial methods, and local methods [Sankur and Sezgin, 2001].

Thresholding based on information theory has received considerable interest in recent years as many well-known entropy-based thresholding methods have been proposed over the past two decades. In our study, we emphasize entropy-based thresholding. Two key concepts of information theory, Shannon's entropy and Kullback-Leibler information distance are widely used in defining image entropies. Based on the two concepts, image entropies are computed using either the histogram of an image or the co-occurrence matrix of an image. Several important image entropies, global entropy [Pun, 1980; Kapur and Wong, 1985], local entropy [Pal and Pal, 1989], joint entropy [Pal and Pal, 1989], and relative entropy [Chang, 1994] are consecutively proposed. Desired threshold(s) can be obtained when the image entropy of a thresholded image is maximized, such as global entropy, local entropy and joint entropy, or when the image entropy between the original image and its thresholded version is minimized, such as relative entropy, in entropy-based threshoding techniques. Nowadays, many researchers [Chang et al, 2002; Luo and Tian, 2000] put their efforts on exploring fast entropy-based multilevel thresholding since most existing entropy-based thresholding methods were proposed in the bi-level case. Although these methods can directly be extended to the multilevel case, the computational load becomes a major limitation to their application in practical situations.

Taking into account the speed requirements in carry-on luggage inspection at airports, different thresholding algorithms, particularly timesaving entropy-based multilevel thresholding algorithms, are selected, improved and applied to x-ray luggage scans. We will elaborate more on their main technical aspects in Chapter 4.

2.4 Pseudo Coloring

Pseudo coloring of gray scale images is a typical process used as a means of supplementing the information in various fields such as medicine, inspection, military, and several other data visualization applications. This process can significantly improve the detectability of weak features, structures, and patterns in an image by providing image details that otherwise would not be noticed [Czerwinski et al., 1999].

The main purpose of color-coding is to harness the perceptual capabilities of the human visual system, that of airport screeners in this case, to extract more information from the image. This will provide a better qualitative overview of complex data sets and will assist in identifying regions of interest for more focused quantitative analysis by making similarly joined areas in the scene more distinguishable [Dai and Zhou, 1996]. By helping in differentiating objects of various densities, color-coding also minimizes the

role of human operators in monitoring and detection, reduces the time required to perform inspection, and lessens the probability of error due to fatigue.
Most visualization techniques generally contain a step in which data values are mapped to color to make the overall range of data visible. Given the fact that the human eye is more sensitive to some parts of the visible spectrum of light than to others and that the brain may interpret color patterns differently, the interpretation of results produced by these visualization techniques depends crucially on the color mapping (color scale) applied.

Traditionally, color scales were designed by having the hue sequence range from violet, via indigo, blue, green, yellow and orange, to red, following the color order of the visible spectrum. Since the human visual system has different sensitivities to different wavelengths, researchers such as Clarke and Leonard [Clarke and Leonard, 1989] indicated that spectrum-based color scales were not perceived to possess a color order that corresponds to the natural order of the gray scale in the image.

Many research efforts in pseudo coloring have been made over the past several decades. Based on the primary aspects researchers have focused on for the design of color scales, the various available pseudo-coloring techniques can be grouped as follows: (a) A number of researchers attempted to develop natural-order color scale preserving the order of gray levels by defining a particular path traversing the RGB color space under certain predefined constrains. The heated-object scale is achieved by bringing the RGB intensities up in the order of red, green and blue and limiting the path to 60^0 clockwise from the red axis. This selection is based on the claim that natural color scales seem to be produced when the intensities of the three primary colors rise monotonically with the same order of magnitude of intensities throughout the entire scale [Pizer et al., 1982]. To construct a natural color scale, Lehmann et al. [Lehmann et al., 1997] defined a spiral-like color scale in the RGB model keeping the original brightness progression of gray scale images. Specifically speaking, their color scale follows a spiral-like path along the diagonal of the RGB model. Lehmann et al. formularized such scale to allow the determination of the resulting number of colors. They demonstrated such scale's effectiveness by applying it to medical x-ray images, and they also pointed out that better results could be obtained if other color models were used such as HSI as the lightness is directly represented by one of the axes in HSI. (b) Several studies [Levkowitz and Herman, 1992; Rudaz et al., 1997; Shi et al., 2002] focused on constructing a uniform color scale where adjacent colors are equally spaced in terms of Just Noticeable Differences (JNDs) and maintain a natural order along this color scale. Levkowitz and Herman's research [Levkowitz and Herman, 1992] provided a scale with the maximum uniform resolution. They were hoping that their optimal color scale outperformed the gray scale, but evaluation results did not confirm that, at least for their particular application. They presented several reasons that might have caused the unexpected results. One particular reason was that they used the CIELUV model to adjust the final colors, which might not have been appropriate to model the perceived uniformity; another reason was that the perceived change in color due to its surroundings was not considered. Shi et

al. [Shi et al., 2002] designed a uniform color scale by visually setting up its color series to run from inherently dark colors to inherently light colors, i.e. from black through blue, magenta, red, yellow to white, then further adjusting the colors to make them equally spaced. Their color scale was evaluated by comparing it to the gray scale. The authors indicated that the contrast sensitivity has been improved after applying their uniform scale, but they failed to demonstrate any significant outcome. (c) Some researchers focused on decreasing the perceptual artifacts of the human visual system such as the simultaneous contrast, to convey value and shape information accurately and effectively. Ware [Ware, 1988] divided the information available in images into metric or value information and form information. He proposed theoretical principles to predict which color scale would be effective in conveying both metric and form information. Through a series of psychophysical experiments, Ware demonstrated that simultaneous contrast was a major source of error when reading metric information, but only partially verified his form hypothesis. (d) Other researchers utilized common mathematical functions such as the sine function to construct desired mappings or color scales. Gonzalez and Wood [Gonzalez and Woods, 2002] described an approach where three independent mathematical transforms were performed on the gray level data, and the three output images fed into the R, G and B channels to produce a specific color mapping. The nature of these mathematical functions would determine the characteristics of the color scale.

Through interactions with various types of color scales under different circumstances, most researchers agree that color is useful to reveal more information in images, and for certain applications some types of color scales are superior to others. In that regard, Levkowitz and Herman [Levkowitz and Herman, 1992] concluded that several easily interchangeable color scales could substantially increase the perception of information in images over the use of a single scale.

The only widely known coloring scheme [Heimann, 2004], in use since the introduction of color in x-ray luggage inspection, requires two x-ray images, one at low energy and the second at high energy, resulting in the need for a more costly system. The atomic number of the material is determined using the two images and color is assigned based on atomic number values. There was no perceptual or cognitive basis - psychological or physiological - on which color combinations were selected. In an effort to address the relatively new problem of visualizing low density threat items in luggage scenes, while incorporating considerations of the perceptual and cognitive characteristics of the human operator, a set of RGB and HSI-based color transforms, which will be presented in Chapter 5, were designed and applied to single energy x-ray luggage scans.

2.5 Image Fusion

Image fusion is defined as a process of combining information or features of interest from multiple source images to generate a single grayscale or color image that can convey more useful information than any of the individual source image used alone.

Many common and advanced image fusion approaches share the same fundamental mathematical tools. Based on the mathematical tools used in these image fusion methods, they can be classified into three groups: (1) Statistical and numerical methods, (2) Multi-resolution based methods, and (3) Color fusion methods. Grayscale image fusion (Groups 1 and 2) is commonly performed at the pixel and feature levels. At the pixel level, the images are combined by considering individual pixel values or a small set of pixel values of the source images. At the feature level, an image is initially segmented in some way to produce a set of regions. Various properties of these regions can be calculated and used to determine which features from which images are included in the fused image [Lewis et al, 2004].

Here we briefly introduce a number of representative approaches of the statistical and numerical fusion methods and the multi-resolution based fusion methods, which were the two approaches used in this research.

2.5.1 Statistical and Numerical Fusion Methods

A simple approach to image fusion is to compute the weighted average of corresponding pixels of the source images. The principal component analysis (PCA) proposed in [Rockinger and Fechner, 1998] is a typical pixel-level weighted fusion method. The weights for each source image in the PCA method are computed from the eigenvector corresponding to the largest eigenvalue of the covariance matrix of the source images [Xue et al, 2002]. Variations of the PCA method and other arithmetic signal combinations are numerous [Piella, 2003]. In some research, a fusion task was expressed as an optimization problem. In Bayesian optimization, the goal is to find the fused image which maximizes a posterior probability. In the Markov random field approach, the input images are modeled as Markov random fields to define a cost function which describes the fusion goal. A global optimization strategy such as simulated annealing is employed to minimize this cost function [Piella, 2003].

2.5.2 Multi-Resolution Fusion Methods

Multiresolution decomposition-based fusion methods are motivated by the fact that the human visual system is primarily sensitive to local contrast changes. i.e. edges. Multiresolution decompositions provide a convenient spatial-scale localization of these local changes [Piella, 2003]. Three major steps are involved in multi-resolution fusion methods: (1) Decompose the source images into a multi-resolution representation using a selected transform, (2) Construct the multi-resolution representation of the fused image using a particular fusion rule and the multi-resolution representations of the source images, and (3) Compute the inverse multi-resolution transform to the multi-resolution representation of the fused image to obtain the fused result. The difference between various multi-resolution fusion methods is in the multi-resolution transform and fusion rules employed. The pyramid transform, discrete wavelet transform and discrete wavelet frame are the most commonly used multi-resolution decomposition methods for multi-resolution image fusion. Recently, wavelet based fusion methods have received great attention as a number of successful wavelet based fusion methods have been reported [Li

et al, 1995; Zhang and Blum, 1997; Lewis et al, 2004]. [Li et al, 1995] used an area-based maximum selection rule and a consistency verification step. [Zhang and Blum, 1997; Lewis et al, 2004] segmented source images into constituent regions and extracted region features as selection rules to guide the fusion process. [Lewis et al, 2004] pointed out the advantages of feature-level fusion over pixel-level. More intelligent semantic fusion rules can be considered based on actual features in the image, rather than on single or a group of pixels. However, since the quality of a feature-level fused image significantly depends on the image segmentation algorithm used, a powerful segmentation algorithm, usually not available for many applications, is required to produce satisfactory fused images. Much research on image fusion is currently focused on pixel level; Feature-level fusion will require the development of robust image segmentation algorithms.

So far, image fusion techniques have not been widely applied to airport luggage inspection although they are extensively harnessed in a variety of domains, such as defense systems, medical imaging, robotics and industrial engineering. By analyzing the characteristics of dual-energy x-ray luggage scans and referring to existing fusion methods, we proposed two new dual-energy image fusion techniques. Detailed descriptions of the two dual-energy image fusion methods will be given in Chapter 6.

2.6 Image Quality Measures

Approaches to image quality evaluation can be classified as objective and subjective measures. For the objective measures parameters are computed to indicate the quality of the captured and processed images, while for subjective measures viewers read the images directly to determine their quality. The ultimate research goal in image quality evaluation is to develop a quantitative measure that can be used as a substitute for the subjective measures in a given application domain.

In this thesis, our discussion on the state of the art in image quality measures is limited to the image enhancement, visualization and fusion domain. In these areas, image quality methods can be grouped into non-reference methods and reference methods, according to whether or not one or more reference images are required for the computation of the quality measures.

Reference image quality measures (RIQM) require using one or more images as references to compute the indexes indicating the quality of the processed images. RIQM associates quality with the deviation from the reference image(s) such as the original or the ideal image. There are several commonly used RIQM, including root mean square error (RMSE), cross correlation, and power signal to noise ratio (PSNR) [Kinape and Amorim, 2003]. Many other metrics such as the ones described in [Lee and Wang, 1999; Elbadawy et al, 1998] were proposed by extending these common measures. More recently, with the rapid growth of image fusion techniques, a variety of reference image quality measures emerged [Xydeas and Petrovic, 2000; Piella, 2004]. [Xydeas and Petrovic, 2000] proposed a measure that evaluates the relative amount of edge

information that is transferred from the input images to the composite image. [Piella, 2004] utilizes local measurements to estimate how well the salient information contained within the sources is represented by the composite image. As in many real-world applications, available good reference images can not be guaranteed. Some researchers concentrate on non-reference image quality measures (NRIQM). NRIQM are calculated by only using information from the images evaluated. Several well-known NRIQM include standard deviation, histogram, and entropy [Xue et al, 2002]. Based on image power spectrum, [Nill and Bouzas, 1992] developed an NRIQM primarily applied for the evaluation of aerial images. They demonstrated a good correlation of their measure with the visual quality of aerial images assessed for their informative value (detection, recognition and identification of man-made objects). In either case, RIQM or NRIQM, the desire is to develop objective image quality measures that correlate well with human evaluations. Although many new metrics have been reported, powerful and robust image quality measures are still lacking in the imaging community. Reasons for this are (1) no enough knowledge on human visual characteristics is available to establish an accurate visual model and (2) the difficulty in using objective measures to describe the process of the human visual evaluation.

Our objective is to identify efficient metrics from various existing IQMs, by comparing their results to airport screeners' evaluations for original and processed x-ray luggage images. These identified metrics will then be used to judge the effectiveness of the image enhancement, visualization and fusion algorithms developed. Objective quality measures selected for the evaluation of the fused versions of dual-energy x-ray images will be discussed in the section on image quality measures in Chapter 6.

2.7 Summary

An extensive literature review for each of the topics investigated in this research has been presented. First, x-ray imaging principles and x-ray luggage inspection systems most commonly used at airports are introduced as the foundation for later analysis of the characteristics of x-ray luggage scans. The exploration of the state of art in image enhancement, image segmentation, pseudo coloring, image fusion and image quality measures, presented in preceding sections, lays a theoretical and practical foundation for our research and aids us in establishing our research direction. For clarity, the key theories and methods that serve as the basis of our research are highlighted as follows:

Image Segmentation: After investigating a variety of theories of image segmentation and available algorithms, taking into account several essential requirements during the process of carry-on luggage inspection, fast entropy-based multilevel thresholding techniques are first determined as our major exploration direction for this topic. Based on [Chang et al., 2002] and [Luo and Tian, 2000], a timesaving multi-thresholding method called Valley method is proposed.

Pseudo Coloring: Theories, experiments and principles proposed in these literatures, [Ware, 1988; Levkowitz and Herman, 1992; Shi et al., 2002; Gonzalez and Woods, 2002], incorporating a series of guidelines on color use derived based on the human perceptual or cognitive characteristics of color, was used as the foundation for the design and development of color scales or color transforms. Our contribution was in the design and development of a set of RGB and HSI-based color transforms that effectively visualize low density threat items in luggage scenes.

Image Fusion: Many successful image fusion algorithms applied in various applications demonstrated that multi-resolution transforms in general, and the wavelet transform in particular, are powerful tools for image fusion. Therefore, we put more of our efforts in the investigation and development of a wavelet-based fusion algorithm suited for dual-energy x-ray scans. Two dual-energy x-ray image fusion algorithms, one is based on local statistical information of the source images and the other is based on wavelet transform have been developed.

Image Quality Measures: To judge the effectiveness of the image enhancement, visualization and fusion algorithms used and developed in this research using objective quality measures, we conducted a comparative study of some chosen IQMs by applying them to original and fused dual-energy x-ray luggage images.

The next few chapters will give detailed discussion and descriptions on the theories and algorithms applied and developed in this research.

3 Gray Level Enhancement

Gray-level enhancement techniques modify the pixel intensity distribution of an input image to generate richer, brighter, clearer, and cleaner versions of the image. This section presents a number of common image enhancement methods for the purpose of increasing contrast and adjusting brightness to make the various components of the luggage scene more distinct in the image.

3.1 Common Gray-Level Enhancement Techniques

In this research, some common image enhancement methods are applied to raw single-energy x-ray images of luggage scenes containing low density threat items.

3.1.1 Linear Contrast Enhancement

The first basic procedure applied to x-ray luggage data is linear contrast enhancement which provides for the "stretching" of the pixel range within a given image so that the pixel values cover a wider dynamic range (or the entire range), providing an enhanced image from the original. Linear contrast enhancement can be mathematically formulated by equation (3.1)

$$g(x,y) = a \times f(x,y) + b, \tag{3.1}$$

where $f(x,y)$ is the value of the original image at pixel location (x,y) and $g(x,y)$ the resulting enhanced image value at the same location; a and b are coefficients to be computed according to the desired range of the output images. Figure 3.1 shows examples of a synthetic and an x-ray luggage scene before and after linear regression. The synthetic image used for illustration of the techniques implemented consists of a simple grouping of very low density geometric shapes of different gray values, most of which are barely apparent to the naked eye.

3.1.2 Gamma Intensity Adjustment

This is a non-linear enhancement method based on the relationship given in equation (3.2), where if $0<\gamma<1$, then the transformation can be seen as a log transformation brightening an image; on the other hand, if $\gamma>1$, then the transformation can be viewed as an exponential transformation darkening an image. I and I' are the original and enhanced images, c a scaling factor.

$$I' = cI^{\gamma}. \tag{3.2}$$

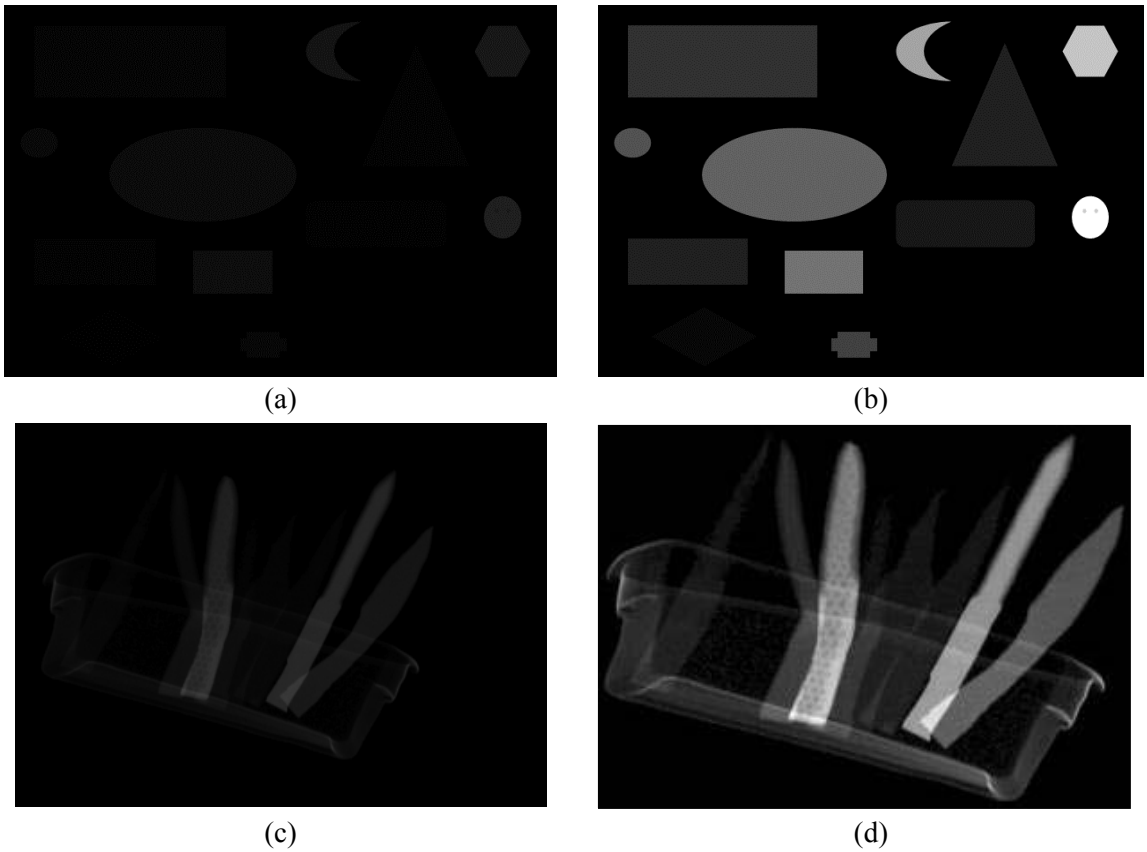

Figure 3.1 Linear contrast enhancement. (a) Synthetic original scene, (b) linearly regressed image of (a), (c) original x-ray luggage scan containing low density threat items, and (d) linearly regressed image of (c).

Results of the gamma adjustment using synthetic data and x-ray luggage image data for gamma values less than 1 are given in Figures 3.2.

3.1.3 Logarithmic Intensity Adjustment

Logarithmic intensity adjustment can take several forms but may typically be expressed as:

$$I' = s \times \ln(I + 1). \tag{3.3}$$

I' and *I* are the output and input gray scale images and *s* is a scaling factor. This type of logarithmic intensity adjustment can produce an enhanced image as shown in Figure 3.3. The left image in each set represents the raw data while the right images show the logarithmically enhanced results.

3.1.4 Standard Measure Technique

Another form of intensity adjustment studied and applied to x-ray images of luggage was the σ-norm or standard measure as expressed in equation (3.4),

$$I' = \frac{I - \bar{I}_s}{\sigma_s}, \tag{3.4}$$

where I is the gray level value of a pixel (x, y) in the original image, $\bar{I}_s$ the mean gray value in a neighborhood s of image I around pixel (x, y) , σ_s the standard deviation of s, and I' is the output value at pixel (x, y) . After the initial values are computed, the resulting image is obtained by linearly scaling initial results to be between 0 and 255. This accounts for potential negative values obtained from equation (3.4). Figure 3.4 illustrates the results from the application of a standard measure technique to an x-ray image of low density knives (soft wood, hard wood, glass of different thickness and color, ceramic, and plastic).

3.1.5 Histogram Equalization

This is a well-known image enhancement technique based on the alteration of the image's histogram characteristics to provide as close to a uniform distribution as possible. Enhancement of an x-ray image obtained by this process is shown in Figure 3.5 (d). A synthetic image in Figure 3.5 (a) and its equalized version in Figure 3.5 (b) are also shown.

3.2 Screener Performance Evaluations

A fully automatic and interactive computer evaluation was designed. A snapshot of one screen of this application is shown in Figure 3.6. A set of 40 x-ray scans containing various low density threat items in different configurations and levels of clutter (see

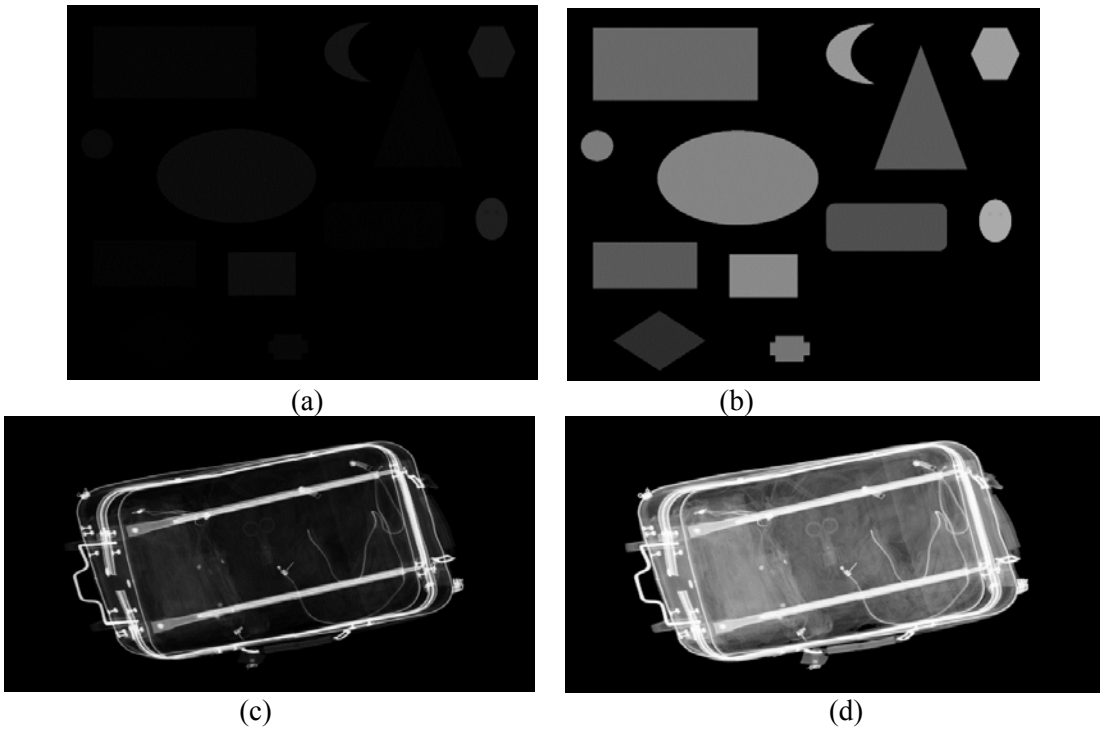

Figure 3.2 Gamma correction. (a) and (c) Synthetic image and original x-ray image, (b) and (d) enhanced versions of (a) and (c), respectively.

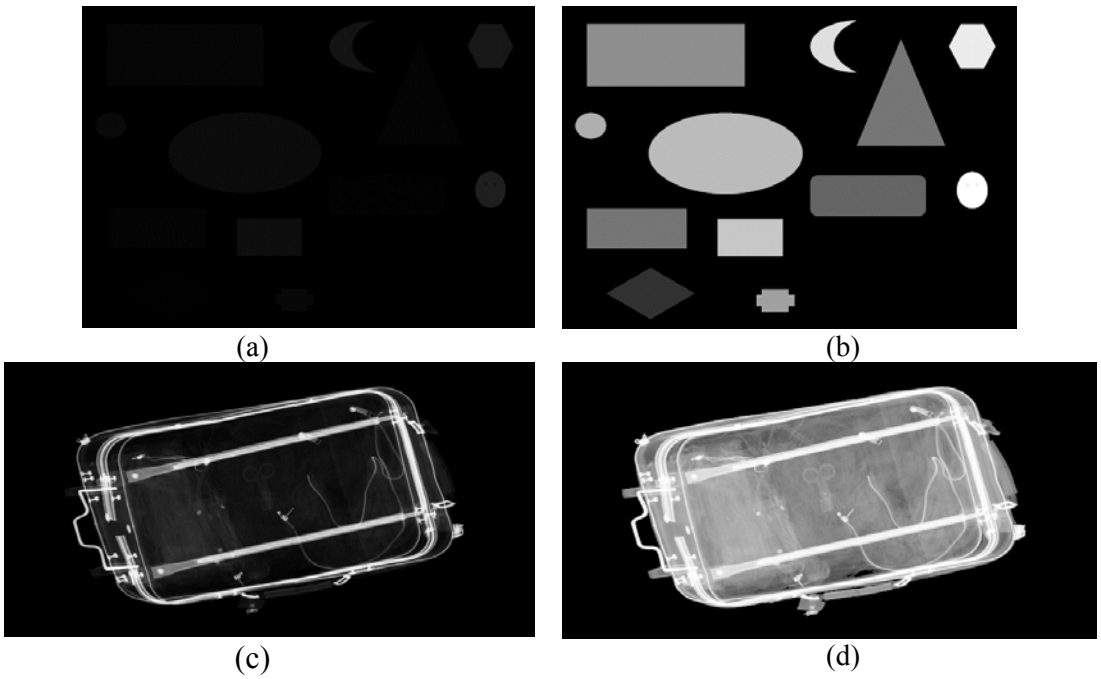

Figure 3.3 Logarithmically enhanced synthetic and x-ray scenes. (a) and (c) original scenes, (b) and (d) logarithmically enhanced versions.

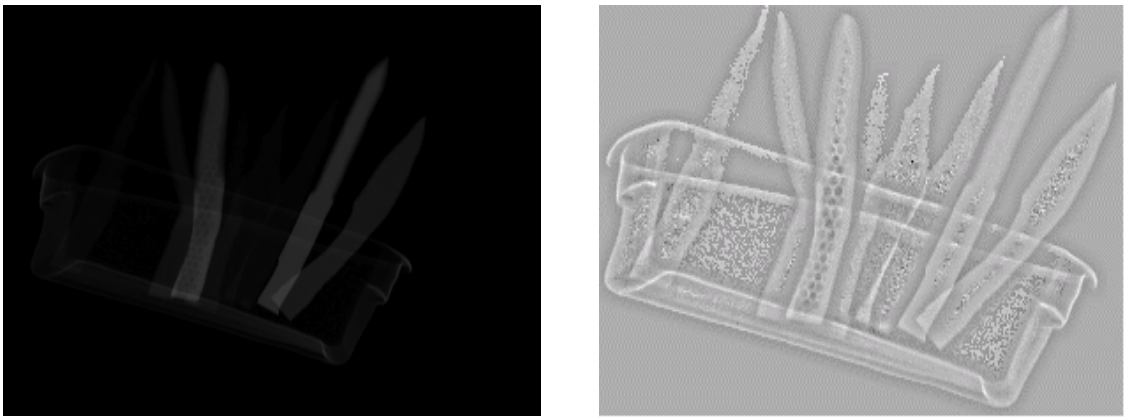

(a) (b)

Figure 3.4 Standard measure technique. (a) Original scan and (b) its standard measure enhanced version.

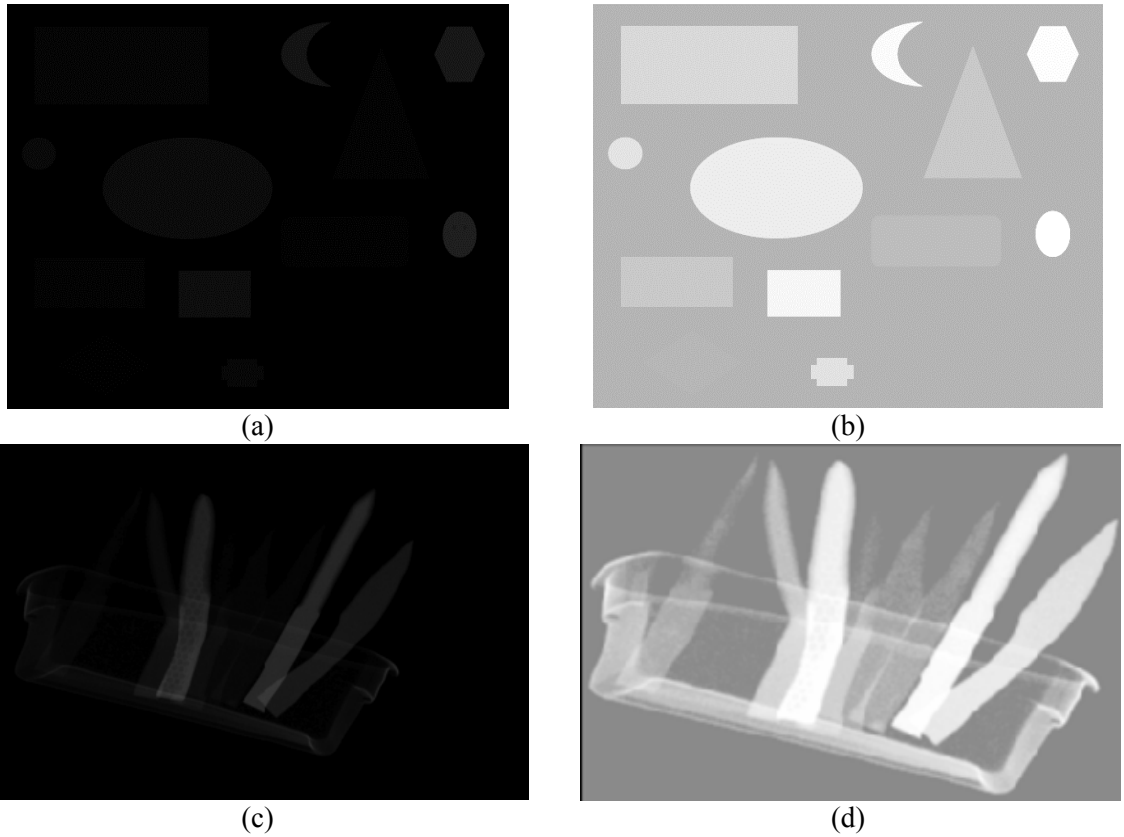

(a) (b)

(c) (d)

Figure 3.5 Histogram equalization performed on (a) synthetic data and (c) x-ray data with corresponding resulting images shown in (b) and in (d), respectively.

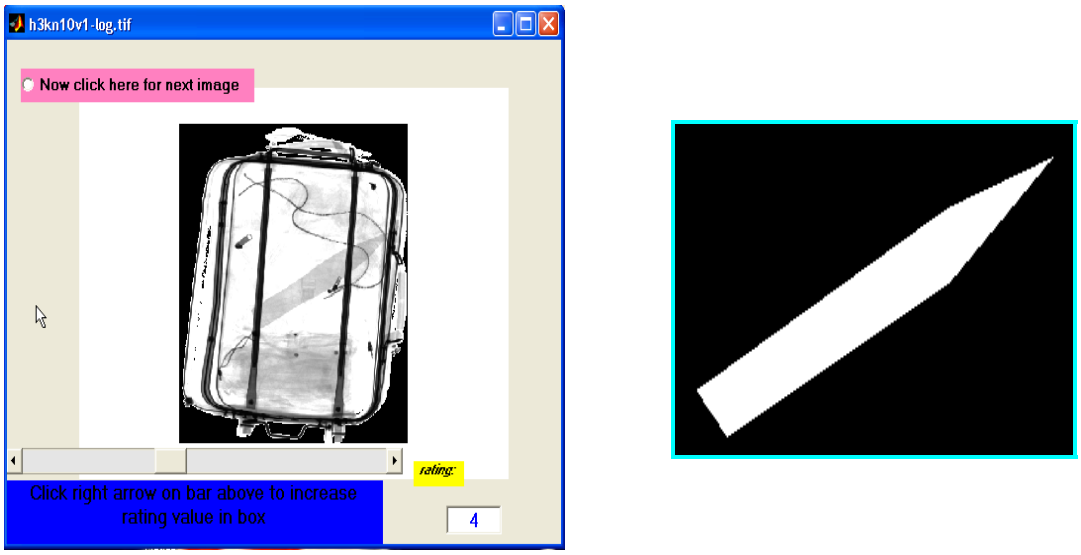

(a) (b)

Figure 3.6 (a) Snapshot of screener evaluation application, (b) binary mask of threat object in image (a) used for confirmation of threat detection.

Section 4.1 of Chapter 4 for more information) were selected. Common image enhancement algorithms as described in Section 3.1 were applied to all original images. All images, raw and processed, were shown to screeners in random order selected using a random number generator. The screeners were asked not only to affirm seeing a threat but to also point and click on the threat to ensure they saw the actual threat. The screeners were also asked to rank the images in terms of their visual clarity and ease of interpretation, which is an important fact in relieving boredom and keeping the screener's level of concentration relatively high. The evaluation sessions were conducted at McGhee Tyson Airport in Knoxville, Tennessee and involved a total of 40, Transportation Security Administration (TSA) luggage screeners. Figure 3.6(a) shows an example of a typical image used in this evaluation. This particular image contains a low density, glass knife at the center of the luggage and was enhanced by the logarithm transform.

Five types of information were collected for each image shown: (1) did the screener see the threat object in the image? (2) if so, how many (1 or 2) threat items were seen, (3) could the screener click on the location of the first threat item correctly? (4) if two threat items were indicated, could the screener correctly click on the location of the second threat object, (5) a rating (from 1 to 10, with 10 being best) of "how helpful" the screener believed the displayed image was in detecting the threat object. The ability of the screener to correctly click on the threat item location within the luggage was determined through use of a binary mask image. Figure 3.6(b) shows the mask image for the glass knife of Figure 3.6 (a). When the screener clicks on a specific (x, y) location in the image

being evaluated, the program checks the same location in the corresponding mask image. If this pixel location has a value of 1, the answer is recorded as being correct.

The information indicated in the previous paragraph was recorded in spreadsheet format and compiled as graphical representations for the entire set of data collected. A number of graphics were generated. Figure 3.7 shows the mean visual rating for each enhancement procedure and the original image. A significant increase of the screeners' rating values between the original image and the processed data is revealed. An average of 170% visual improvement was reported by screeners. All the enhancements were rated considerably higher than the original. A more quantifiable variable is shown in Figure 3.8. This graph illustrates the percent of correctly detected threat objects seen in the original and various types of enhancement methods tested. An increase in threat detection rate of 40 to 62%, as compared to the detection rate from the raw images, was achieved.

3.3 Summary

Some common image enhancement techniques are selected as candidates to enhance single-energy x-ray images of carry-on luggage. These techniques are introduced and analyzed and their features are underscored. In addition, through visual interpretation, and more importantly through testing on TSA airport screeners, it is shown that common image enhancement techniques are very valuable tools in increasing the rate of low density threat detection in x-ray luggage scans. A significant increase of up to 62%, as compared to the original image, in the rate of threat detection was obtained when enhanced/decluttered data was used by screeners. Feedback from screeners also rated the processed data, on the average, as 170% more helpful in detecting threats than the raw data.

Furthermore, we believe that if an appropriate series of methods consisting of several gray-level image enhancement approaches is applied to x-ray luggage images, the possibility that threat items are highlighted or differentiated in the output image will be greater compared with applying individual method only. Pseudo coloring of the processed gray scale data is also pursued for better data visualization, increased screeners' alertness, and longer attention retention. Chapter 5 will detail the efforts on pseudo coloring of the processed gray scale data

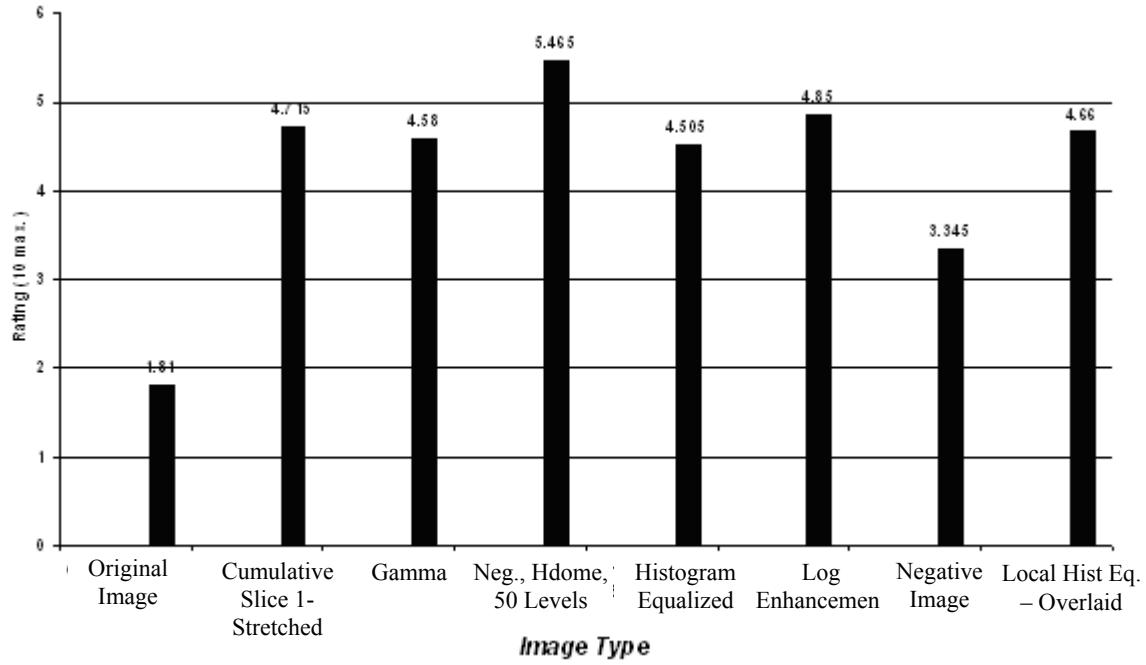

Figure 3.7 Mean opinion scores (10 being best) by screeners of original image and each of the differently-processed images

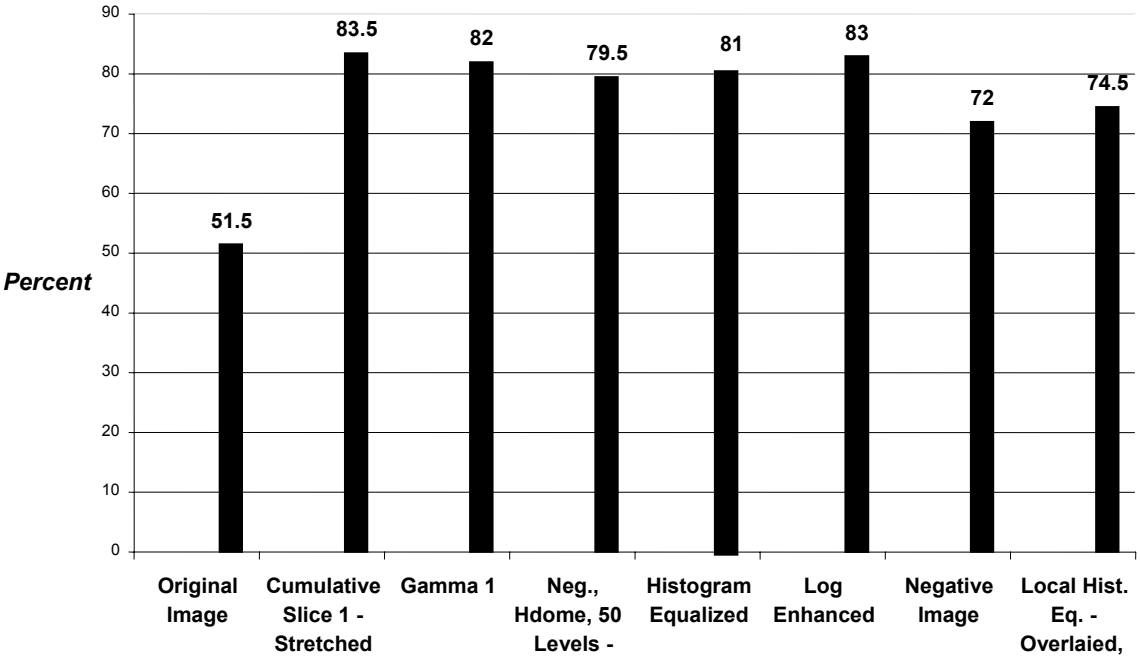

Figure 3.8 Percent of screeners who actually detected the right threat, sorted by image type.

4 Image Segmentation

Image segmentation techniques are applied to extract objects of interest from a given luggage scene. Through the use of image segmentation techniques, a relatively complex luggage scene can be separated into several simple sub-scenes, which help bring up items that are invisible or unclear in the original scene for the scene to be easily and accurately interpreted by screeners. Because of the reasons presented in Section 2.3.2, the focus has been on multilevel image thresholding techniques. In this chapter, we first study and apply image hashing algorithms to x-ray luggage images. Entropy-based multilevel thresholding is then presented. A selected fast entropy-based multilevel thresholding algorithm, iterated conditional modes (ICM), and a developed entropy-based multilevel thresholding algorithm, Valley method, are emphasized.

4.1 Image Hashing Algorithms

Image hashing is performed via intensity slicing and involves selecting some portion of the range of pixel values of an original image and producing image slices containing only the selected portion of that pixel range. The objective is to progressively de-clutter an image scene and produce in separate image slices objects of different intensity values. Intensity slicing can be performed in varying manners. The following introduces several methods we chose and applied for the decluttering of x-ray luggage scenes.

4.1.1 Equal Interval Image Slicing

With this method of slicing, equal width slices are used generally covering the entire dynamic range of the image. Figure 4.1 (a) depicts a simple graphical representation of this process. Each one of the slices produced can also be stretched to reveal items previously hidden by the lack of dynamic range. An example of six-slice image hashing at equal intervals is given in Figure 4.1 (b).

4.1.2 Cumulative Image Slicing

This method of intensity slicing is similar to equal interval slicing in that a number of equal intervals are selected first. Here however, the slices are cumulative. For example, if the original image is divided into six sub-images, the first image slice shows all pixels in sub-image 1, the second slice all pixels in sub-images 1-2, and so on. An example of result obtained from this technique is shown in Figure 4.2. Original image is the same as seen at the top of Figure 4.1 (b).

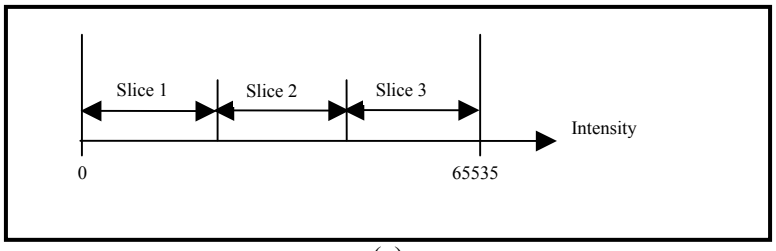

(a)

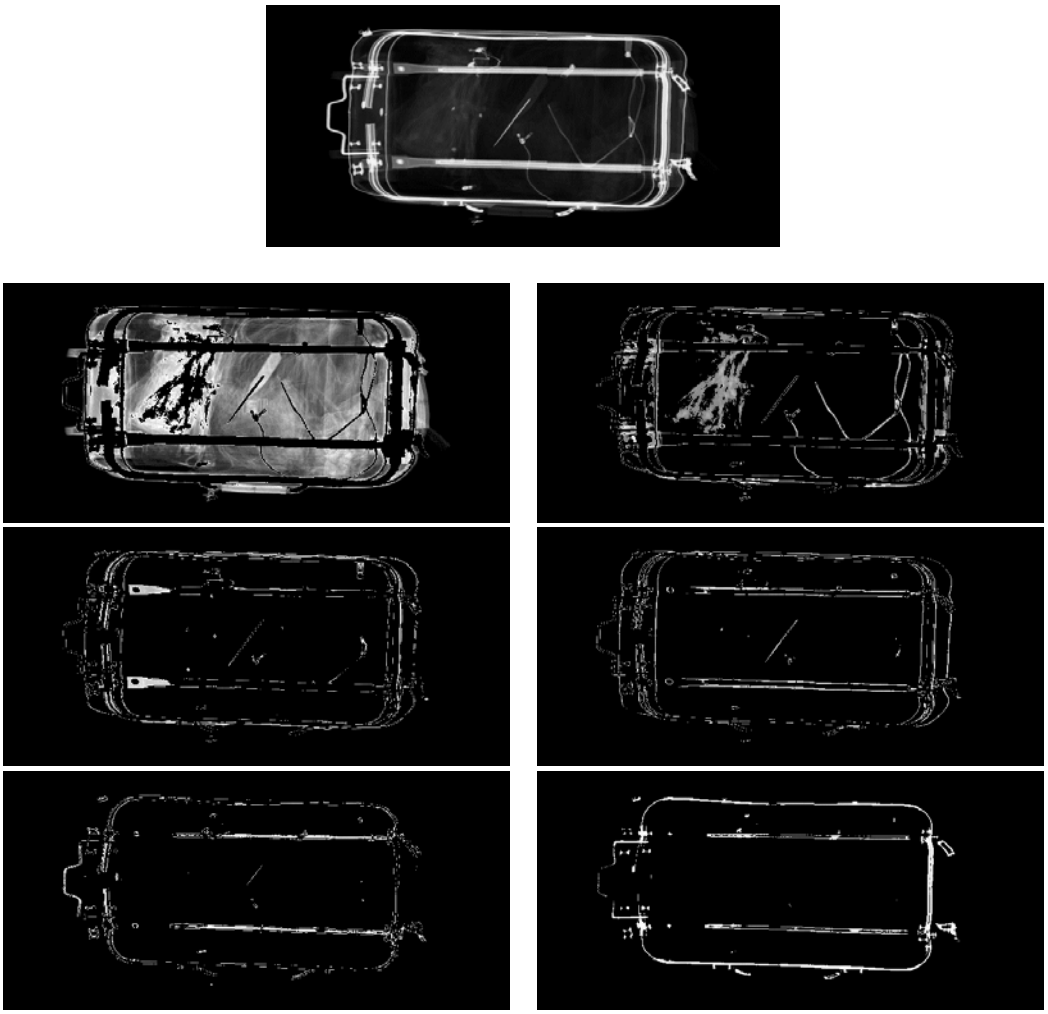

(b)

Figure 4.1 Equal interval image slicing. (a) Illustrative schematic for the equal interval image hashing algorithm, (b) result of a six-slice equal interval image hashing applied to the original image shown on top.

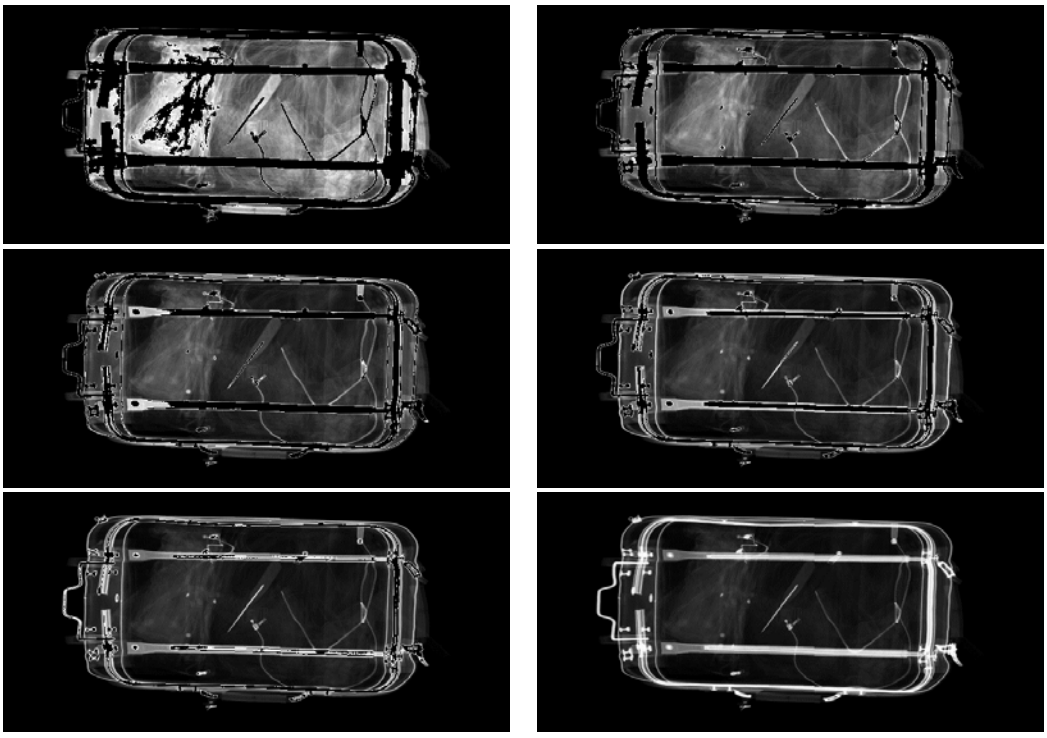

Figure 4.2 Result of six-slice cumulative image hashing of original images shown in Figure 4.1.

4.1.3 H-Domes Image Slicing

H-domes slicing [Vincent, 1993; Shao and Chen, 2001] is slightly different from the two previous hashing techniques and involves the use of the original image as a mask. Markers are constructed by subtracting a fixed value *h* from the mask. The mask is morphologically reconstructed using the marker and the reconstructed image is subtracted from the mask, providing *h* domes of the original image. Lastly, the *h* domes are structurally opened to remove small grains. Figure 4.3 shows a graphical representation of the h-domes concept and Figure 4.4 illustrates the algorithm application to an 8-bit original x-ray image (top left) with 50 gray levels for the domes.

4.2 Entropy-Based Multilevel Thresholding Approaches

Most existing entropy-based thresholding methods are able to automatically search thresholds using a particular entropy criterion. Pun [Pun, 1980], Kapur et al [Kapur, 1985], Pal and Pal [Pal and Pal, 1989], and Chang et al [Chang et al., 1994] thresholding methods were proposed for the bilievel case and all of them can automatically generate a single desired threshold. Pun [Pun, 1980] and Kapur et al [Kapur, 1985] methods maximize global entropies to obtain the desired threshold; Pal and Pal [Pal and Pal, 1989] approach finds the optimal threshold that maximizes the local or joint entropy. The basic idea behind these methods is to maximize the entropies derived from Shannon's formula such that the image after thresholding preserves the maximum information. Chang et al [Chang et al., 1994] thresholding method minimizes relative entropies to get the desired threshold. That is, the threshold segments an image such that the resulting thresholded image best matches the original image. All these methods can be easily extended to the multilevel thresholding case; however, computational load increases exponentially due to an exhaustive search. To deal with the problem, many researchers have been exploring fast multilevel thresholding approaches. Several fast methods, for instance, were proposed in [Luo and Tian, 2000; Chang et al., 2002; Lin, 2001]. Extending [Luo and Tian, 2000; Chang et al., 2002], we suggest a timesaving multi-thresholding method called Valley method that will be described in Section 4.2.2.

4.2.1 The ICM Method

The ICM method proposed by [Luo and Tian, 2000], is one of the existing timesaving entropy-based multi-thresholding methods we selected and extended for the segmentation of single-energy x-ray luggage scans.

4.2.1.1 Maximum Entropy Criterion

The ICM method uses the global entropy proposed by Kapur et al [Kapur, 1985] as a criterion to find thresholds. The Kapur's global entropy in the multilevel case is given in (4.1).

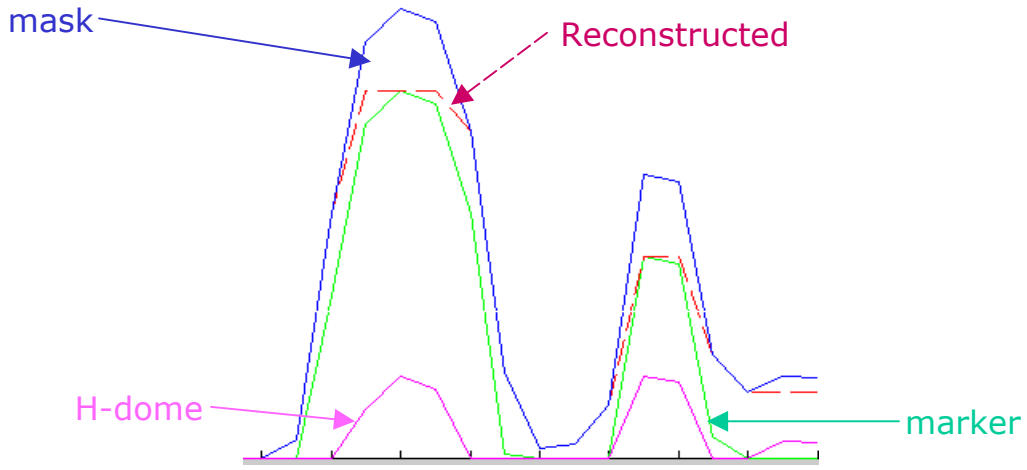

Figure 4.3 Graphical representation of the h-domes methodology.



(a) (b)

Figure 4.4 Result (b) of the H-domes algorithm applied to the negative of an 8-bit original x-ray image (a) with 50 gray levels for the domes.

$$H(s_1,s_2,...,s_k) = \log(\sum_{i=0}^{s_1} p_i) + \log(\sum_{i=s_1+1}^{s_2} p_i) + ... + \log(\sum_{i=s_k+1}^{L-1} p_i) - \frac{\sum_{i=0}^{s_1} p_i \log p_i}{\sum_{i=0}^{s_1} p_i} - ... - \frac{\sum_{i=s_k+1}^{L-1} p_i \log p_i}{\sum_{i=s_k+1}^{L-1} p_i}, \quad (4.1)$$

where $s_1, s_2, ..., s_k$ are thresholds to be found to satisfy

$$(s_1,s_2,...,s_k) = \arg(\max_{s_1,s_2,...,s_3} H(s_1,s_2,...,s_k)) \quad (4.2)$$

4.2.1.2 ICM Algorithm

The ICM is a statistical iterative method developed based on Bayes' theorem and Markov random field [Besag, 1986]. It converges rapidly although it generally does not converge to the global optimal state [Luo and Tian, 2000]. The initial state of ICM method is of critical importance to the final state converged to. If the initial state is close to the global optimal state, it is very likely that ICM will converge to the global optimal state.

Let *n* be the number of classes needed; min_i and max_i be the parameters of the *ith* class. The following conditions are satisfied, $\min_1 = 0$, $\max_n = \max_gray$ and $\max_{i-1} = \min_i$ for any *i* between *2* and *n*. The algorithm proceeds as follows:

1. Initialize the value of min_i, $inter1_i$, $inter2_i$ and max_i by using the initialization algorithm stated below.
2. For each class *i* from *1* to *n-1*, change the value of max_i between min_i and max_{i+1} to find the max_i maximizing (4.1).
3. Repeat step 2 until there are no changes (experiments showed the algorithm converged to the stable state after 3 to 5 iterations, irrespective of the number of classes and the number of gray levels).
4. Set threshold values to be $max_1, \ldots, max_{n-1}$.

4.2.1.3 Initialization Algorithm

Since the final state of a system depends strongly on the initial state, the determination of the initial state is an important step for the ICM method. Luo et al [Luo and Tian, 2000] proposed an initialization algorithm to get good initial values.

1. Find the gray levels that correspond to local minima and local maxima (valleys and peaks) from the histogram of the image in a single scan and store them into two arrays, *loc_min* and *loc_max*. The entries in *loc_min* and *loc_max*

satisfy $loc_\min[i-1] < loc_\max[i] < loc_\min[i]$. Gray levels between two adjacent local minima are called a threshold component.

2. Merge some of the adjacent threshold components that have the form of *"N"* and *"И",* as shown in Figure 4.5, and meet the following conditions:

   - Conditions to merge for the form of "*N*":
   hist(loc_max(i))-hist(loc_min(i)) < hist(loc_max(i+1))-hist(loc_max(i))
   and *loc_max(i+1)-loc_max(i)<max_inter max_inter=max_hist/(2*classnum)*
   - Similar conditions can be set for the form "*И*".
   - Repeat the process until no merge can be made.

3. If the number of threshold components is still greater than the number of classes needed, proceed to further merges by finding the threshold component with the smallest probability and merge it with the adjacent threshold component that has smaller probability.

4.2.2 The Valley Method

A timesaving multi-thresholding method, Valley method is proposed as an extension to [Luo and Tian, 2000] and [Chang et al., 2002] algorithms. Assume *N* is the number of classes in a segmented image. The theoretical base of this method is that the maximum entropy of a segmented image is obtained when *N* classes have the same probabilities of $\frac{1}{N}$ [Chang et al., 2002].

4.2.2.1 Optimal Thresholds

The entropy of a segmented image is the sum of the entropies of the *N* classes. The general form to calculate the entropy of the segmented image is given in (4.3).

$$H(P_1^*, P_2^*, ..., P_N^*) = -P_1^* \log P_1^* - P_2^* \log P_2^* - ... - P_N^* \log P_N^*, \tag{4.3}$$

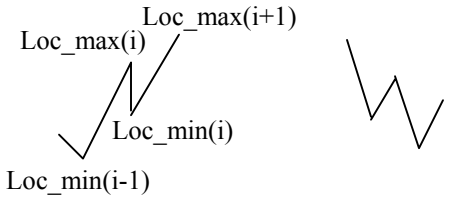

Figure 4.5 Form "*N*" on the left and form "*И*" on the right.

where P_n^* $n = 1,2,...,N$ is the sum of probabilities of gray levels falling into the *nth* class and $\sum_{n=1}^{N} P_n^* = 1$. According to the derivation of [Chang et al., 2002], the maximum value of (4.3) is obtained when $P_n^* = \frac{1}{N}$ $n = 1,2,...,N$. Thus, the maximum entropy of a segmented image is obtained when N classes have the same probability $\frac{1}{N}$; that is, the optimal thresholds are found when they result in the N classes having the same probabilities of $\frac{1}{N}$.

4.2.2.2 Valley Algorithm

Based on the preceding theory, the Valley method is developed as follows:

1. Find the gray levels corresponding to the local minima and local maxima (valleys and peaks) of the histogram of an image in a single scan and store local minima and local maxima into two separate arrays, *loc_min* and *loc_max*. The entries in *loc_min* and *loc_max* satisfy $loc_\min[i-1] < loc_\max[i] < loc_\min[i]$ (This step is the same as the first step in the initialization of the ICM method).

2. Calculate the cumulative probability function, FT, by using the histogram of the image. Select the gray-levels *loc_min(i)* and loc_min(i+1), for $1 \le i \le (\ length(loc_\min) - 1\ )$, that meet *FT(loc_min(i))<=* $n * \frac{1}{N}$ and *FT(loc_min(i+1) >=* $n * \frac{1}{N}$ for the nth class *(1<=n<=N-1)* as threshold candidates. Thus there are two threshold candidates to determine each class *n*, *1<=n<=N-1*.

3. Combine the candidate thresholds and calculate the entropy for each combination using (4.3).

4. Choose the combination that produces the maximum entropy as the desired threshold set.

4.3 Experimental Results

The ICM method [Luo and Tian, 2000] and the Valley method were applied to segment single-energy x-ray carry-on luggage scans. Three representative single-energy x-ray luggage scans (8-bit images), containing low-density and high-density threats, were segmented with the two methods. Figures 4.6 (a), (b) and (c) show the three images. Their corresponding histograms are shown in Figures 4.7 (a), (c) and (e).

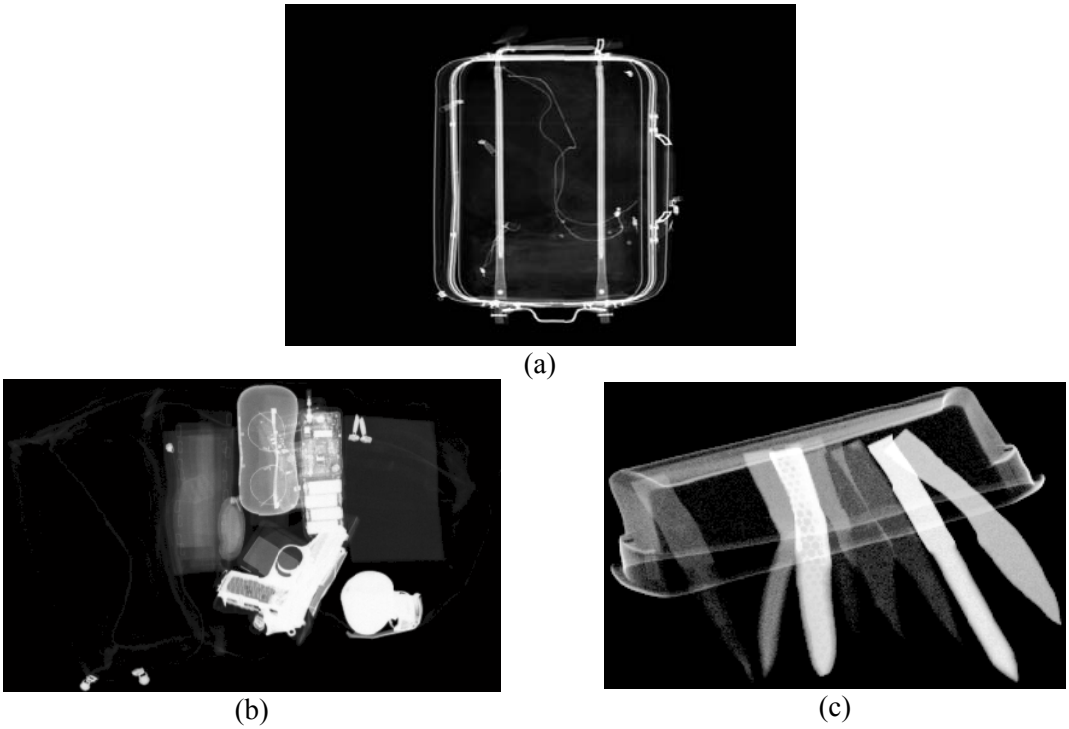

(a) (b) (c)

Figure 4.6 Three representative x-ray luggage scans used for segmentation. (a) Scan containing a low-density threat, a narrow soft wood knife, (b) scan containing high-density threats, gun and grenade, and (c) scan containing various low-density knives.

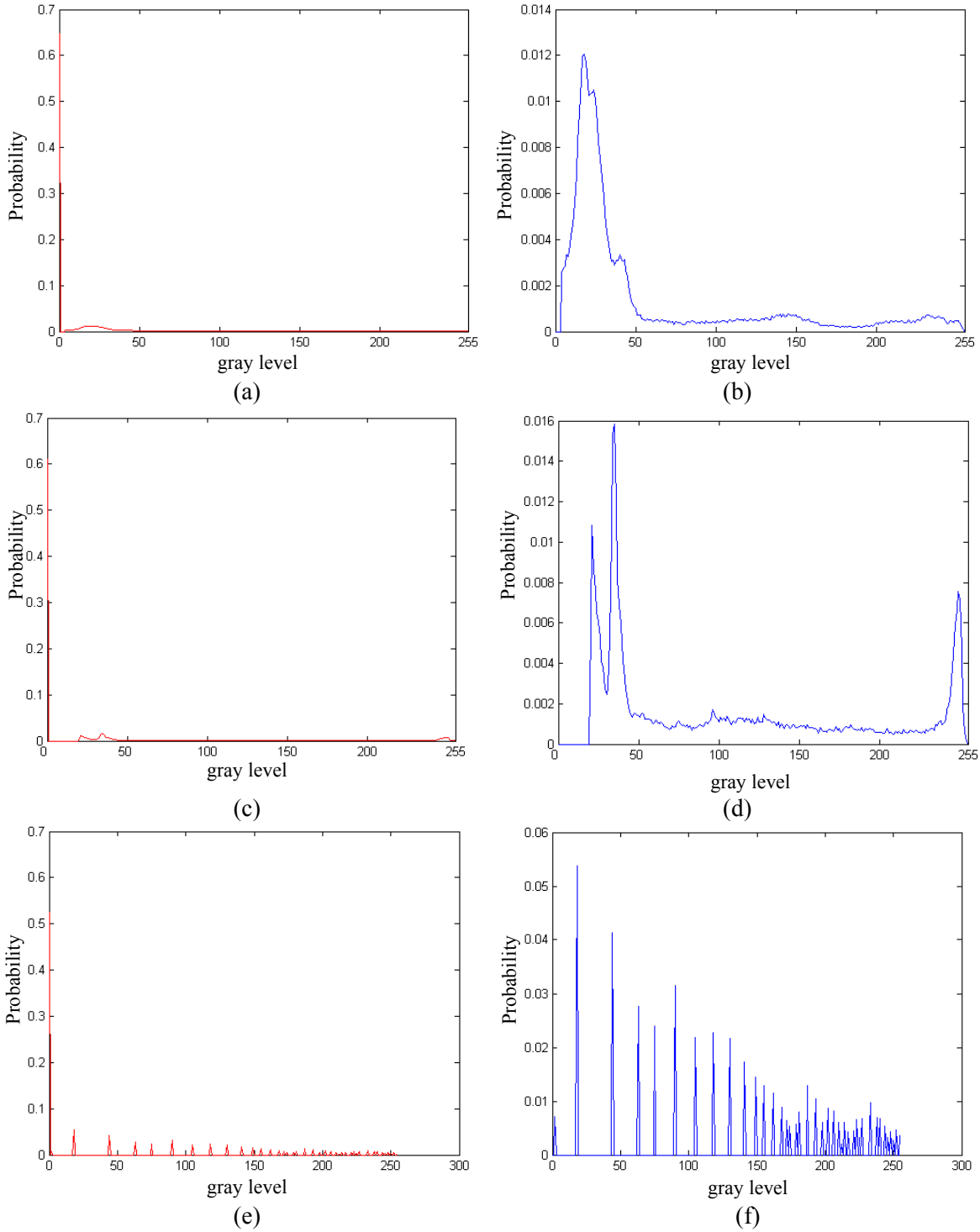

Figure 4.7 Histograms of x-ray scans. (a), (c) and (e) corresponding histograms of the three x-ray scans shown in Figures 4.9 (a), (b) and (c), (b) (d) and (f) the counterparts of (a) (c) and (e) without the components of gray level 0.

Since the background (gray level 0) accounts for a large percentage of 60-70% in the three x-ray luggage scans, to show the shape of the histogram clearly, the component of gray level 0 is removed. The histograms of Figures 4.7 (b), (d) and (f) reflect that operation. Based on our experiments, the number of classes was set to 5, 6 or 7 to segment single-energy x-ray luggage scans.

4.3.1 The ICM Method

Tables 4.1, 4.2 and 4.3 show the initial and final states obtained to segment the images shown in Figures 4.6 (a), (b) and (c) for the case of 5 classes, respectively. Corresponding resulting slices are shown in Figures 4.8, 4.9 and 4.10.

4.3.2 The Valley Method

A simulated image containing 5-graylevel objects, as shown in Figure 4.11, was segmented by using the Valley method and the ICM method. Resulting slices of the Valley method and the ICM method are shown in Figures 4.12 and 4.13, respectively. The results clearly demonstrate that the Valley method is more successful in segmenting the image. Specifically, the Valley method differentiated all five objects, including the background of the image.

The Valley method was also examined by segmenting the three representative images given in Figure 4.6. Classes were set to 5 for this experiment. Because the background (gray level 0) takes a large percentage of 60-70% in each of the images, the probability of gray level 0 was subtracted when $P_n^* \quad n = 1,2,...,N$ were computed. That is, $P_n^* = (1 - p_0)/5 \quad n = 1,2,...,5$ for the case of 5 classes, where p_0 is the probability of gray level 0 in an input image. The thresholds found for the three representative images shown in Figures 4.6 (a), (b) and (c) for the case of 5 classes are given in Table 4.4. The corresponding resulting slices are shown in Figures 4.14, 4.15 and 4.16.

The Valley method provides faster computation speed compared to the ICM method, giving acceptable results. Results shown in Figures 4.15 and 4.16 demonstrate that the Valley method efficiently differentiates the different contents in the x-ray scans. From the result shown in Figure 4.14, however, it seems that the shape of the histogram of an input image affects the result of the Valley method more than the result of ICM. Therefore, in order to obtain satisfactory results for different input images using the valley method, there are two possible solutions (1) preprocessing the input image before the use of the Valley method; (2) improving Step 2 of the Valley method (see Section 4.2.2.2). That is, improving the searching method of threshold candidates from Valleys.

Table 4.1 Initial and final states obtained for the image shown in Figure 4.6 (a) for the case of 5 classes.

Thresholds	1	2	3	4
Initial State	1	61	107	147
Final State	48	98	146	203

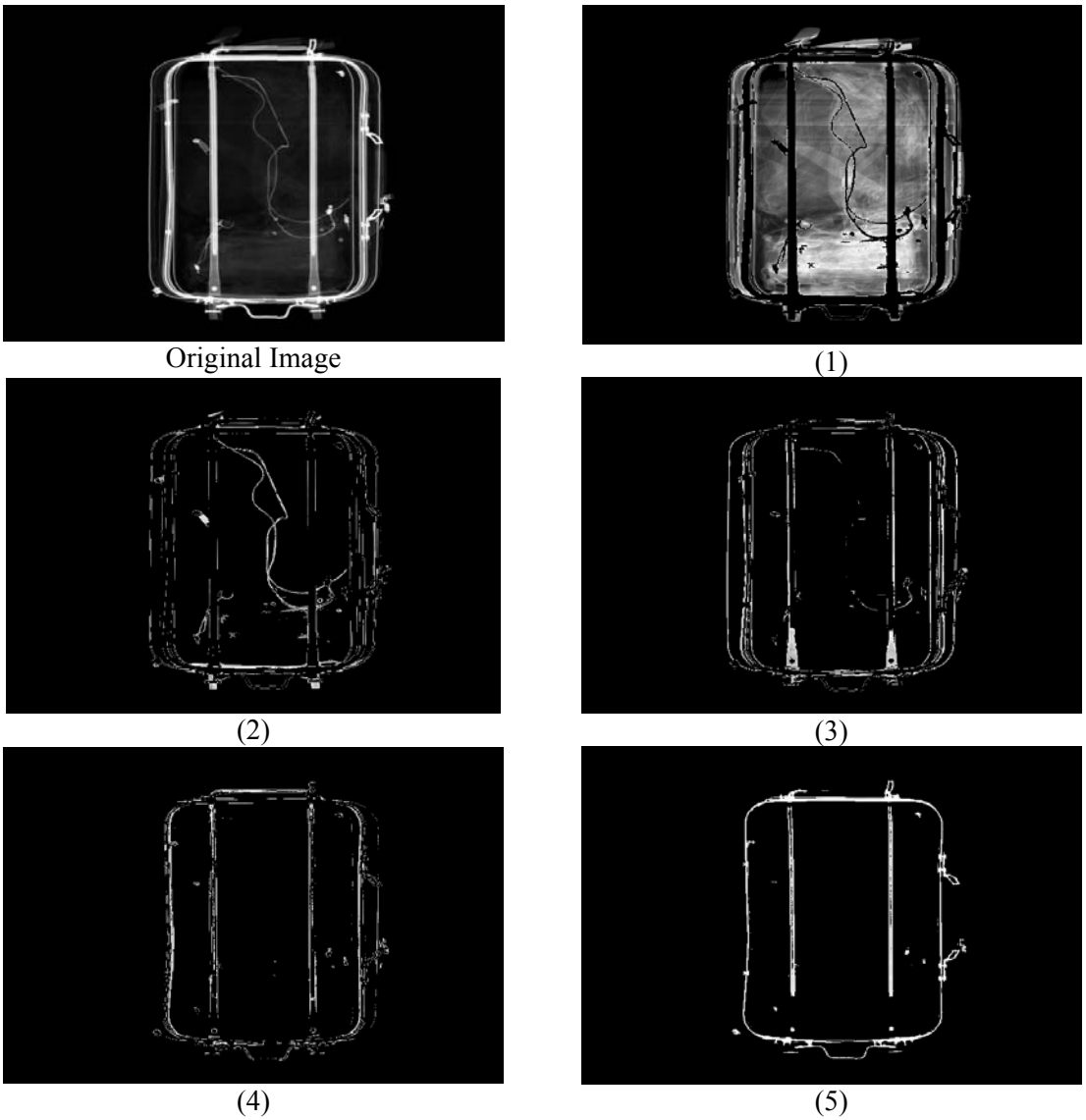

Original Image (1) (2) (3) (4) (5)

Figure 4.8 Resulting slices generated by using the resulting thresholds shown in Table 4.1 for the case of 5 classes.

Table 4.2 Initial and final states obtained for the image shown in Figure 4.6 (b) for the case of 5 classes.

Thresholds	1	2	3	4
Initial State	1	30	83	114
Final State	26	64	113	177

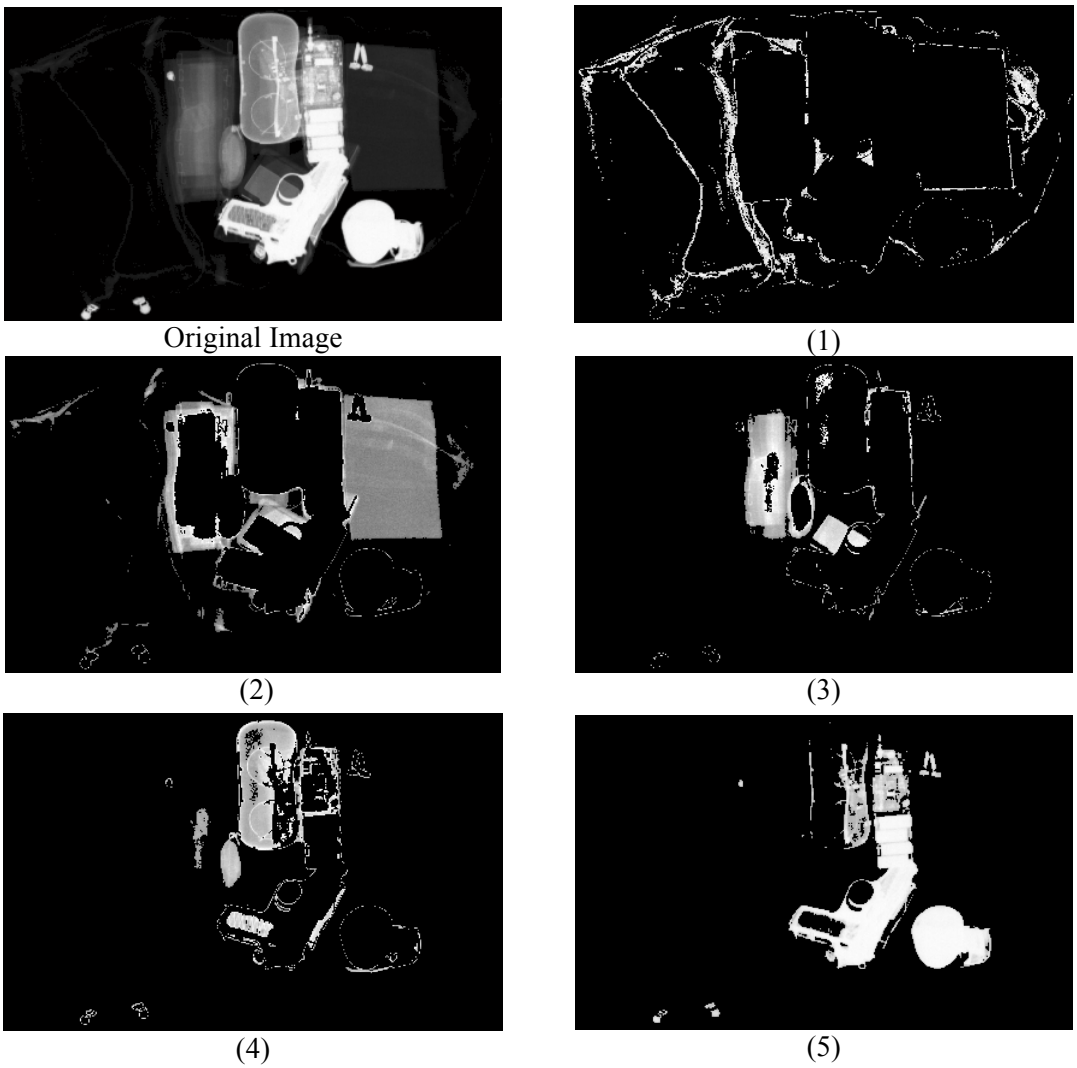

Figure 4.9 Resulting slices per class generated using the resulting thresholds shown in Table 4.2 for the case of 5 classes.

Table 4.3 Initial and final states obtained for the image shown in Figure 4.6 (c) for the case of 5 classes.

Thresholds	1	2	3	4
Initial State	1	64	91	180
Final State	1	75	89	206

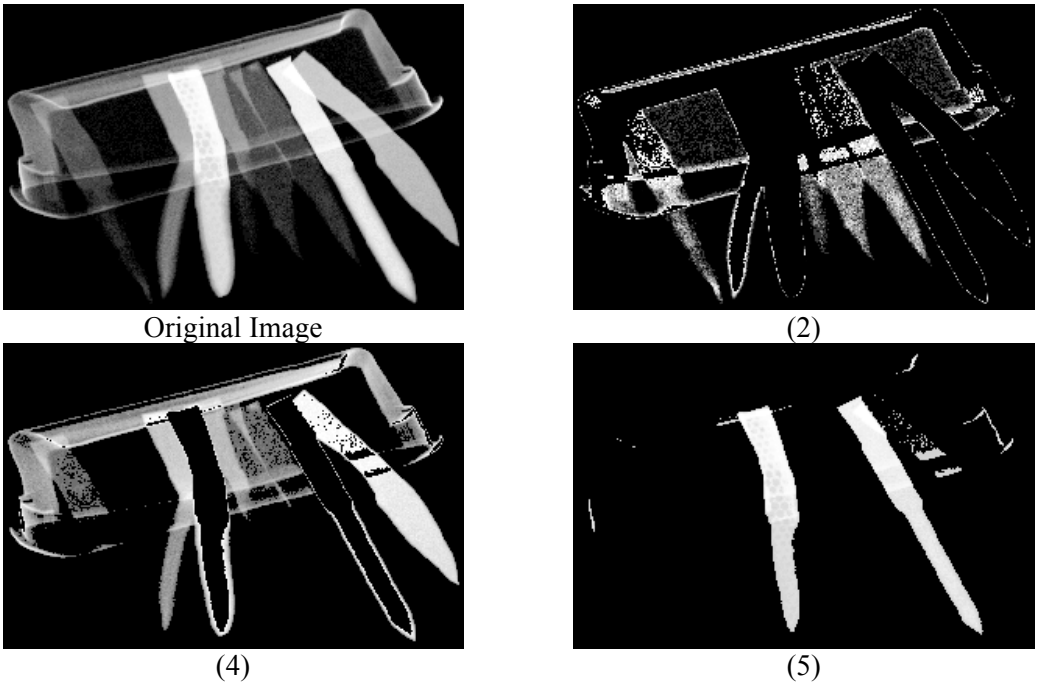

Original Image (2) (4) (5)

Figure 4.10 Resulting slices generated by using the final state of the thresholds shown in Table 4.3 for the case of 5 classes.

Table 4.4 Thresholds obtained by using the Valley method to segment (a) the image shown in Figure 4.6 (a), (b) the image shown in Figure 4.6 (b), (c) the image shown in Figure 4.6 (c), for the case of 5 classes.

	Thresholds			
(a)	8	21	35	100
(b)	30	46	114	198
(c)	43	104	154	205



Figure 4.11 Simulated image with 5 gray level objects, 0,128, 166, 192 and 255.

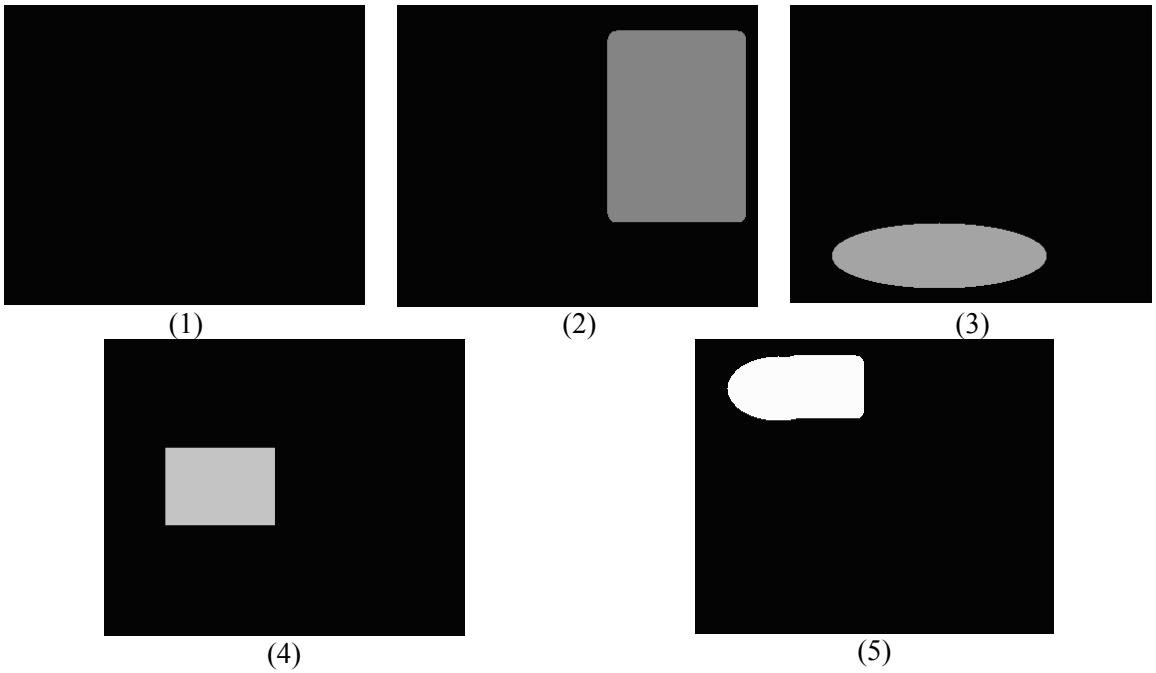

Figure 4.12 Resulting slices per class produced by using the valley method.

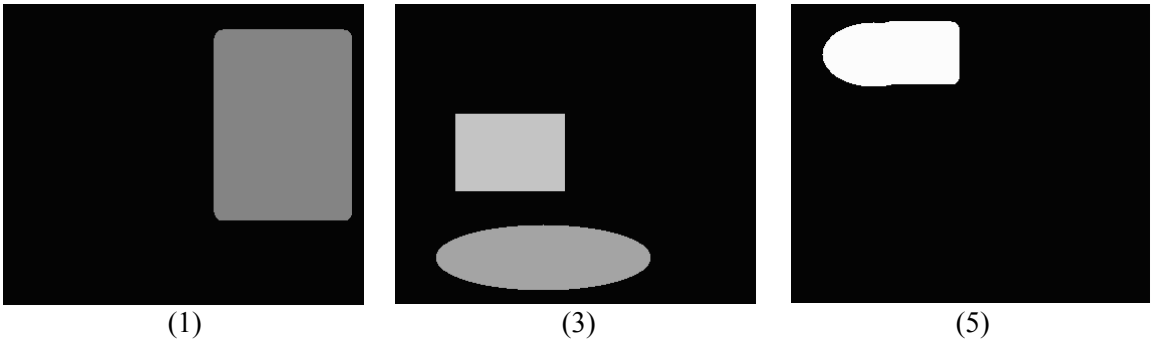

Figure 4.13 Resulting slices produced by using the ICM method.

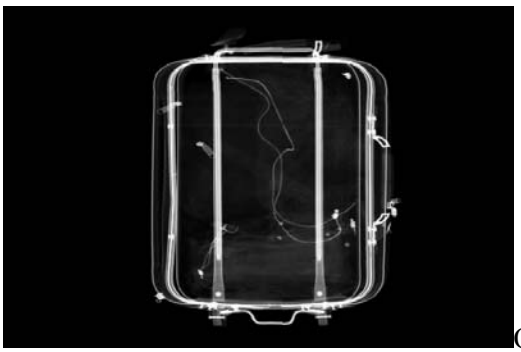

Original Image

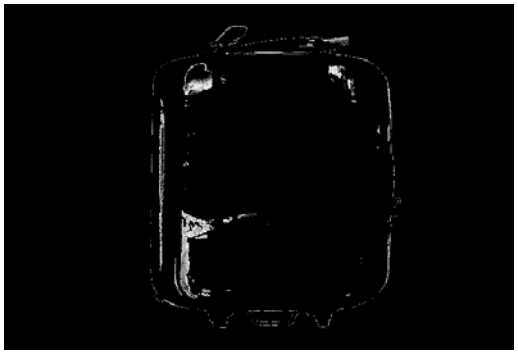

(1)

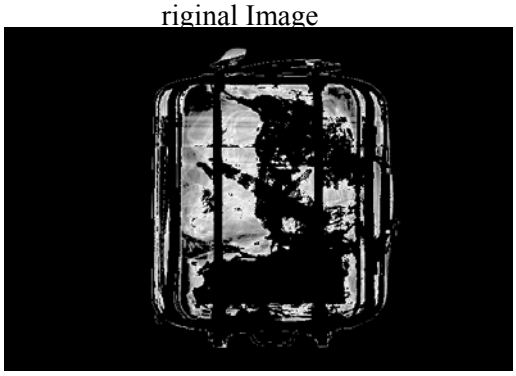

(2)

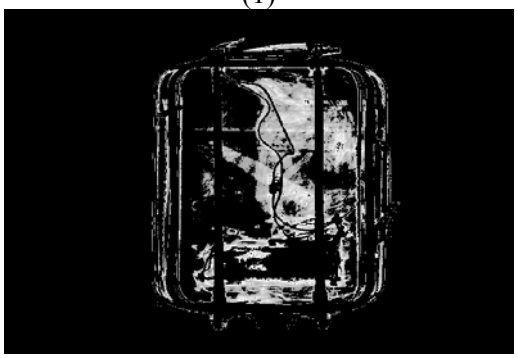

(3)

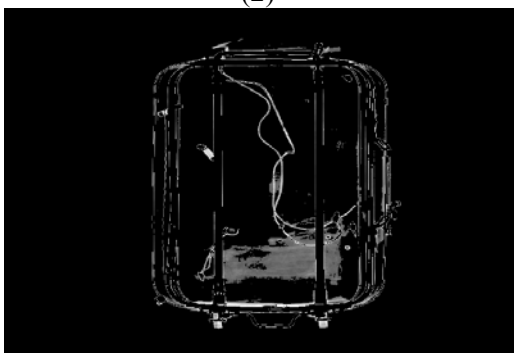

(4)

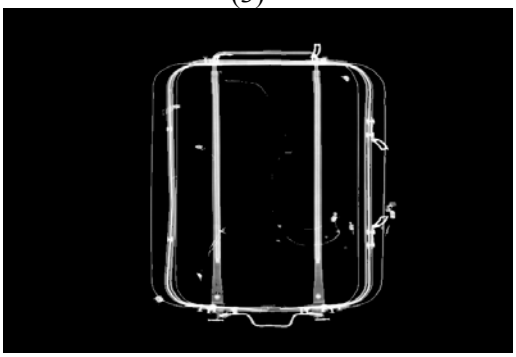

(5)

Figure 4.14 Resulting slices per class generated by using the thresholds shown in Table 4.4(a) for the case of 5 classes.

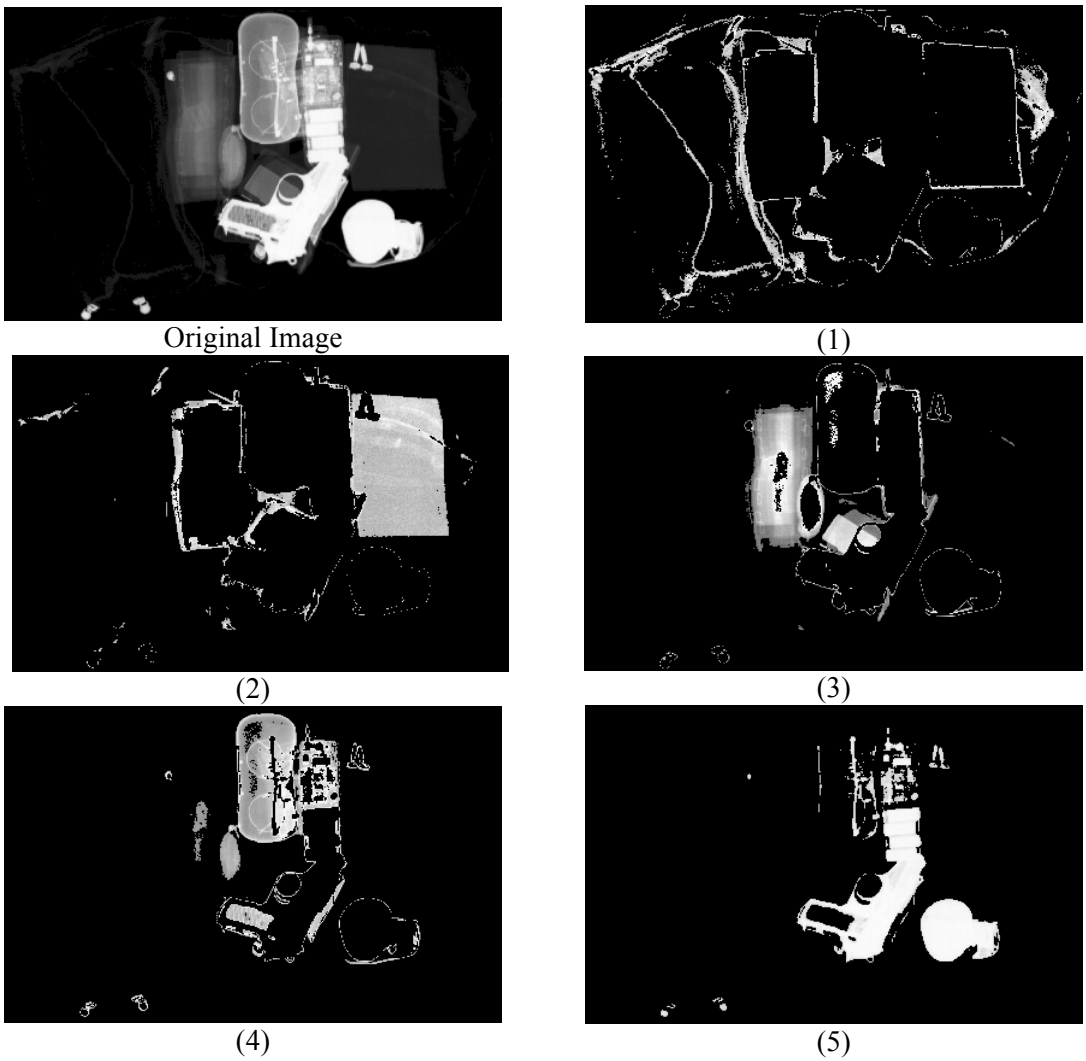

Original Image (1) (2) (3) (4) (5)

Figure 4.15 Resulting slices per class generated by using the thresholds shown in Table 4.4(b) for the case of 5 classes.

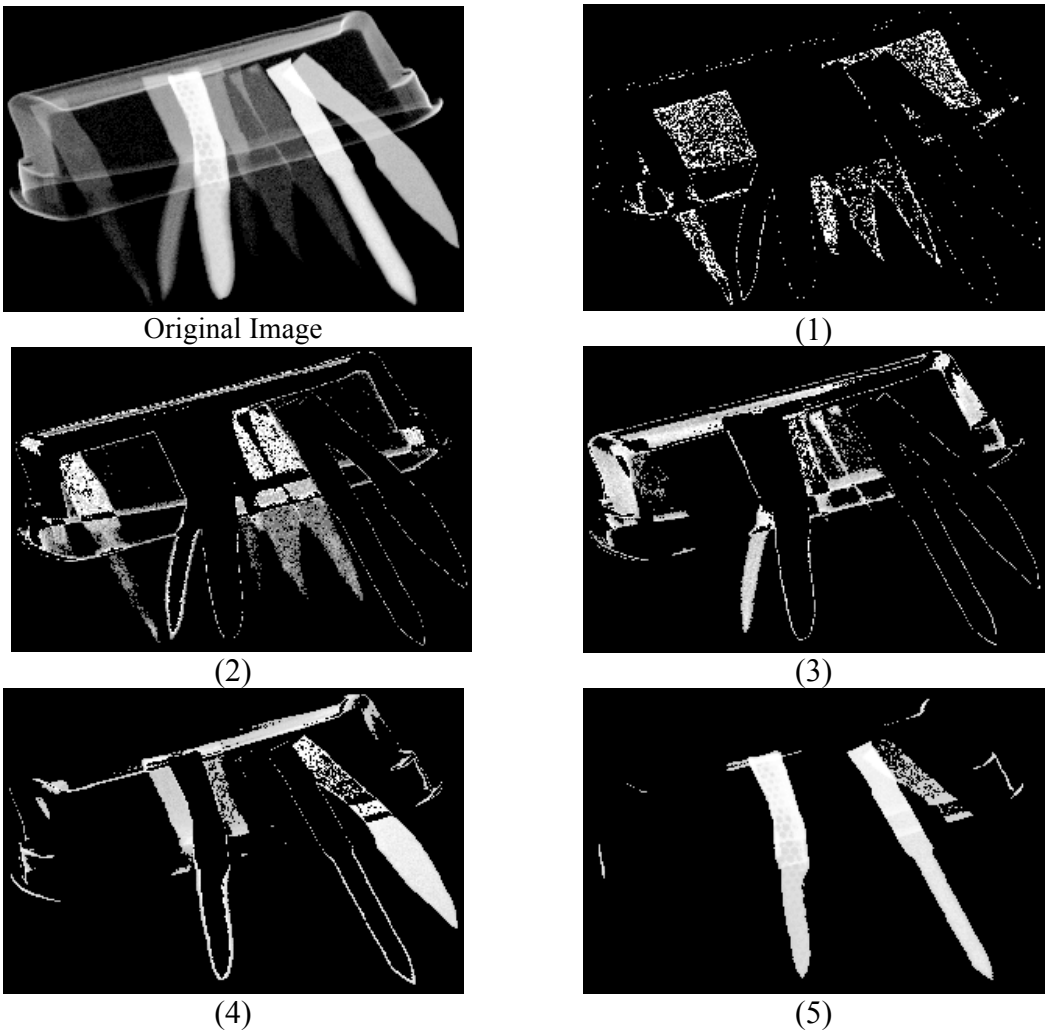

Figure 4.16 Resulting slices per class generated by using the thresholds shown in Table 4.4(c) for the case of 5 classes.

4.3.3 Integration of the Resulting Slices

Image slices corresponding to the classes, generated from the application of entropy-based multilevel thresholding methods such as ICM or Valley method, are combined in a single image, which is then color coded for better visualization.

Integration Method:
The HSI color model is used to compose the resulting slices into a single color image as following:

1 Assign one color to each class. For any two adjacent classes set complementary colors.
2 Apply contrast stretching to each of the resulting slices such that the content of each class is of the same color (hue) but encompass a wider range of intensities.

Color images, as shown in Figures 4.17, 4.18 and 4.19, are produced by using this integration method. Figures 4.17 (a) and (b) show the original image containing a low-density threat, a narrow soft wood knife, and its color counterpart composed using the 5 slices shown in Figure 4.8, respectively. Figures 4.18 (a) and (b) show the original image and its color counterpart composed using the 5 slices shown in Figure 4.9, respectively. The original image containing various low-density knives and its two color counterparts composed by using the 5 slices shown in Figure 4.10 and 7 slices are illustrated in Figures 4.19 (a), (b) and (c).

4.4 Summary

In this chapter, we showed through visual interpretation of segmented results, that common and newly developed image decluttering techniques are very valuable tools in revealing threats in single-energy x-ray luggage scans.

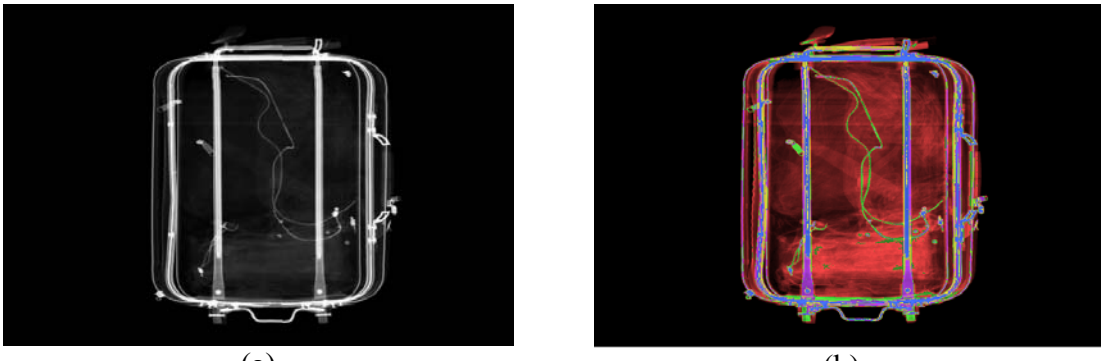

(a) (b)

Figure 4.17 (a) Original image containing a low-density threat, a narrow soft wood knife, (b) color counterpart composed by using the 5 slices shown in Figure 4.8 and applying a selected color map.

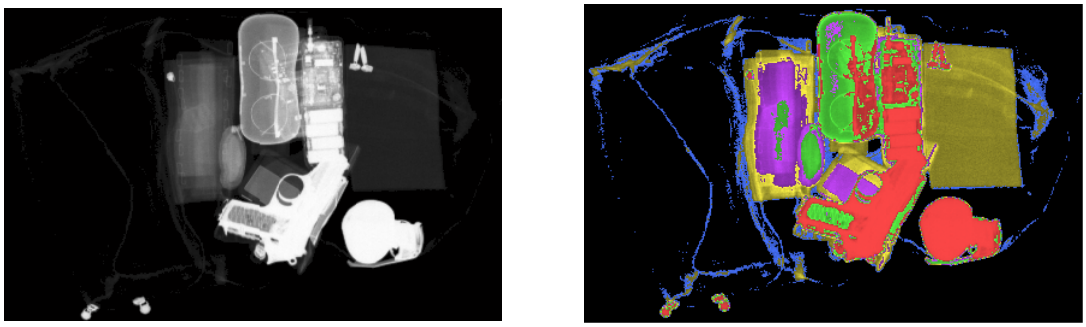

(a) (b)

Figure 4.18 (a) Original image containing high-density threats, gun and grenade, (b) color counterpart composed by using the 5 slices shown in Figure 4.9 and applying a selected color map.

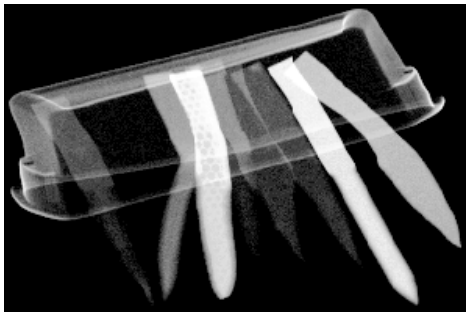

(a)

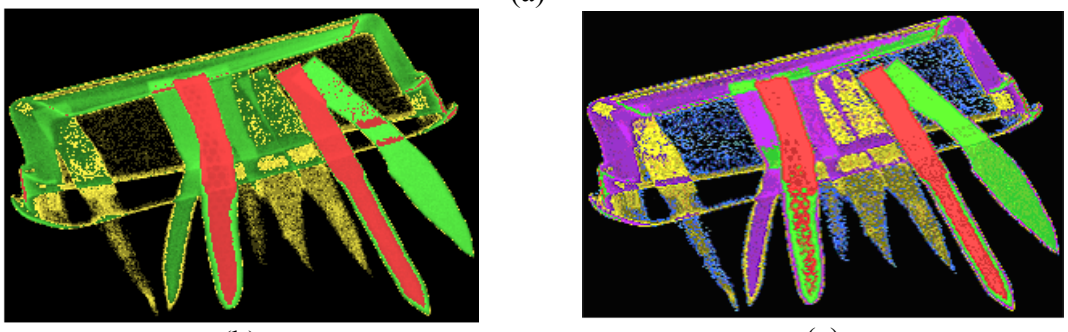

(b) (c)

Figure 4.19 (a) Original image containing various low-density knives, (b) color counterpart composed by using the 5 slices shown in Figure 4.10, (c) color counterpart composed by using 7 slices and applying a selected color map.

Several image hashing methods applied to single-energy x-ray luggage scans are first introduced. Entropy-based multilevel thresholding techniques are then presented. An existing time-saving multilevel thresholding method, ICM method, was chosen and applied to x-ray carry-on luggage scans. As the results show in the previous section, this method gives a satisfactory solution to our x-ray images in short time. An extension to the methods of [Luo and Tian, 2000] and [Chang et al., 2002], an entropy-based multilevel thresholding method, Valley method was proposed and tested by applying it to simulated images and real-world x-ray carry-on luggage images. The solution obtained by this method depends on the histogram shape of the input image. For images whose distribution of intensity values is not concentrated in a narrow graylevel range the proposed method is effective.

From the results obtained, it is clear that image segmentation is a useful preprocessing means to reveal various objects in carry-on luggage images. However, because of the uncertainty and diversity of contents in carry-on luggage, entropy-based multilevel thresholding methods, which provide solution independent of the shape of the image histogram, are desirable. Moreover, the automatic selection of the optimum number of classes in the image segmentation algorithms can be a potential extension to this effort.

5 Pseudo Coloring

The use of color in this study is motivated by the following reasons: (1) Color could improve the number of objects being distinguished as human beings can distinguish thousands of colors compared to a few dozen gray levels; and (2) Color adds vivacity to images, which in turn decreases boredom and improves the attention span of screeners.

This chapter describes a series of linear and non-linear pseudo-coloring maps designed and applied to single-energy x-ray luggage scans, in an effort to assist airport screeners in identifying and detecting threat items, particularly hard to see low-density weapons in luggage. Considerations of the psychological and physiological processing involved in the human perception of color as well as the effects of using various color models, such as the RGB and HSI models, are explored. Original gray scale data, various enhanced images, and segmented scenes are used as inputs to the various color mapping schemes designed in this research.

5.1 Aspects of Human Visual Perception

Color is a sensation created in the brain, caused when the light radiation of a certain wavelength reaches our eyes. It is a psychophysical phenomenon relating to both physiological (how the eyes detect light and color) and psychological (how the mind processes the sensation of color) processing. A brief background on each of these two aspects is given in Subsections 5.1.1 and 5.1.2. Recommendations for optimum color assignment are drawn in Subsection 5.1.3.

5.1.1 Physiological Processing of Color

The eye lens, retina, and color-processing unit along the optic nerve play the main role in the physiological processing of light. The function of the lens is to focus the incoming light on the retina. Different wavelength lights require different focal lengths. Therefore, for pure hues the lens must change its shape so that the light is focused correctly. If short wavelengths and long wavelengths, pure blue and pure red for instance, are intermixed the lens has to constantly change shape and the eye will become tired. A related effect called chromostereopsis is the appearance of pure colors located at the same distance from the eye to be at different distances, e.g. reds appear closer and blues more distant. Sometimes, pure blue focuses in front of the retina and appears unfocused. The lens also absorbs light about twice as much in the blue region as in the red region, meaning that people are more sensitive to longer wavelengths (yellows and oranges) than to shorter wavelengths (cyans and blues). The retina contains light sensitive cells (rods and cones), which absorb photons and transmit chemical signals to the brain. Cones are responsible for color vision and are divided into red, green and blue cones that are sensitive to long,

middle, and short wavelengths, respectively. Colors can be seen as variable combinations of red, green, and blue as all three types of cones are partially activated when light reaches the retina. The percentages of the number of the three types of cones present in the retina are as follows: blue at 4%, green at 32%, and red at 64%. All cones are differentially distributed in the retina with a dense cone concentration in the center of the retina. The distribution of the three types of cones themselves is also asymmetrical. The center of the retina is primarily made of green cones, surrounded by red cones, with the blue cones being mainly on the periphery. A minimum intensity level, function of the wavelength, is required for the photoreceptors to respond to a given color. The highest sensitivity, being in the center of the spectrum, requires blues and reds to have a higher intensity than greens or yellows to be equally perceived [Murch, 1984].

The optic nerve connects the retina to the brain and color-processing unit along the optic nerve transforms cone signals into the composite signals red + green, red - green, and blue - yellow ($yellow = (R + G)/2$) [Ouerhani et al., 2004], then transmits them to the brain using three corresponding channels called opponent processing channels.

5.1.2 Psychological Processing of Color

Psychological processing of color is a vast field of study and not as well understood as the physiological processing. In this field, simultaneous contrast, color-constancy and the effects of various backgrounds on color perception are the main aspects usually examined. Simultaneous contrast is the effect caused when the color of a patch is shifted perceptually by the color of adjacent patches [Ware, 1988]. For example, colors tend to look darker and corresponding objects look smaller against white, and lighter and larger against black as shown in Figure 5.1. Color surroundings cause chromatic induction (a color region appears tinged with the complementary hue of the surround) which can make the same colors look different or different colors look the same as shown in Figure 5.2. Many other factors such as field size and viewing conditions also affect the appearance of the color perceived.

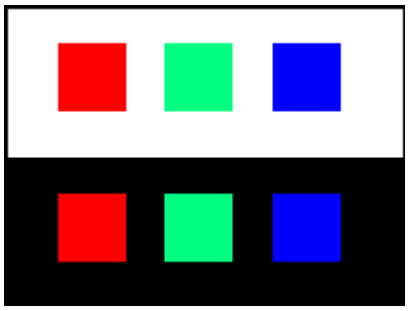

Figure 5.1 Simultaneous contrast: colors look darker and corresponding objects smaller against a white background and lighter and larger against a dark background [MacDonald, 1999].



(a) (b)

Figure 5.2 Simultaneous contrast can make (a) the same colors look different, or (b) different colors look the same [Taylor and Murch, 1986].

5.1.3 General Recommendations for Optimum Color Assignment

The effective use of color can be a very powerful tool, while the ineffective use of color can degrade an application's performance and lessen the user's satisfaction [Taylor and Murch, 1986; Wright, 1997]. In order to create an application where colors are used optimally, the following questions have to be answered [Healey, 1996]:

- How effectively can colors be selected to provide good differentiation between different objects?
- How many colors can be displayed at the same time?
- Which color space should be used?
- What factors determine target element color relative to non-target elements?

Color is usually used in a qualitative rather than a quantitative fashion, that is, to show that one item is different from another and not simply to display a relationship of degree. In general, for a set of colors to work well in a design, some unifying attribute should tie them together, following the Gestalt law of closure (completeness) [Moore and Fitz, 1993]. This could be a particular hue or range of saturations or lightness that appear throughout the composition to designate a given aspect or function, relieved by small areas of a contrasting accent color. Key issues to consider in finalizing a color scheme are clarity, comprehensibility, and how well the user will be able to pick out the desired information and understand its significance. Contributory factors include: (1) Discernibility — how easy it is to distinguish an item from its background; (2) Conspicuity — how obvious the item is relative to its neighbors; and (3) Salience — how well the item "pops out" from the display as a whole.

5.1.3.1 Physiologically-Based Guidelines

Based on the physiology of the human visual system as described in Subsection 5.1.1, the following guidelines for the use of color were drawn using Murch's principles [Murch, 1984]:

- The simultaneous display of extreme spectrum colors should be avoided. This causes the lens to rapidly change shape and thus tires the eyes. De-saturate the colors or use colors that are close together in the spectrum.
- Pure blue should be avoided for fine details such as text, thin lines, and small shapes. Since there are no blue cones in the center of the retina, fine details are difficult to see.
- Red and green should be avoided in the periphery of large displays.
- Adjacent colors that differ only in the amount of blue should be avoided. Since blue does not contribute to brightness, this creates fuzzy edges.
- Adjacent areas of strong blue and strong red should be avoided to prevent unwanted depth effects [MacDonald, 1999].
- Opponent colors go well together.
- Older operators need higher brightness levels to distinguish colors.
- The use of hue alone to encode information should be avoided in applications where serious consequences might ensue if a color-deficient user were to make an incorrect selection.

5.1.3.2 Psychologically-Based Guidelines

The following recommendations are based on the considerations given in Subsection 5.1.2:

- The number of colors used should be reasonable. If the user is overwhelmed or confused by too many colors vying for his/her attention, he/she is unlikely to develop an effective mental model [Wright, 1997].
- Consistency is vital when meanings are assigned to colors. The intuitive ordering of colors helps establish intuitive consistency in a design. The spectral and perceptual order of red, green, yellow, and blue can guide the order of the concepts attached to color. For instance, red is first in the spectral order and focuses in the foreground, green and yellow focus in the middle, while blue focuses in the background.
- If the color of a kind of items is known ahead of time or if a color only applies to a particular type of items, the search time for finding an item decreases.
- Where accurate visual judgment of a color is necessary, the surrounding should be a neutral mid-gray to avoid unwanted perceptual color changes.
- Color can be described more meaningfully in terms of the perceptual dimensions of lightness, hue, and colorfulness than in terms of the measured dimensions.

5.2 Theoretical Aspects of Pseudo-Coloring

The two main aspects that influence the appearance of pseudo colored objects are the color space used and the color transform applied within that space. The following is an analysis on how each of these can affect the perceived colored scene.

5.2.1 Color Spaces

A color space (or model) is a specification of a coordinate system and a subspace within that system where each color is represented by a single point [Gonzalez and Woods,

2002]. Color spaces provide a rational method to specify, order, manipulate, and effectively display an object's colors. Color spaces may be used to define colors, discriminate between colors, judge similarity between colors, or identify color categories for a number of applications [Plataniotis et al., 2000]. The process of selecting the proper color space involves knowing how the color signals are generated and what information is needed from these signals.

RGB and HSI are two widely used color spaces referred to in the design of the color transforms introduced and discussed in this chapter.

5.2.1.1 The RGB Color Model

The RGB color model is normally used on monitors, namely for display. In this model each color is expressed using its primary spectral components of red, green, and blue. This color model is device-dependent and easy to implement, but is non intuitive for interpretation.

5.2.1.2 The HSI Color Model

The HSI model is defined based on how humans describe color. It is a user-oriented model that is suited for human interpretation. Each color in the HSI model is represented by a hue, saturation, and intensity component.

Hue is a color attribute that describes true color. It refers to the degree of red, green, blue, yellow, purple, etc., in a given color. Another way to think of hue is as a description of a particular wavelength in the spectrum. A coding scheme for hue might follow the spectrum, starting with red at 0, green at 0.33, blue at 0.66, and wrapping around back to red at 1.0. Saturation is the purity of the color, or the measure of the degree to which a pure color is diluted by a white light [Thompson, 1995]. Saturated colors have comparatively higher degrees of hue whereas de-saturated colors are comparatively closer to gray. One important property of saturation is that if the saturation of all the pixel values is set to 0, all the colors are washed out of the image and the only component of the HSI specification that is visible is the value component. In other words, you can change an image to display only gray values by setting the saturation for all pixels to 0, and you can tint all the pixels by setting saturation to some larger value. Intensity of the color represents how little black has been added to the color. A low value means the color is approaching black; a high value means little black has been added and the hue shines through clearly. The intensity component is decoupled from the color information in the image and the hue and saturation components are intimately related to how humans perceive color. These features make the HSI model suitable for developing image processing algorithms for human interpretation.

5.2.2 Color Transforms

The main objective of pseudo coloring is to obtain an ergonomic color representation of the data that can be easily recognized by a human with normal sight. A variety of

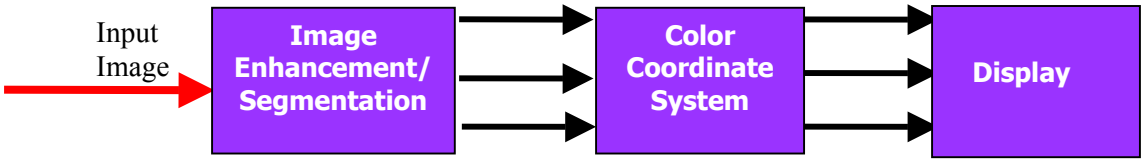

Figure 5.3 General approach for color mapping of gray level images.

mapping schemes can be used to achieve this task. Pseudo colored images are all obtained using the basic technical approach shown in Figure 5.3. Pseudo-color mappings are non-unique and extensively interactive trials have to be performed to determine an optimum mapping for displaying a given set of data.

One of the basic techniques for pseudo coloring is performed by directly applying a single color hue to replace a particular gray scale. For example, the color range from C_{0-255} can be used to code the gray scale range I_{0-255}. Another approach [Dai and Zhou, 1996] is based on the desired tri-stimulus value of the output color image, where analysis of the tri-stimulus value of the required output image is performed and a function $P[]$ is defined, which maps the original gray scale data $I(x, y)$ to the primary color values $R(x, y), G(x, y), and\ B(x, y)$. This process can be represented as follows:

$$\begin{aligned} R(x,y) &= P_R[I(x,y)] \\ G(x,y) &= P_G[I(x,y)] \\ B(x,y) &= P_B[I(x,y)] \end{aligned} \quad , \tag{5.1}$$

where the transforms $P_R[], P_G[], P_B[]$ could be either linear or non-linear functions, based on the desired output image. The complete color-coding process can be described as follows:

$$I(x,y) \Rightarrow \begin{Bmatrix} P_R[] \\ P_G[] \\ P_B[] \end{Bmatrix} \Rightarrow \begin{matrix} R(x,y) \\ G(x,y) \\ B(x,y) \end{matrix} \Rightarrow C(x,y). \tag{5.2}$$

$C(x, y)$ is the final pseudo colored image. By varying the functions $P[]$, different color coded images can be obtained.

To accurately represent gray values using color, the following properties are desirable in a color scale [Levkowitz and Herman, 1992; Levkowitz, 1988]. Given a sequence of numerical gray values $\{v_1 \le ... \le v_N\}$ represented by the colors $\{c_1 \le ... \le c_N\}$, respectively: (1) Color should perceivably preserve the order of gray values, i. e., the relationship among the colors should be c_1 perceived as preceding $... c_i$ perceived as preceding c_N; (2)

Color should perceivably reflect the distances between the gray values, that is, for any $1 \le i, j, m, n \le N$, *if* $v_i - v_j = v_m - v_n$, we should also have $pd(c_i, c_j) = pd(c_m, c_n)$, where $pd(c_i, c_j)$ is the perceived distance between c_i and c_j; (3) Boundaries not existing in gray-level data should not be perceived after using color.

The combination of the concepts of increasing the number of JNDs [Levkowitz and Herman, 1992] and conveying both value and form information effectively, by reducing the effects of simultaneous contrast, would result in a color scale sequence that increases monotonically in luminance, while cycling through a range of hues [Ware, 1988]. Combining these two major ideas with the general recommendations for optimum color assignment given in Subsection 5.1.3, the following rules [Ware, 1988] are used to produce a number of optimal transforms:

- For transforms designed based on the RGB color model, the R, G and B versus gray level transform functions should not decrease simultaneously and the intensity, $I = (R + G + B)/3$, should increase monotonically. For $1 \le n \le N-1$ and $r_n \le r_{n+1}$, $g_n \le g_{n+1}$, and $b_n \le b_{n+1}$, we should have $r_n + g_n + b_n \le r_{n+1} + g_{n+1} + b_{n+1}$. Colors should be triple mixtures (RGB), and not pair-wise mixtures, to avoid exaggerated saturation.

- For transforms designed based on the HSI color model, good properties for revealing both shape and value are that the intensity I versus gray level should increase monotonically; the hue H versus gray level should cycle through a particular range of hues such that for $1 \le m \le N$, $h_1 \le ... \le h_m \prec h_{m+1} + 360... \le h_N + 360$ or $h_1 \ge ... \ge h_m \succ h_{m+1} - 360... \ge h_N - 360$, and the saturation S versus gray level should be monotonic, i.e., $s_1 \le s_2 \le s_3 \le ... \le s_{N-1} \le s_N$ or $s_2 \ge s_3 \le ... \ge s_{N-1} \ge s_N$ [Levkowitz and Herman, 1992]. The hues should be chosen in such a way that the color scale runs from inherently dark hues to inherently light hues.

Based on the characteristics of major color spaces and recommendations for color transforms, a number of color maps were designed, implemented, and applied to x-ray luggage scans. The following sections describe the implementation, results, and comparative performance of these color mapping approaches. Two classes of color maps were identified one in the RGB space and the other in the HSI space. Within each class, user-specified, mathematically formulated, or constraint-driven transforms are implemented and tested.

The color transforms were applied to x-ray luggage scans containing various potential threat objects made of low-density materials. Three x-ray luggage scans with three different knives are shown in Figures 5.4 (a), (b) and (c) in order of increasing density. The three knives are made of soft wood, light-purple glass, and aluminum.



(a) (b) (c)

Figure 5.4 Original x-ray luggage scans containing knives made of (a) soft wood, (b) light-purple glass, and (c) aluminum.

5.3 RGB-Based Color Transforms

RGB-based color transforms were further classified into two subcategories, user-selected color mappings and mathematically formulated approaches. Linear and non-linear maps were implemented and evaluated.

5.3.1 Perceptually-Based Color Mapping

In these mappings, the color series are usually set up visually according to the color preferences of the user and the transforms defined accordingly.

5.3.1.1 Linear Mapping

For initial trials, a few color maps were adopted from the Matlab image processing toolbox. Those maps were also used in our final performance evaluation for comparison purposes with the transforms that we designed. The "Hot" and "Jet" color scales were first applied to x-ray luggage scans. As Figures 5.5 (a) and (b) show, the "Hot" map changes smoothly from black, through shades of red, orange and yellow, to white, and "Jet" map ranges from blue to red passing through cyan, yellow and orange. The two color scales can be produced using Equations (5.3) and (5.4), respectively.

$$R = \begin{cases} \dfrac{I+1}{n} & I \le n-1 \\ 1 & I > n-1 \end{cases}, \; G = \begin{cases} 0 & I \le n-1 \\ \dfrac{I+1-n}{n} & n-1 < I \le 2n-1, , \\ 1 & I > 2n-1 \end{cases} \tag{5.3}$$



(a) (b)

Figure 5.5 (a) The "Hot" color scale and (b) the "Jet" color scale.

$$B = \begin{cases} 0 & I \le 2n-1 \\ \dfrac{I+1-2n}{m-2n} & I > 2n-1 \end{cases} \tag{5.3}$$

where I represents the gray value, m is the number of colors of the "Hot" scale and $n = f_1(\frac{3}{8}m)$ in which $f_1(x)$ rounds x to the nearest integer towards zero. In Equation (5.4) I represents the gray value, $n = f_2(\frac{m}{4})$ and $\Delta = f_2(\frac{n}{2}) - (\text{mod}(m,4) == 1)$ in which m is the number of colors of the "Jet" scale and $f_2(x)$ rounds x to the nearest integer larger than x.

$$G = \begin{cases} 0 & I \le \Delta - 1 \\ \dfrac{I+1-\Delta}{n} & \Delta - 1 < I \le \Delta + n - 1 \\ 1 & \Delta + n - 1 < I \le \Delta + 2n - 2 \\ \dfrac{\Delta + 3n - I - 1}{n} & \Delta + 2n - 2 < I \le \Delta + 3n - 2 \\ 0 & I > \Delta + 3n - 2 \end{cases} \tag{5.4}$$

The Red and Blue component values can be obtained by shifting the Green component G to the right and left by $\dfrac{n}{\max(\ grayvalue\ )}$, respectively. Figures 5.6 (a) and (b) illustrate the R, G, and B transforms of the "Hot" and "Jet" color scales.

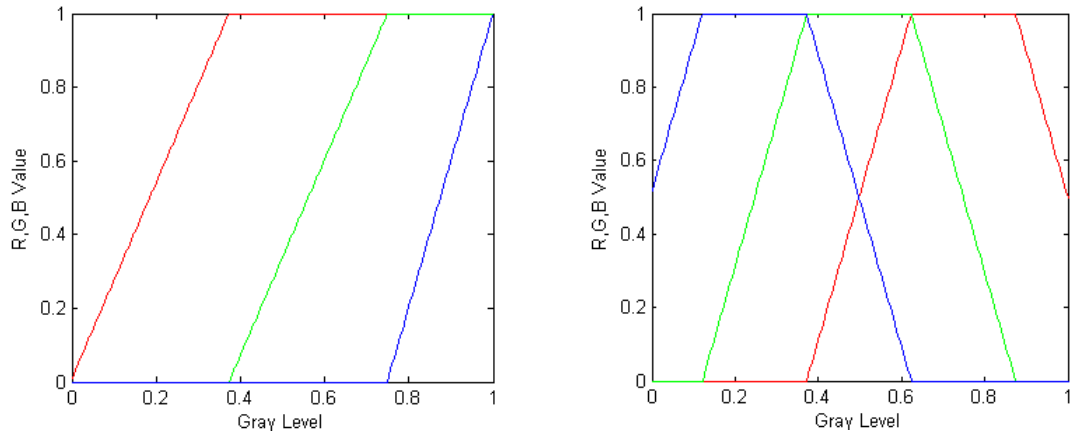

(a) (b)

Figure 5.6 (a) R, G and B values versus gray level for the "Hot" scale, (b) R, G and B values versus gray level for the "Jet" scale.

Colored versions, shown in Figures 5.8 and 5.9, of Figure 5.4 were generated by applying the "Hot" and "Jet" scales to the enhanced images in Figure 5.7 produced by using *original* + *negative* + *h-domes* + *contrast stretching* [Abidi et al., 2004].

5.3.1.2 Non-linear Mapping

This scale, referred to as the "Warm" color scale, varies from dark blue, through magenta and orange, to light yellow. The distances between adjacent colors on this scale are perceivably equal. A 256-step scale as seen in Figure 5.11 (b) was developed and applied to x-ray luggage scans as an extended version to the 16-step color scale shown in Figure 5.10 [Shi et al., 2002]. The colors on the 16-step scale were utilized as base colors and intermediate colors computed by linearly interpolating the red, green, and blue intensity values from each base color to the next. Let R_i, G_i, B_i and $R_{i+1}, G_{i+1}, B_{i+1}$ represent any two adjacent base colors; I_i and I_{i+1} denote their corresponding gray levels. Thus, given a gray level I ($I_i < I < I_{i+1}$ for $1 \le i \le 15$), the associated intermediate color $C = (R, G, B)$ between base colors C_i and C_{i+1} can be found by applying Equation (5.5). Figure 5.11 (a) illustrates the R, G and B values versus gray levels obtained by linearly fitting 256 colors to the 16-step data. Figure 5.12 was obtained by applying the designed color scale "Warm" to the same preprocessed images of Figure 5.7.

$$\begin{aligned} R &= (R_{i+1} - R_i)\left(\frac{I - I_i}{I_{i+1} - I_i}\right) + R_i \\ G &= (G_{i+1} - G_i)\left(\frac{I - I_i}{I_{i+1} - I_i}\right) + G_i \\ B &= (B_{i+1} - B_i)\left(\frac{I - I_i}{I_{i+1} - I_i}\right) + B_i, \end{aligned} \tag{5.5}$$



(a) (b) (c)

Figure 5.7 Enhanced version of Figure 5.4 produced by using original + negative + h-dome + contrast stretching.

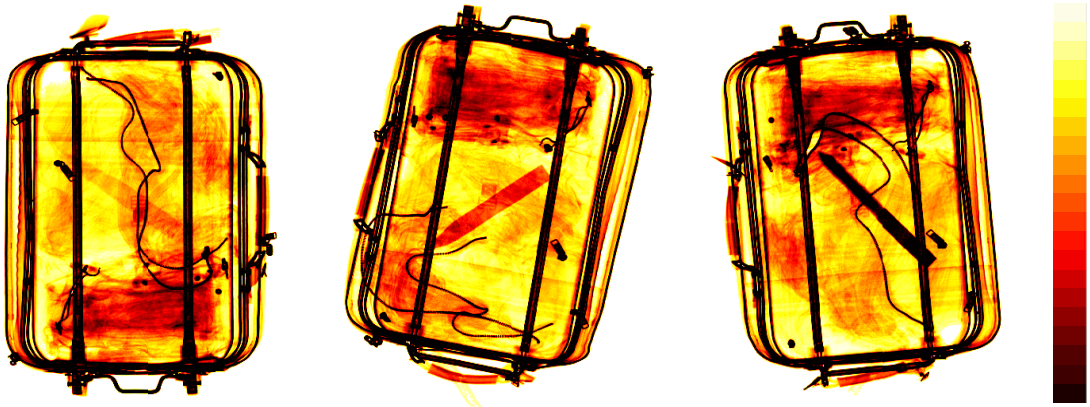

(a) (b) (c)

Figure 5.8 Colored version of Figure 5.7 generated by applying color scale "Hot".

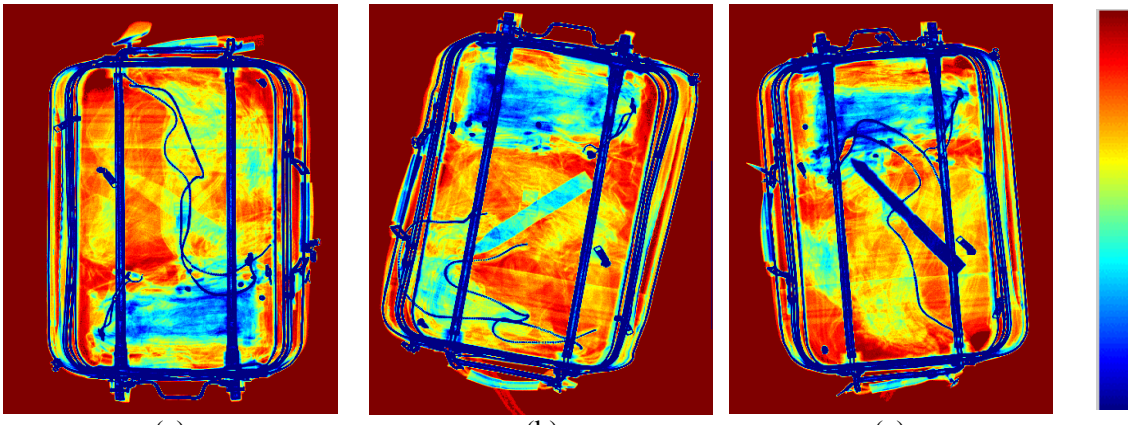

(a) (b) (c)

Figure 5.9 Colored version of Figure 5.7 generated by applying color scale "Jet".



Figure 5.10 The 16-step "Warm" color scale.

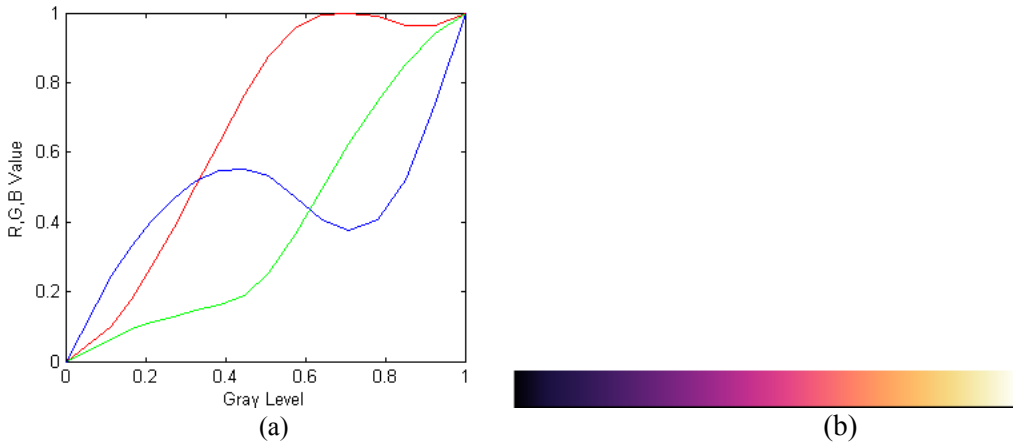

(a) (b)

Figure 5.11 (a) R, G and B values versus gray level obtained by linearly fitting 256 steps to the16-step scale, (b) the 256-step "Warm" color scale.



(a) (b) (c)

Figure 5.12 Colored version of Figure 5.7 generated by applying the designed color scale "Warm" shown in Figure 5.11(b).

5.3.2 Mathematical Formulations

The mapping between colors and gray values in this case is obtained through the use of a mathematically formulated transform. The nature of the mathematical formula determines the color content of the output image. In this section, I denotes the value of a pixel before transform; $R, G, and\ B$ denote its color output in each of the channels. Various types of transforms can be used for color mapping. The following are some of the transforms we designed and applied to x-ray luggage data.

5.3.2.1 Algebraic Transforms

In this mode, color is assigned through a mathematical algebraic formula applied to individual or group pixel values to create various combinations of these original pixels and obtain their resulting color counterparts. An example formula for such a function is given by Equation (5.6), where the number of colors is a parameter (L) that can be supplied by the user and is intrinsically incorporated into the formula for color generation. N is an integer varying from 1 to L. The gray scale was divided into L equal intervals corresponding to the L colors; therefore, for all I s belonging to the same interval, one single color is assigned.

$$\begin{aligned} R &= N / L \\ G &= 1 - N / L \\ B &= \left|2N / L - 1\right| \end{aligned} \quad . \tag{5.6}$$

In this mode, the number of basic colors actually remains the same but variations occur in the color range. For example, when $L = 4$, a color image with only the "basic" colors is produced. The information in this color image is minimal because only the higher pixel values from the gray-scale image are clearly coded. However, when $L = 16$ an image with the same basic colors is produced but the individual range for each color is expanded to obtain 16 colors overall. Most of the information is now retrieved with even the lower pixel values in the gray-scale image being coded. Figure 5.13 illustrates the use of this method to color code a gray-scale image and shows how the variation of the number of colors can achieve different effects in the colored image, such as a variable amount of detail and clutter.

5.3.2.2 Trigonometric Transforms

a) Sine/Cosine transform

One of the characteristics of the sine function is that it contains regions of relatively constant value around the peaks as well as regions that change rapidly near the valleys. The advantage of a continuous color scale becomes evident when considering overlapping materials inside luggage. In systems with abrupt color switch-over between, for example, organic and non-organic materials, even thin layers of overlapping materials, such as steel, copper or PVC, will lead to organic materials being classified as non-organic materials, which is incorrect and might result in false negatives and/or false

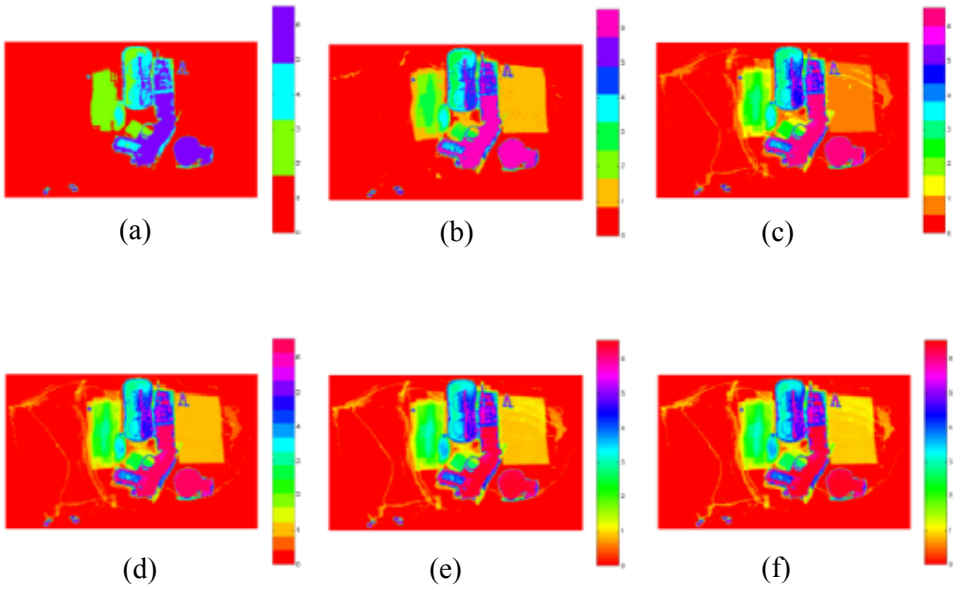

Figure 5.13 Varying the number of colors using the mathematical expression of equation (5.6) for color mapping; (a) through (f) represent color maps using 4, 8, 12, 16, 64, and 256 colors respectively.

positives. The typical form of the sine transform can be expressed as [Gonzalez and Woods, 2002]:

$$\begin{aligned} R &= \left|\sin(\omega_R I + \theta_R)\right| \\ G &= \left|\sin(\omega_G I + \theta_G)\right|, \\ B &= \left|\sin(\omega_B I + \theta_B)\right| \end{aligned} \tag{5.7}$$

where $\omega_R, \omega_G, \omega_B$ are the frequencies for the R, G, and B channels and $\theta_R, \theta_G, \theta_B$ their corresponding phase angles. Changing the frequency and phase of each sine function can emphasize (in color) certain ranges of the gray scale. The effect of mathematical manipulation of the sine-based color assignment on viewer perception of objects and presence of details in x-ray data can be seen in Figure 5.14.

b) Rainbow transform

The rainbow transform can be seen as a special case of the sine/cosine transform. The general form of the three-transform functions used for the rainbow map, are given by Equation (5.8). Specifically speaking, the three periodic functions were used in such a way that one of them was at a peak in a selected color interval as shown in Figure 5.15.

$$\begin{aligned} R &= (1+\cos(\tfrac{4\pi}{3*255} I)/2 \\ G &= (1+\cos(\tfrac{4\pi}{3*255} I - \tfrac{2\pi}{3})/2 \\ B &= (1+\cos(\tfrac{4\pi}{3*255} I - \tfrac{4\pi}{3})/2 \end{aligned} \tag{5.8}$$

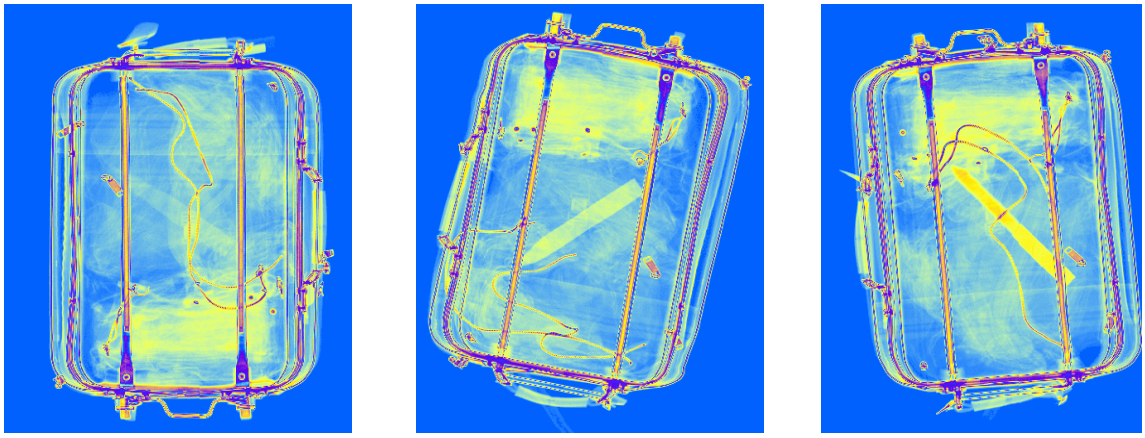

(a) (b) (c)

Figure 5.14 Colored version of Figure 5.4 generated using the sine transform.

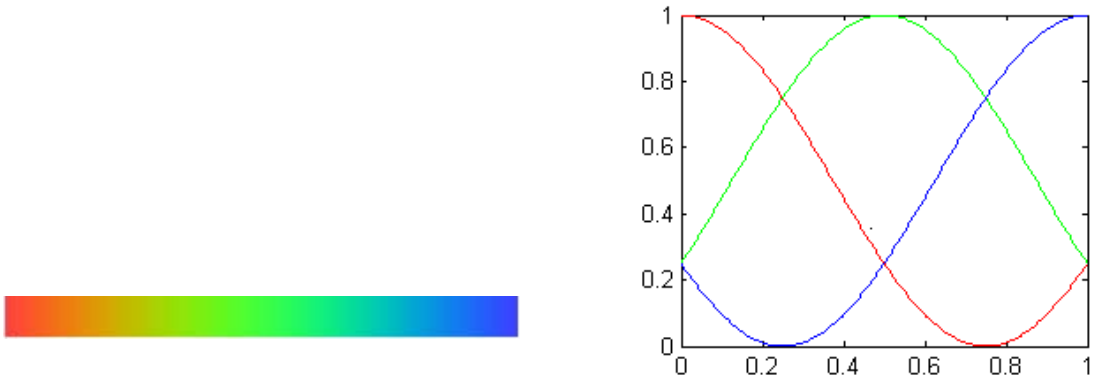

(a) (b)

Figure 5.15 (a) The rainbow color scale; (b) the three periodic functions used for the rainbow transformation. Red, green and blue curves represent the R, G, and B vs. gray level transform functions, respectively.

5.4 HSI Based Color Transforms

HSI-based color transforms were also classified into two subcategories. Color transforms in the first subcategory provide a direct mapping between the gray values and their color counterparts while color transforms in the second subcategory were created according to the approach illustrated in Figure 5.16, where a selected series of enhancement operations are first performed on the x-ray luggage scan to extract or emphasize features of interest and then the results are fed into the H, S and I components to create a composite chromatic image.

5.4.1 Color Directly Applied to Original Gray Scale Data

Two methods are investigated in this subcategory: (1) a histogram-based approach, resulting into a visually selected scale, and (2) a non-linear approach based on the considerations of Subsection 5.2.2.

5.4.1.1 Histogram-Based Color-Mapping

The colors of the various components in the scene are assigned based on the values of the raw image. Pixel ranges are selected from the data's histogram and automatically assigned certain colors. For instance, it is known that high-density (metallic) material has a low degree of transparency and consequently higher pixel intensities. Color components for such gray levels can then be set to result in certain values. Based on the results derived from the color study discussed earlier, this basic procedure can be conducted as follows: (1) Set threshold values, (2) Define the number of colors to be used, (3) Define the hues to be used for each interval of pixel values, (4) Set the saturation to one and the intensity to the gray value of the pixel, then (5) Transform the HSI image to RGB space for display. If for example, four gray level regions were created, the chances of the low-

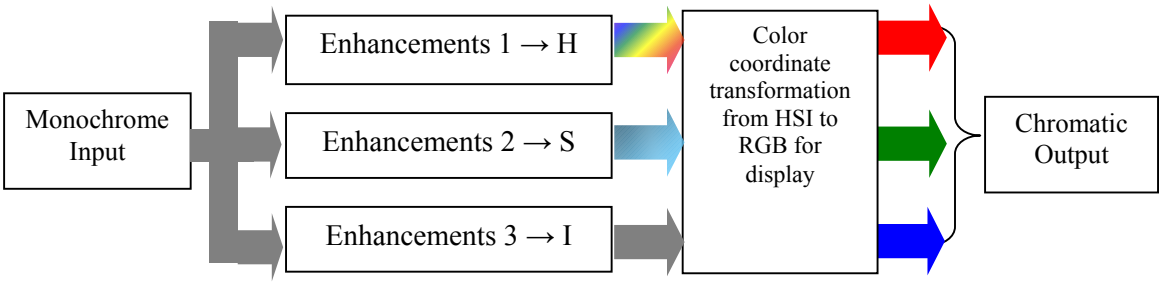

Figure 5.16 General process producing the second-subcategory of HSI-based color transforms.

density threat being present would be greatest in the first two regions. Four colors will be picked based on the recommendations of Subsection 5.1.3. Blue will be used as background and other easy to remember basic colors like red and green will be applied to the other pixels in each bin. The output image would have four hues, which vary as a function of the gray intensity values of the pixels.

5.4.1.2 Function-Based Color Mapping

Based on the criteria mentioned in Subsection 5.2.2, the focus was on the design of natural-order color scales with the ability to reveal value and shape information accurately and effectively by decreasing the effects of simultaneous contrast. In luggage inspection applications, as in many others, the most important issue is that the colors on a color scale used to represent gray values should be perceived as preserving the order of the gray values whenever colors are individually viewed or colors located on different color grounds are viewed. Specifically, the intensity was selected to be monotonically increasing, which could be described by a logarithmic transform, an exponential, a linearly increasing, or any other non-decreasing transform. The optimum selection of the appropriate transform depends on the specific application, i.e., emphasis needs to be made on the low-intensity or high-intensity part of the image. A key issue in the implementation is the design of the hue transform. A right/left semi-ellipse curve is selected for the hue transform and the saturation set to a constant. Considering the fact that the objective is to better visualize low density threat items, the logarithm transform for intensity is used as a way of increasing the value of the low gray levels, improving their appearance, and potentially recognition by screeners. Figure 5.17 (a) shows the transformations of intensity, hue, and saturation and Figures 5.17 (b) and (c) the resulting color bars when using the right and left semi-ellipses respectively. The color scale of Figure 5.17 (b), called "Springtime", uses $h_s = 0, 0 \le h_e \le 180$ and $dir = up$, where h_s is the starting hue, h_e is the ending hue, and up means a counterclockwise progression. The H, S, and I components are given by Equation (5.9).

$$H = \frac{1}{2} - \frac{1}{2} * sqrt\left(1 - \left(\frac{G}{G_{\max}}\right)^2\right);\ S = 0.8;\ I = \ln\left(\frac{G+1}{G_{\max}+1}\right), \tag{5.9}$$

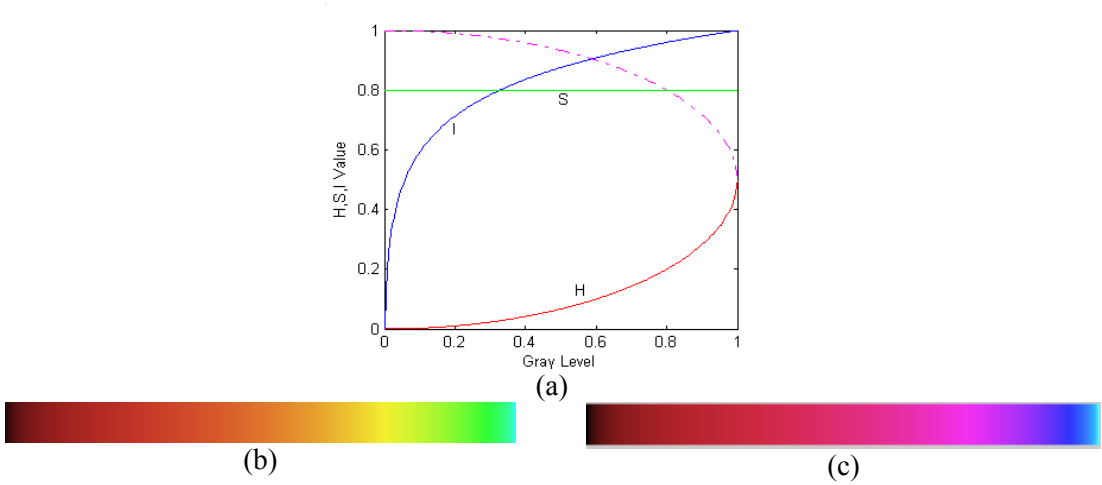

Figure 5.17 (a) Intensity, hue and saturation transforms, (b) color scale "Springtime" produced by using the concave part (solid curve) of the semi-ellipse for the hue transform, and (c) color scale produced by using the convex part (dotted curve) of the semi-ellipse for the hue transform.

where G is the gray level value and $G_{\max}$ is the maximum gray value over the entire image (255 for 8-bit images).

Applying the non-linear "Springtime" color scale to the images in Figure 5.7, we obtain the colored version shown in Figure 5.18.

5.4.2 Color Mapped to Preprocessed Gray Scale Data

Based on the theoretical background addressed in Subsection 5.2.2 and the recommendations of Subsection 5.1.3, different color schemes were designed where preprocessed gray scale data is used as input to the hue, saturation, and intensity color channels. The first set of transforms uses a constant saturation while the second set uses a data dependent saturation.

Let E_1, E_2, and E_3 be the enhanced images produced using some desired gray scale enhancement operations.

5.4.2.1 Constant Saturation

In this first approach, two subsets of color mapping are produced by feeding E_1 (or E_2) into the hue component and E_3 (or E_1) into the intensity component. The saturation, S, is set to a constant within the interval $[0.6, 1]$, that is high enough to ease the distinction between colors but low enough to avoid eye-fatigue due to refocusing [Murch, 1984].

Using this scheme, zero value pixels in E_3 (or E_1) would not appear in the colored image, which generally helps improve the appearance of the final output. The sequences CS1

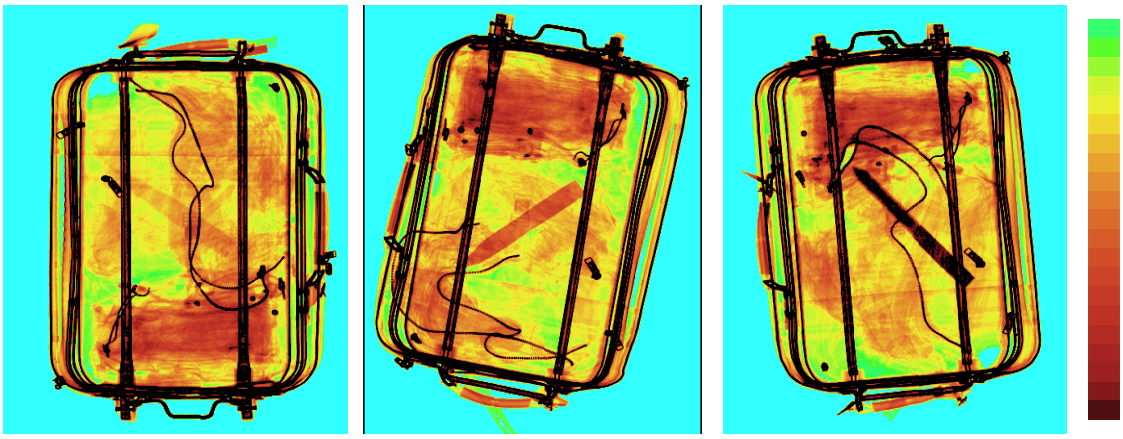

(a) (b) (c)

Figure 5.18 Colored version of Figure 5.7 generated by applying the "Springtime" color scale.

and CS2, described below, are two sets of transformations using gray level enhancement operations found, through screeners tests, to be effective in revealing low-density threats in x-ray luggage scans [Abidi et al., 2004]. The notation "$Original + A + B + C + ...$" denotes a sequence of preprocessing using operations A, B, C, ... applied to the original x-ray luggage scan. The two sets are designed as follows: (1) CS1 with H = E_1 = original + histogram equalization + contrast stretching, S = constant, and I = E_3 = original + negative + H-domes + contrast stretching; and (2) CS2 with H = E_2 = original + negative, S = constant, and I = E_1 = original + histogram equalization + contrast stretching. The colored versions of Figure 5.4 shown in Figures 5.19 and 5.20 were produced using color schemes CS1 and CS2.

Another approach uses the segmented image of the original luggage scan as an input to the pseudo-coloring process. N classes in the scene are clustered through segmentation and a single hue is assigned for each class. For any two adjacent classes complementary colors are used. Contrast stretching is applied to each class such that the intensities of objects in each class cover the full range of gray scale. Objects belonging to a given class will have the same hue value but different intensities. This transform is similar to the histogram-based color map described in Subsection 5.4.1 except that the thresholds in this case are selected automatically via the segmentation algorithm. For each class, the transforms for the H, S, and I channels are expressed as: *H = constant, S = constant, and I = image slice containing one class of objects + contrast stretching*. A single chromatic image containing the N classes of objects is obtained by replacing the image slice in the intensity transform by the segmented image and assigning the hue values accordingly. A multi-level thresholding (Maximum Entropy Approach Using Iterated Conditional Modes -ICM- [Besag, 1986]) was performed to segment various objects in the scene into 5 classes. The red color was assigned to the class of threat objects. The result of a selected color assignment is shown in Figures 5.21.

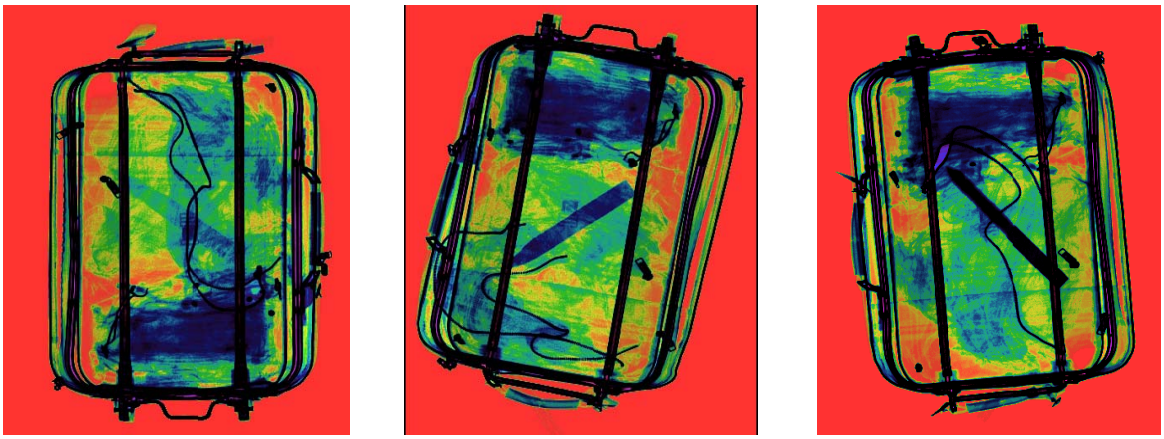

(a) (b) (c)

Figure 5.19 Colored version of Figure 5.4 generated by using color map *CS1* with constant saturation.

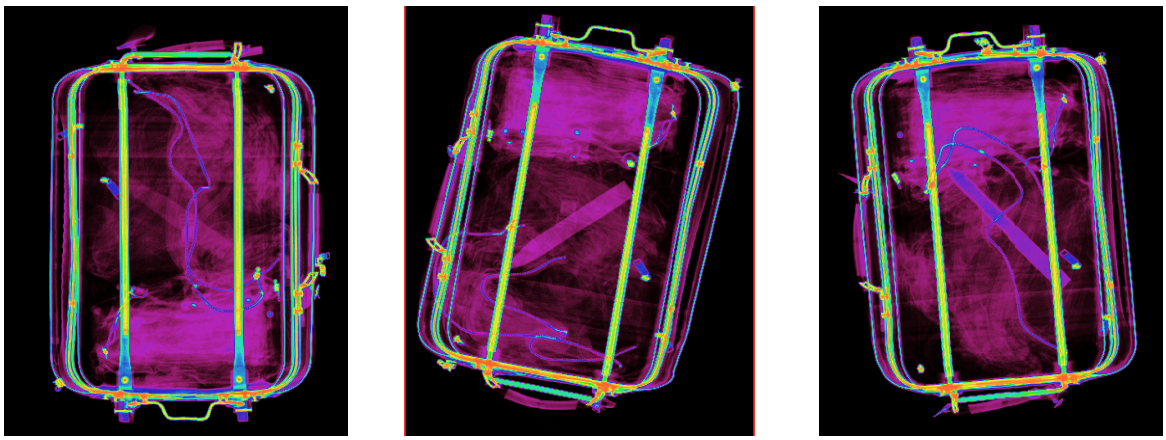

(a) (b) (c)

Figure 5.20 Colored version of Figure 5.4 generated by using color map *CS2* with constant saturation.

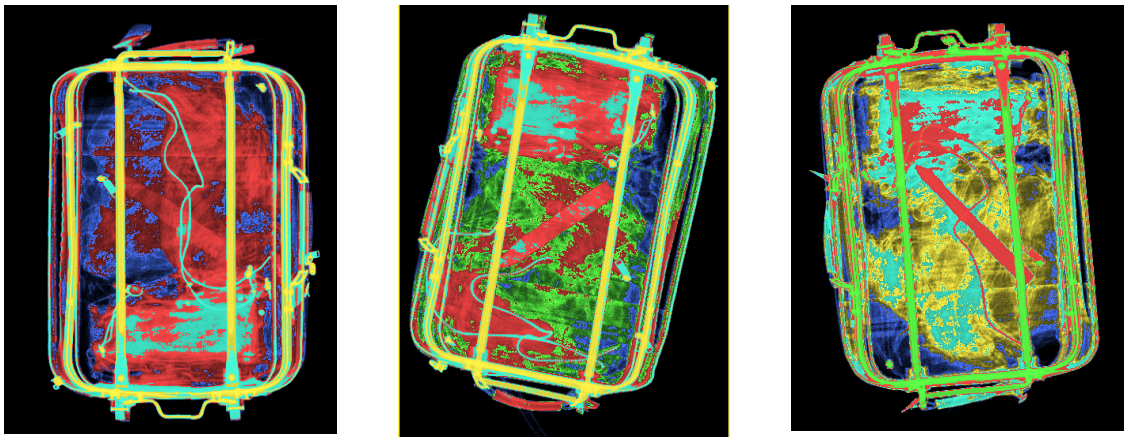

(a) (b) (c)

Figure 5.21 Color-coded version of Figure 5.4 obtained after segmentation, using a constant saturation and 5 different hues (complementary colors), (a) and (b) blue, green, red, cyan and yellow, (c) blue, yellow, cyan, red and green.

5.4.2.2 Variable Saturation

In this scheme E_1 is fed into both the hue and saturation components, while E_3 is fed into the intensity component. Thus, E_1 determines whether some areas of the output image are shown in color or in black and white. If the pixel values of an area in E_1 are all zero, the area will appear black in the output image. Therefore colors are only assigned to the areas where pixel values of both E_1 and E_3 are non-zero, that is, the areas of $E_1 \bigcap E_3 \neq 0$. Instead of using a constant for the S component as in sets CS1 and CS2 in Subsection 5.4.2, the same transformed data used for the H component is fed into the saturation channel. The two sets obtained are therefore: (1) VS1 with $H = E_1 =$ *original + histogram equalization + contrast stretching*, $S = E_1 =$*original + histogram equalization + contrast stretching*, and $I = E_3 =$ *original + negative + H-domes + contrast stretching*; and (2) VS2 with $H = E_2 =$ *original + negative*, $S = E_2 =$*original + negative*, and $I = E_1 =$ original + *histogram equalization + contrast stretching*. Figures 5.22 and 5.23 illustrate the results obtained from applying sets VS1 and VS2, respectively to the images in Figure 5.4.

5.5 Formal Airport Evaluation

Given the fact that airport screeners are the end users of any selected luggage coloring scheme, a natural step of this process is to include, in the validation of the various color coding approaches, the responses of a representative section of the screeners' population. A fully automatic, portable, and interactive computer test was designed. A set of 45 x-ray scans containing various low density threat items in different configurations and with various levels of clutter were selected. Eight pseudo-coloring approaches as described in Sections 5.3 and 5.4 were chosen according to preliminary evaluations of the various



(a) (b) (c)

Figure 5.22 Colored version of Figure 5.4 generated by using color map *VS1* with variable saturation.



(a) (b) (c)

Figure 5.23 Colored version of Figure 5.4 generated by using color map *VS2* with variable saturation.

transforms. The selected color maps were each applied to the luggage scans containing low-density threats. All images were shown to screeners in random order using a random number generator, with all originals shown first and also in random order. The random display of all original data first insures that no systematic influence or bias is gained in the detection of threat by viewing the color enhanced images before the non-colored images. The screeners were asked not only to affirm seeing a threat but to also point and click on the threat to ensure they saw the actual threat. The screeners were also asked to rank the images in terms of their visual clarity and ease of interpretation, which is an important fact in relieving boredom and keeping the screener's level of concentration relatively high. The evaluation sessions were conducted at McGhee Tyson Airport in Knoxville, Tennessee and involved a total of 40 Transportation Security Administration (TSA) luggage screeners. Three types of information were collected for each image shown: (1) did the screener see the threat object in the image, (2) could the screener click on the location of the threat item correctly, (3) a rating (from 1 to 10, with 10 being best) of "how helpful" the screener believed the displayed image was in detecting the threat object. After all color coded images have been shown as single windows, a montage image is shown for each original.

In this montage, the original image is shown side by side (for comparison purposes) with each of its colored versions and the screener is asked to rate each of the nine images on a 1 to 10 scale – with ten being the best in terms of ease of threat detection in the image. An example of one montage window is shown in Figure 5.24. The ability of the screener to correctly click on the threat item location within the luggage was determined through use of a binary mask image. When the screener clicks on a specific (x, y) location in the image being evaluated, the program checks the same location in the corresponding mask image. If this pixel location has a value of 1, the answer is recorded as being correct.

Once all screeners have completed the evaluation, the composite set of data obtained was evaluated in Excel. Figure 5.25 presents a graphic showing the percent of all screeners who were able to correctly click on the threat location for the original image and each of the color enhancement methods. This graphic indicates that a low percentage (31%) of screeners were able to correctly locate the threat object in the original gray scale luggage scan. On the other hand, the color enhanced images fared much better with recognition rates ranging from 56.5 to 69.5%. The images with the color map "Springtime" had the highest recognition rate. This enhancement consists of histogram equalization, followed by image stretching, followed by application of color map "Springtime" developed in Subsection 5.4.1.2.

Another important evaluation criteria collected was the rating of each type of color coding. Figure 5.26 shows the graphic comparing the mean rating by screeners (10 maximum) of the original image and eight pseudo-colored procedures. Again, the original scored lowest (1.64) while the enhanced images were all significantly higher and in the range 2.56 to 5.24. That is an improvement of up to 219%. Color scale "Springtime" again obtained the highest rating in this category.

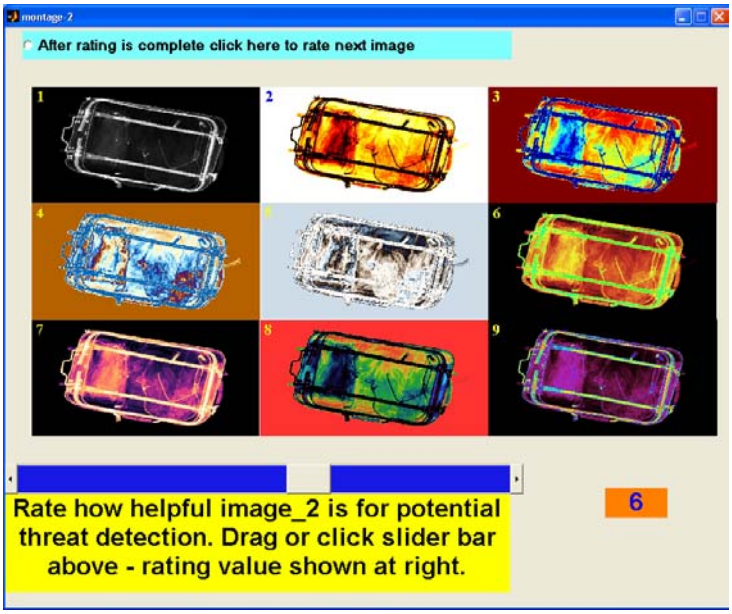

Figure 5.24 Montage of original and all color coded images for comparative rating**.**

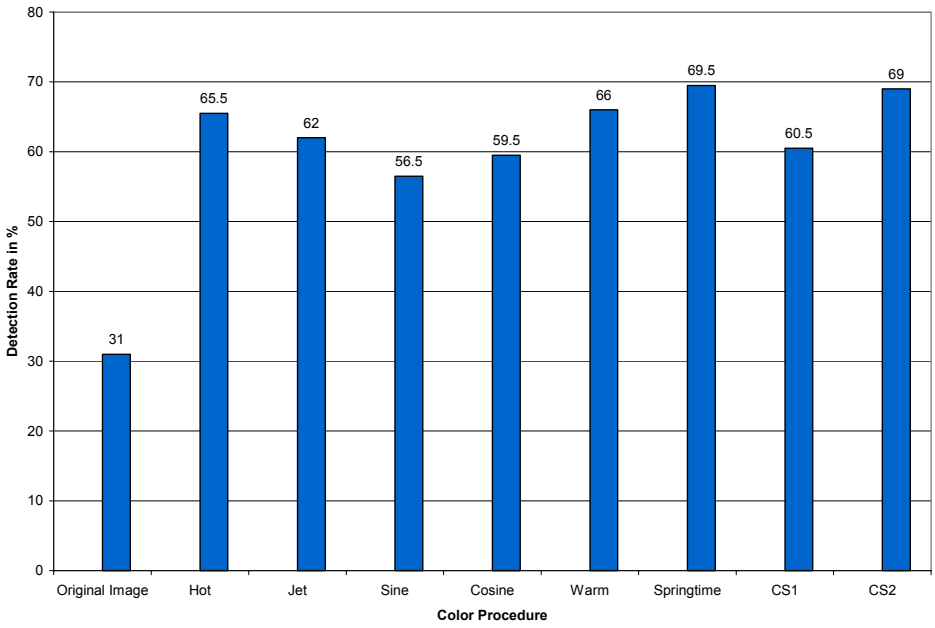

Figure 5.25 Percent of screeners able to correctly identify threat objects on each type of images.

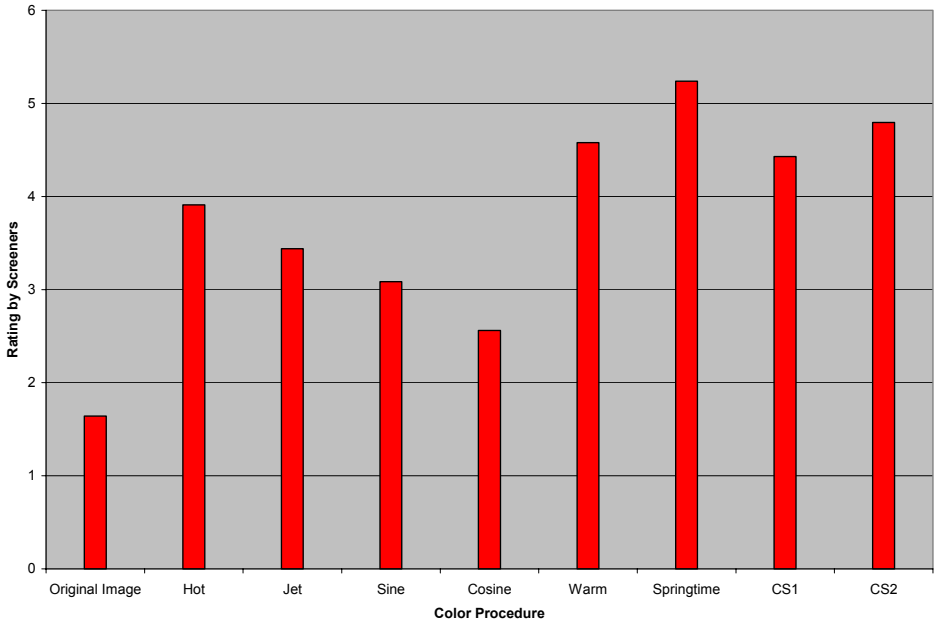

Figure 5.26 Mean ratings of eight pseudo-coloring approaches and gray level original obtained from screeners' evaluation.

The overall results obtained from the screeners' evaluations indicated a clear preference for color-enhanced x-ray scans over original gray scale luggage scans. The four approaches, "Warm", "Springtime", CS1 and CS2 received higher average ratings than the rest of the methods. Most of the four approaches, except "Warm", were designed based on the HSI color model, which confirms earlier remarks that the HSI color model is more suitable to human interpretation and therefore more effective in revealing low-density threats concealed in x-ray luggage scans.

5.6 Summary

A number of novel color transforms were introduced, applied to luggage scenes, and tested by screeners in an airport environment. Proper color mapping schemes have been designed based on human perceptive and cognitive features. The expectation that pseudo-coloring techniques can provide additional enhancement of x-ray luggage scans, better data visualization, increased screeners' alertness, and longer attention retention was demonstrated through experimental results and evaluations by actual airport screeners. In this chapter, we showed through visual interpretation, and more importantly through testing on TSA airport screeners that newly developed color-mapping techniques are very valuable tools in increasing the rate of low density threat detection in x-ray luggage scans. A significant increase of up to 97%, as compared to results from the original data, in the rate of threat detection was obtained when color coded data was used by screeners. Feedback from screeners also rated the color processed data, on average, up to 219%

more helpful in detecting threats than the raw data. Not only did the testing show that color processed data is more effective than gray scale data in detecting threat and keeping the screener's attention, but we were able to also rank the set of color mapping procedures in terms of the most effective and most appealing to screeners. In comparing the RGB-based approaches to the HSI-based approaches, the latter color space proved superior, which was expected given the many known advantages of the HSI space in human-based applications [Wei et al., 1997]. Future efforts will include more testing with the introduction of images containing no threat objects and others containing multiple threat items to study the performance in terms of false positive rates.

6 Dual-Energy X-Ray Image Fusion

The goal of image fusion here is to integrate complementary information from the low-energy x-ray image and the high-energy x-ray image such that the produced combined image is more amenable for a successful screeners' interpretation.

As introduced in Section 2.2.2, commercial dual energy x-ray luggage inspection systems, that fuse low-energy image and high-energy x-ray image into a single color image through estimating the atomic number of materials, result in a false alarm rate of roughly 30%. To reduce the false alarm rate and increase the threat detection rate, we explored other approaches to fuse dual-energy x-ray images.

6.1 Image Fusion using Local Spatial Information

6.1.1 Algorithm

This fusion method highlights details hidden or not clearly seen in original dual-energy images.

Assume that LowE denotes the low-energy x-ray image of a given luggage scene and HighE the corresponding high-energy x-ray image.

1. Find the difference image, *Diff*, using (6.1).

$$Diff = |LowE - HighE|, \tag{6.1}$$

2. Categorize each pixel in the given luggage scene as local background pixel or detail pixel.

   Generally, in one plane a pixel is classified into a local background pixel if its intensity value is close to the values of its surrounding pixels. Here the concept of local background pixel is extended to two planes, that is, the low-energy and high-energy images. If the pixel value in one plane is close to its corresponding pixel value in the other plane, the pixel is classified as a local background pixel. Otherwise, the pixel is classified as a detail pixel. Based on the above definition of local background pixel and detail pixel, a threshold is required to categorize each pixel. Allowing for some possible errors resulted in during image capture, we should set a small positive value as the threshold. For the dual-energy x-ray luggage images (256 gray levels) we have examined, the threshold value was set around gray level 10 and was found to work well for the pixel classification. Any pixel whose intensity value in the

difference image is greater than the threshold is categorized as a detail pixel; On the other hand, any pixel whose intensity value in the difference image is equal to or less than the threshold is categorized as a background pixel. Figure 6.1 depicts the process of this categorization.

3. Form a background image and a detail image.

   - Formation of the background image: To highlight details in the luggage scene, a smooth background is obtained by averaging the intensity values of the low-energy and high-energy images for the pixels categorized as background pixels, as given in (6.2).

$$\text{Background Image} = \begin{cases} (LowE + HighE)/2 & \text{for background pixels} \\ 0 & \text{for detail pixels} \end{cases} \tag{6.2}$$

   - Formation of the detail image: To have the pixels categorized as detail pixels have higher contrast with their neighbors, for any detail pixel, the intensity value in the detail image is taken from either the low-energy or the high-energy image according to the condition given in (6.3).

$$\text{Detail Image} = \begin{cases} \text{LowE} & \text{if } |R - HighE| < |R - LowE| \\ & \text{for detail pixels} \\ \text{HighE} & \text{if } |R - HighE| >= |R - LowE| \\ 0 & \text{for background pixels} \end{cases} \tag{6.3}$$

   where R is the response of a 3×3 averaging filter applied to the image obtained by averaging, $(LowE + HighE)/2$.

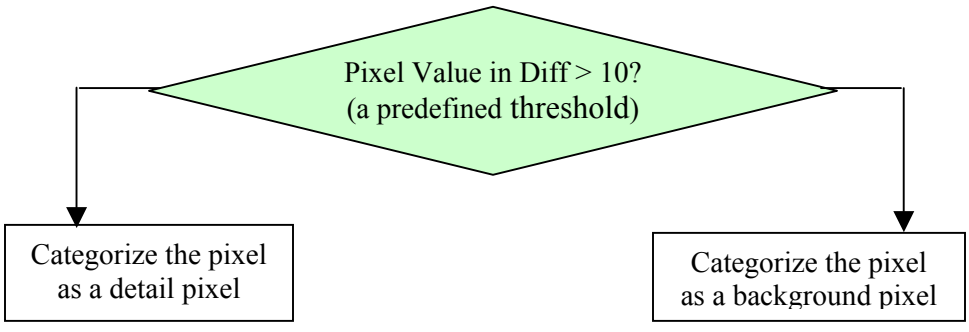

Figure 6.1 Categorization of the pixels in a given luggage scene as local background pixels or detail pixels.

4. Generate the combined grayscale image by adding the background image and the detail image.

The major steps of this proposed fusion approach are illustrated in Figure 6.2. Figure 6.3 (c) shows a combined grayscale image generated by applying this algorithm to dual-energy x-ray images in Figures 6.3 (a) and (b).

6.1.2 Noise Analysis and Noise Reduction

The fused results generated by directly applying the preceding proposed method to the original dual-energy images show the presence of noise. To characterize this noise, a small patch is analyzed from an area of the image where pixel values should be constant. Observing the shapes of the histograms of the small patches taken from the same spatial location of each pair of low and high-energy images, we approximate this noise with Gaussian function. Figure 6.4 shows a small patch selected from a luggage scene and the histograms for the small patches taken from the low and high-energy images of the same luggage scene.

To reduce the presence of noise, an adaptive and local noise-removal filter, Wiener filter good for Gaussian noise removal, is applied to the dual-energy images. Figure 6.5 shows the histograms of the noise-reduced versions of the same small patch as Figures 6.4 (b) and (c). It is obvious that the distribution ranges of the gray levels of the small patch decrease after noise removal. After performing noise reduction on the low-energy and high-energy images, the preceding fusion approach is employed to fuse the two noise-

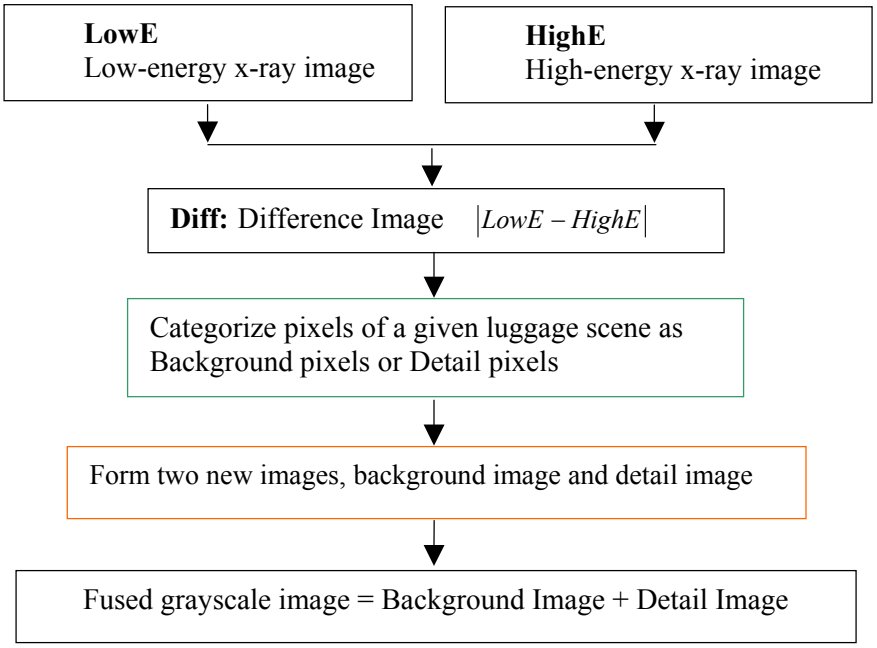

Figure 6.2 Flow chart of the developed approach for dual-energy x-ray image fusion.

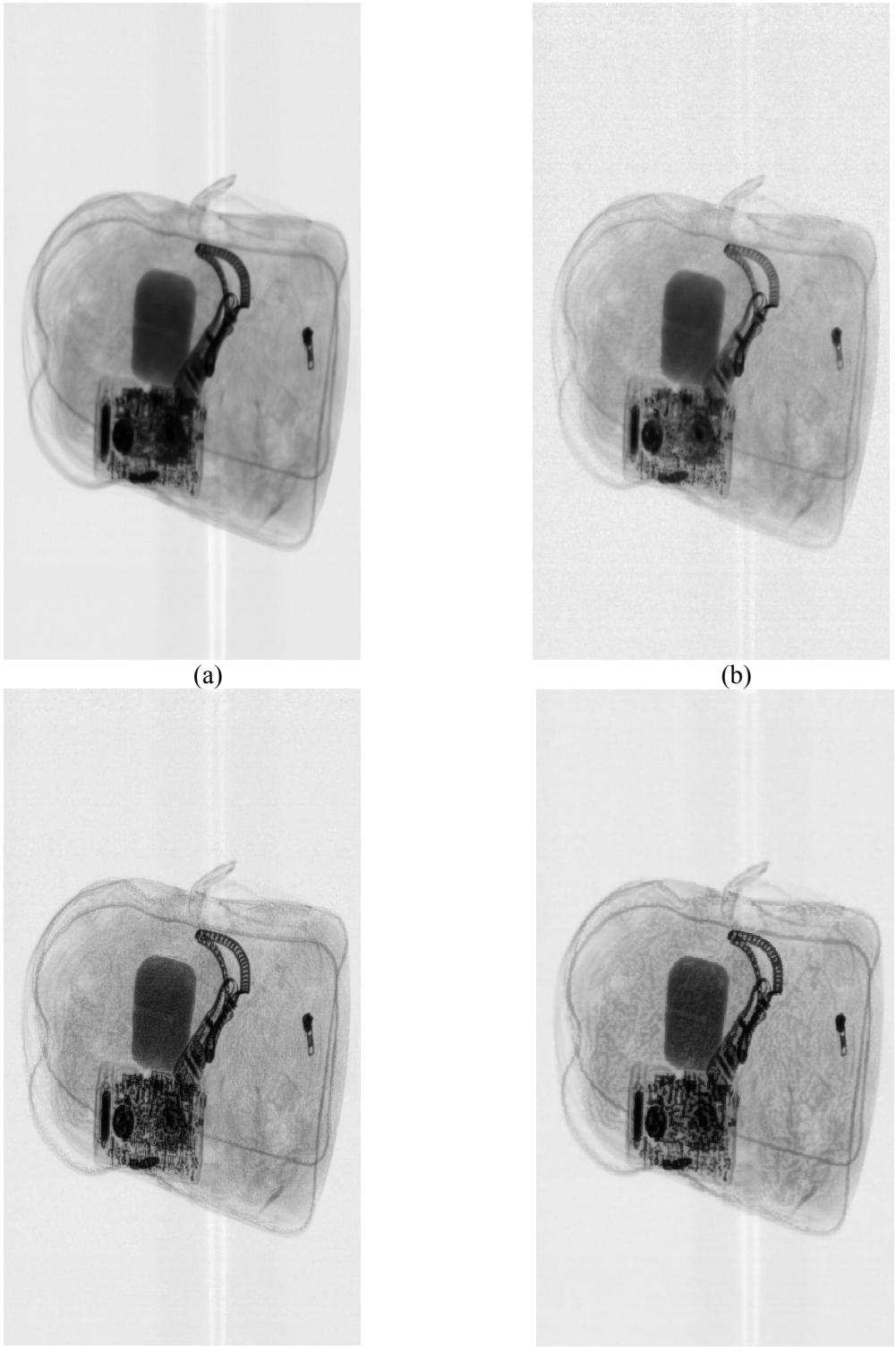

(a) (b)

(c) (d)

Figure 6.3 Dual-energy x-ray images and fused results generated using the local spatial information based fusion algorithm, (a) low-energy image, (b) high-energy image, (c) combined grayscale image, and (d) noise-reduced combined version.

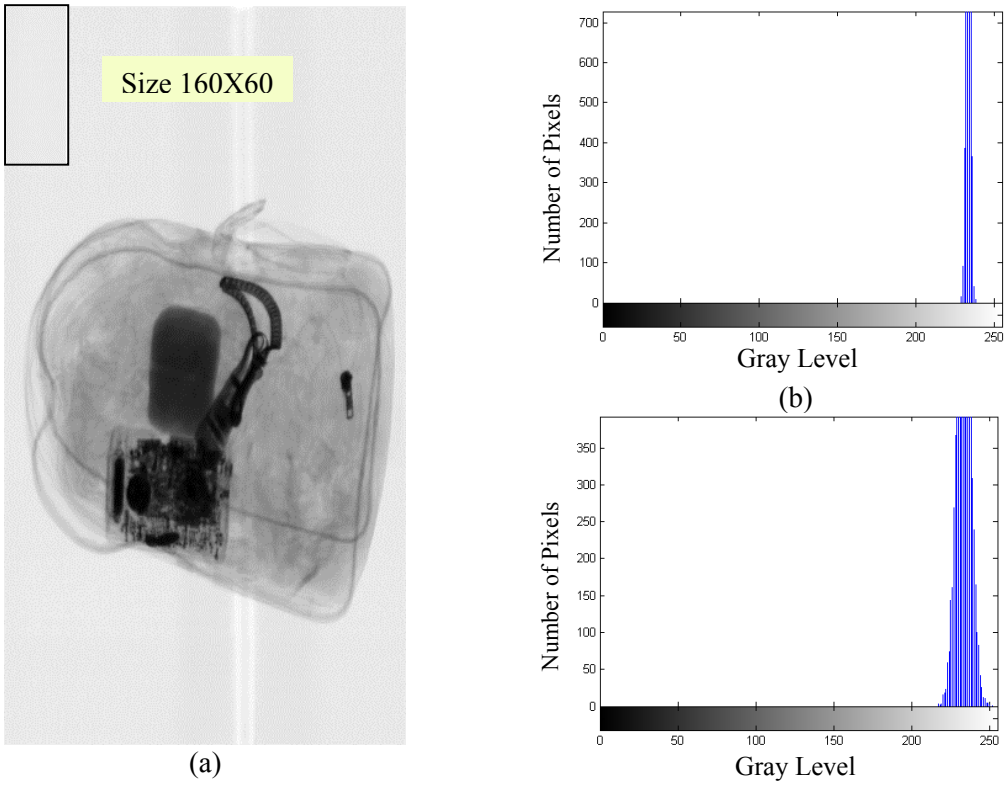

(a) (b) (c)

Figure 6.4 Noise analysis. (a) A selected small patch of size 160×60, (b) and (c) histograms of the small patches taken from the low-energy and the high-energy images.

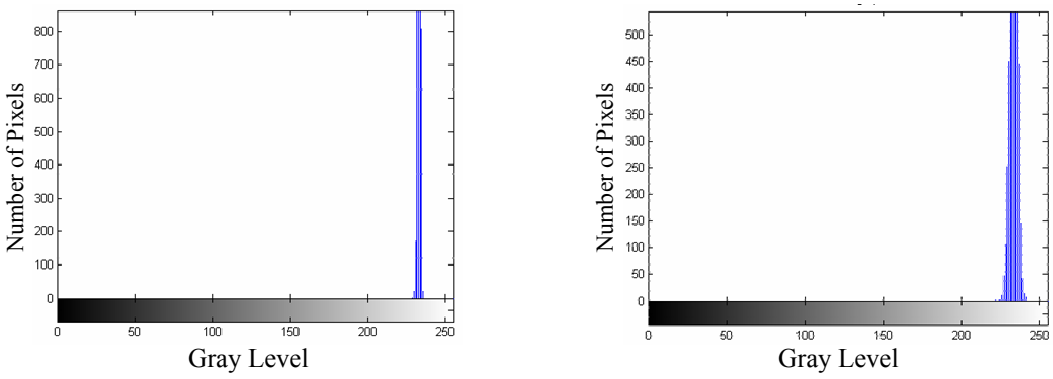

(a) (b)

Figure 6.5 Noise reduction. (a) Histogram of the noise-reduced version of the same small patch as used in Figures 6.4 (b), (b) histogram of the noise-reduced version of the same small patch as used in Figures 6.4 (c).

reduced versions. The resulting image generated by applying the proposed fusion approach to noise-reduced low-energy and high-energy x-ray images is referred to as noise-reduced combined version. Figure 6.3 (d) shows the noise-reduced combined version of the luggage scene.

Small patches are also taken at the same location as indicated in Figure 6.4 (a) from the directly combined version and the noise-reduced combined version of the luggage scene. As shown in Figure 6.6, the distribution range of the gray levels of the patch from the directly combined version and the noise-reduced combined version lies between those of the patches from the low-energy and high-energy images. This means that noise is not amplified by the fusion method proposed. The reason behind the appearance is most pixels in the small patch fall into background pixels and an averaging operation was performed on them.

6.2 Wavelet Based Image Fusion

6.2.1 Image Fusion with Wavelet Transform

The general procedure of fusing images based on wavelet transform is illustrated in Figure 6.7. First, the registered source images are each transformed into corresponding wavelet coefficient images using the discrete wavelet transform (DWT). Then, following a fusion rule, the fused wavelet coefficients are computed from the wavelet coefficients of the source images. The inverse DWT (IDWT) is then applied to the fused wavelet coefficients to obtain the fused image.

The fusion rule plays an essential role in the wavelet-based image fusion process. Two commonly used fusion rules, pixel based and region based rules, are introduced here. For pixel based fusion rule, the value of a fused wavelet coefficient is determined by the corresponding wavelet coefficients of the source images as depicted by the green pixels in Figure 6.8. Region based fusion rule not only utilizes the corresponding wavelet

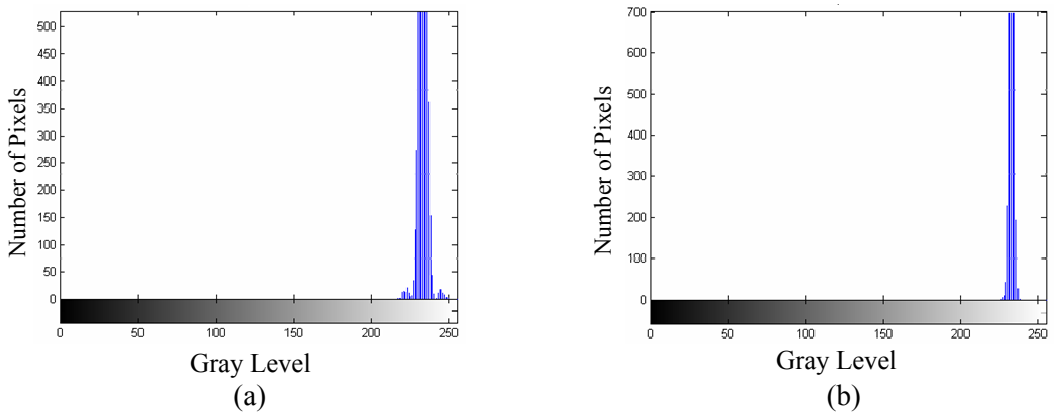

Figure 6.6 Noise reduction. (a) Histogram of the small patch taken from the combined version, (b) histogram of the small patch taken from the noise-reduced combined version.

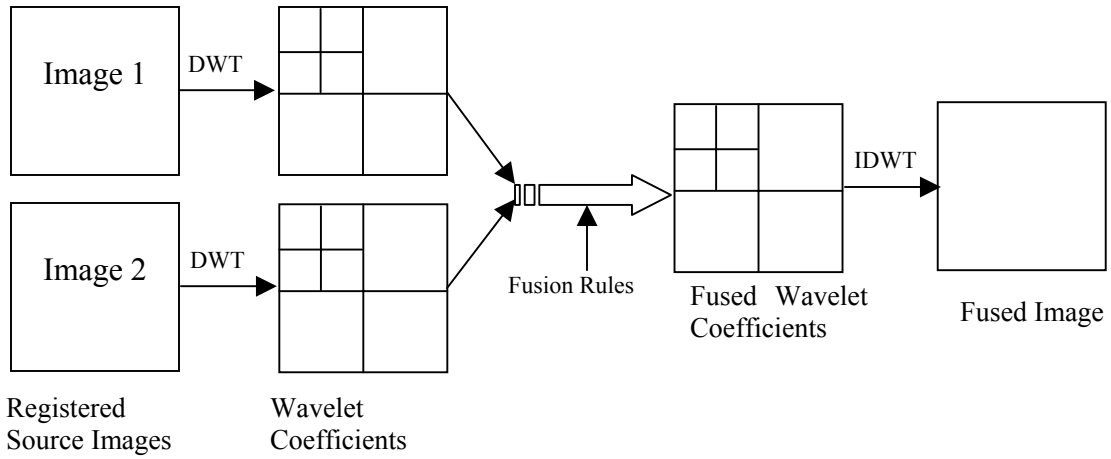

Figure 6.7 General procedure of image fusion with the wavelet transform.

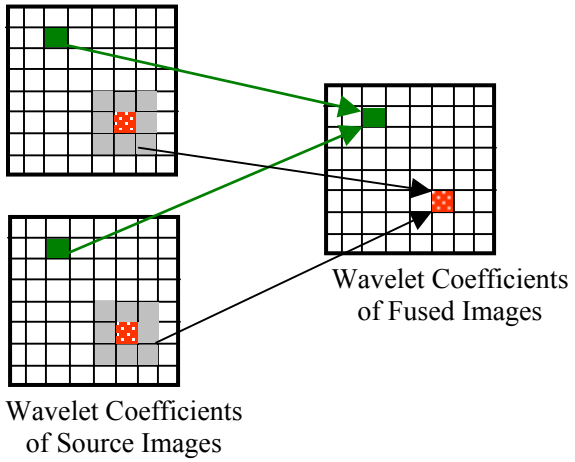

Figure 6.8 Two commonly used fusion rules: pixel based fusion rule (green) and region based fusion rule (red).

coefficients of the source images but also employs their surrounding wavelet coefficients to define a fused wavelet coefficient as shown by the red pixels in Figure 6.8.

6.2.2 Wavelet Based Fusion Algorithm for Dual-Energy X-Ray Images

As in Section 6.1.1, assume that LowE denotes the low-energy x-ray image of a given luggage scene; HighE the corresponding high-energy x-ray image; and FuseI the fused image obtained.

1. Compute the wavelet decompositions of LowE and HighE, seperately.

   To perform DWT on LowE and HighE and obtain their decompositions, a wavelet family and a wavelet basis able to represent enough image detail, need to be selected. A practical selection rule in image processing applications is to use a wavelet basis that can represent enough variation detail, regardless of its wavelet family. Another aspect needing to be determined is how many scales are necessary for the decomposition. Too few scales will cause too little detail to show in the fused image; On the other hand, too many scales will result in the fusion image not to be smooth enough for screeners to interpretation. Thus, to get a high-quality fusion image a compromise on the number of scales needs to be made.

2. Apply a low-pass filter to the approximation coefficients of LowE and the approximation coefficients of HighE to get the approximation coefficients of the fused version.

   The idea behind this step is a smooth approximation of a given scene can make the details in the scene more easily perceptible. Specifically, we generate each of the approximation coefficients of the fused image by averaging the corresponding approximation coefficients of LowE and HighE, as shown in (6.4).

   $$\text{approximation coefficients of FuseI} = (\text{approximation coefficients of LowE} + \text{approximation coefficients of HighE}) / 2 \tag{6.4}$$

3. Combine corresponding detail coefficients of LowE and HighE to get the detail coefficients of fused version.

   The idea behind this step is to have the details, uniquely exhibited in LowE or HighE, be incorporated into the fused version, and details existing in both LowE and HighE be more visible in the fused version. Specifically, we obtain each of the detail coefficients of the fused version, at all decomposition levels, by adding the corresponding detail coefficients of LowE and HighE, as shown in (6.5).

   $$\text{detail coefficients of FuseI} = \text{detail coefficients of LowE} + \text{detail coefficients of HighE} \tag{6.5}$$

The use of (6.5) as a way of combining the detail coefficients stem from an attribute exhibited in dual-energy x-ray images where distinct objects in a given luggage scene show similar general contours in both LowE and HighE.

4. Construct the fused image.

   The fused image, FuseI, is obtained by performing IDWT using the approximation coefficients and the detail coefficients, computed in Steps 2 and 3, respectively.

Figure 6.9 (c) shows a fused grayscale image generated by applying the wavelet-based fusion algorithm to dual-energy x-ray images in Figures 6.9 (a) and (b).

6.2.3 Noise Analysis and Reduction

To determine if noise is amplified during the fusion process while using the preceding wavelet-based fusion algorithm, a small region of a given luggage scene was selected for noise analysis as presented in 6.1.2. We calculated the mean and standard deviation of gray levels for the small region using each of the image patches cropped from the low-energy x-ray image, the high-energy x-ray image, and the fused image. Table 6.1, for example, gives the mean and standard deviation of gray levels of the small region illustrated in Figure 6.4 (a), computed by using data from the low-energy x-ray image, the high-energy x-ray image, and the fused image. Comparing their means and deviations, we can see that the noise presence in fused image version is slightly increased. Since it is very likely that the increase in noise level will cause the fused images to possess many artificial details, a question arises on "how can we reduce noise in the fused image?" A noise reduction step needs to be incorporated into the wavelet-based fusion algorithm. Observing the wavelet transform results of the dual-energy images, we found the noise appears in their corresponding detail coefficient images after wavelet decomposition. Figures 6.10 (a) and (b) are corresponding wavelet transform results of Figures 6.9 (a) and (b) where the number of scales was set to 4. To decrease the noise as much as possible with a little loss of useful information, the first-scale detail coefficient images are processed by using a hard thresholding method [Mathworks, 1994]. That is, find a threshold from a set of data − first-scale detail coefficients, and then set to 0 the first-scale detail coefficients whose absolute values are lower than the threshold. Different threshold selection rules can be used. For dual-energy x-ray luggage images, we finally chose the selection rule based on minimax principle [Mathworks, 1994] after observation and comparison of a set of experimental results. Figure 6.9 (d) shows the fused image version generated after the application of noise reduction. We used the small patch, corresponding to the patch shown in Figure 6.4(a), from Figure 6.9 (d) and obtained its mean and standard deviation shown in the fourth row of Table 6.1. Comparing with the fused version before noise reduction, we see a significant noise decrease in levels. After the incorporation of noise reduction, noise level now resides between the noise levels of its corresponding high-energy and low-energy images while there is no any perceptible loss to the quality of the fused image.

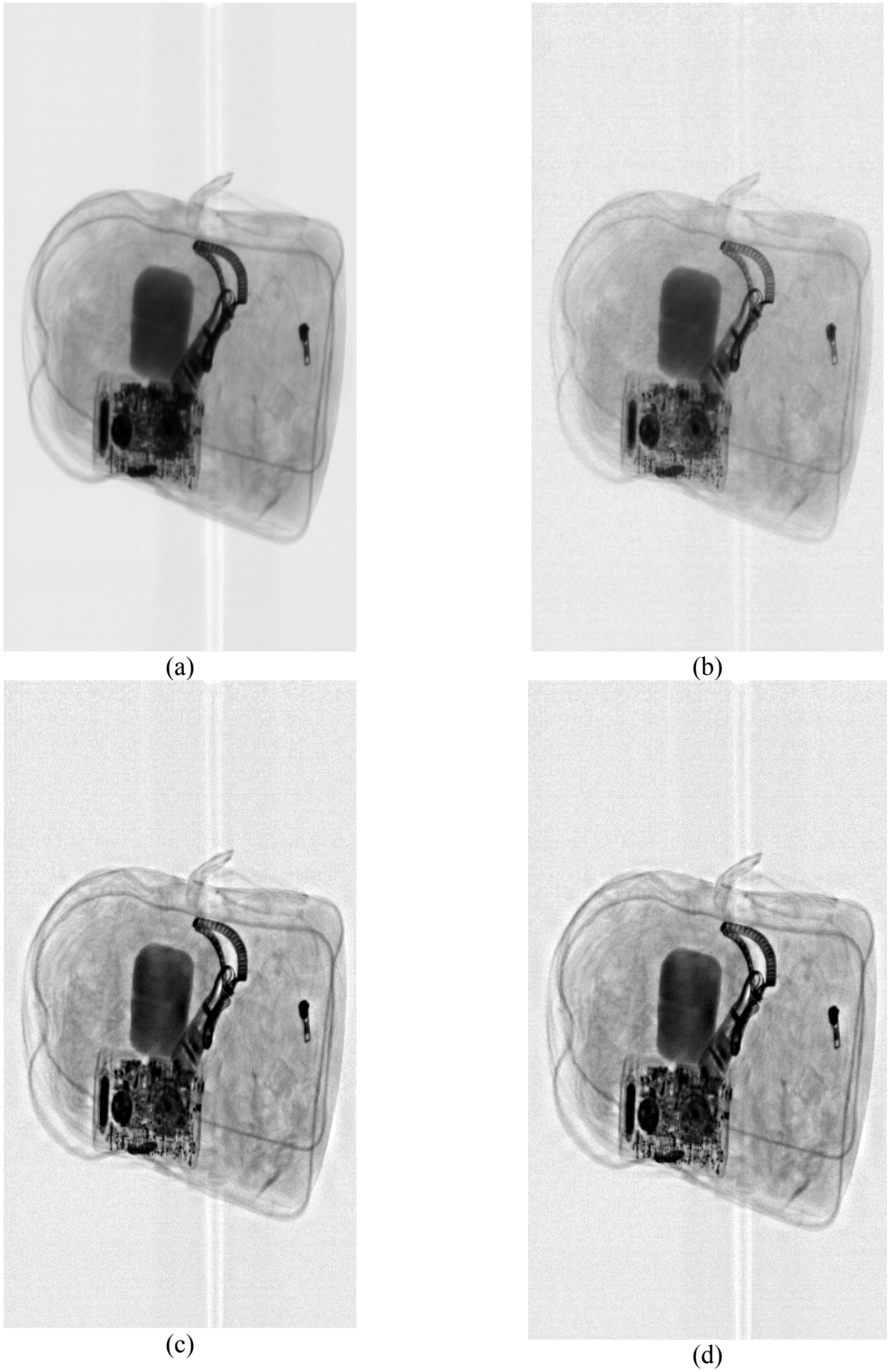

(a) (b)

(c) (d)

Figure 6.9 Results of wavelet-based fusion algorithm, (a) and (b) low-energy and high-energy x-ray images, and (c) and (d) fused image generated using wavelet-based fusion algorithm, before and after the application of noise reduction.

Table 6.1 Means and standard deviations of gray levels of the small region shown in Figure 6.4 (a), computed by using data from the low-energy x-ray image, the high-energy x-ray image, and the fused image generated using wavelet-based fusion method before and after noise reduction.

Parameter / Patch	Mean	Standard Deviation
Low-Energy	233.4935	1.5159
High-Energy	233.3541	18.0587
Fused	232.9319	18.8955
Fused after noise reduction	232.9258	12.9902

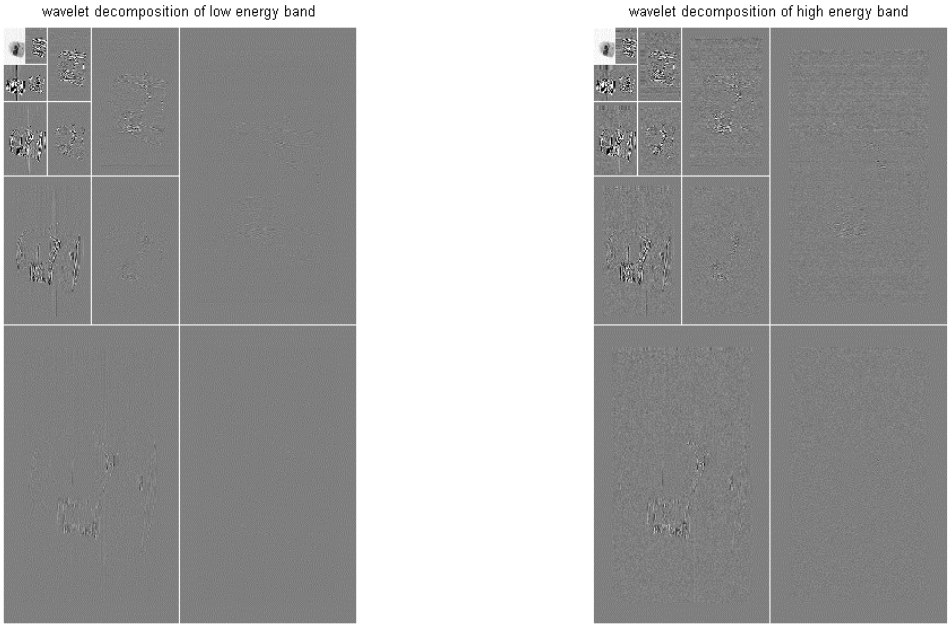

(a) (b)

Figure 6.10 Noise analysis. (a) and (b) Wavelet transforms of Figure 6.9 (a) and (b).

6.3 Color-Coding of Fused Images

A pseudo coloring scheme is proposed and applied to fused dual energy data. The algorithm is described as follows:

1. Segment the difference image obtained from (6.6) using a histogram based thresholding method.

$$Diff = LowE - HighE \text{ or } Diff = HighE - LowE , \tag{6.6}$$

   The underlying reason for this segmentation is due to the fact that the range of differences is usually function of the properties of objects such as objects' density and thickness.

2. Designate a given chromaticity (H and S) for each class.

3. Feed the fused image into brightness channel (I).

The color images produced using the above method indicate similarities and dissimilarities between objects' properties for those objects of same/different chromaticities.

6.4 Experimental Results

A number of pairs of dual-energy x-ray images are examined by using the two proposed fusion methods described in Sections 6.1 and 6.2.

6.4.1 Image Fusion Using Local Spatial Information

Results produced by applying the proposed algorithm in Section 6.1 to three pairs of dual-energy x-ray images are shown in this section. For the generation of all combined versions, the threshold was set to 10. Besides, as for noise removal, the size of the Wiener filter was 3×3. Figures 6.11 6.12 and 6.13 each show the raw dual-energy x-ray images, the directly combined version, and the noise-reduced combined version, of each one of the three luggage scenes.

6.4.2 Wavelet-Based Dual-Energy X-Ray Image Fusion Approach

This section shows the results produced by applying the wavelet-based fusion algorithm presented in Section 6.2 to two pairs of dual-energy x-ray images. As discussed in 6.2.2, a wavelet family (a wavelet basis) and the number of scales need to be determined for the decomposition of original dual-energy images. Through a series of experiments, we selected Daubechies wavelet transform and specified 4 scales in our fusion process. Figures 6.14 and 6.15 each show the raw dual-energy x-ray images, the directly fused

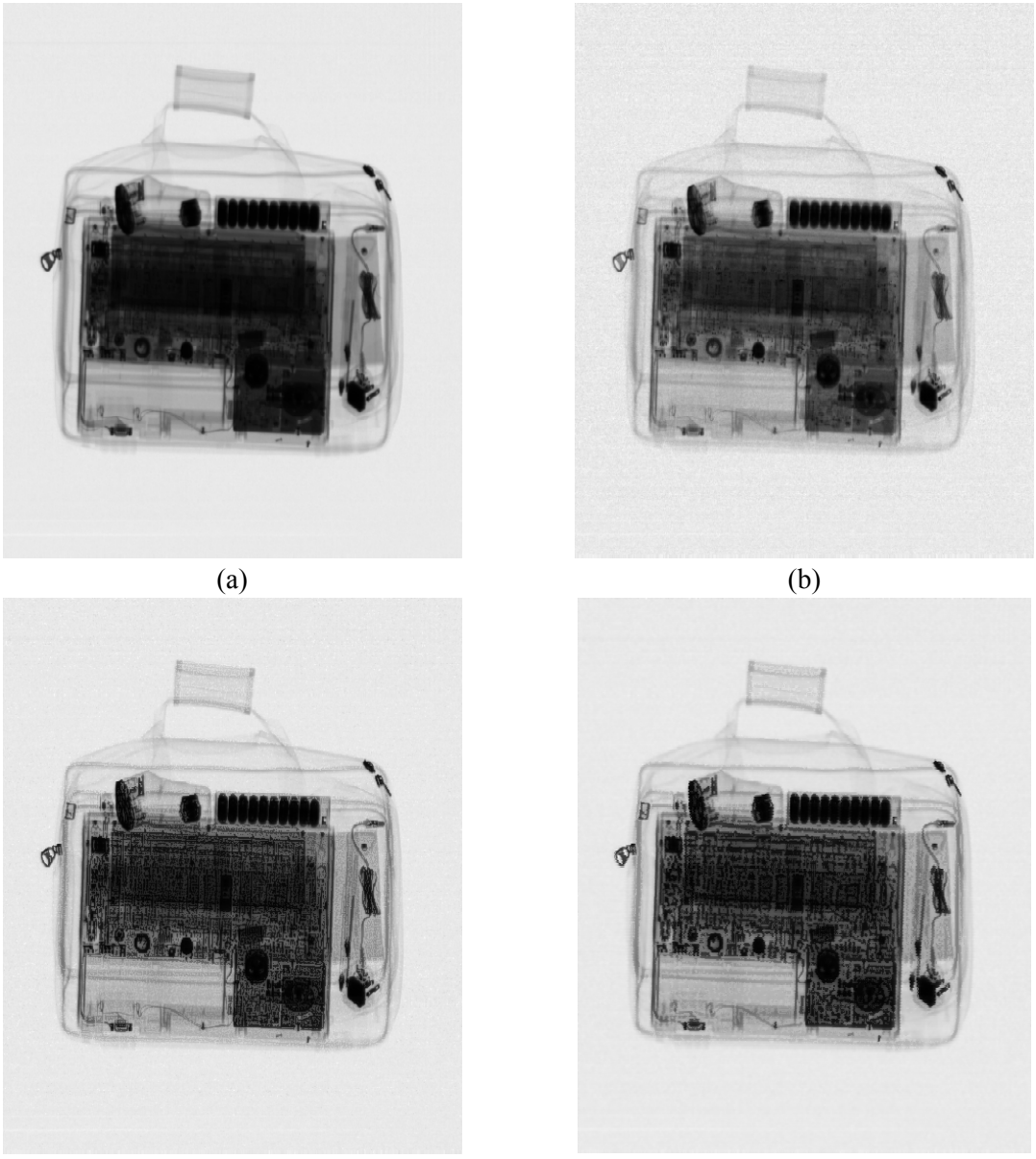

(a) (b)

(c) (d)

Figure 6.11 Dual-energy x-ray images and fused results generated using the algorithms presented in Section 6.1 (a) low-energy image, (b) high-energy image, (c) combined grayscale image, and (d) noise-reduced combined version.

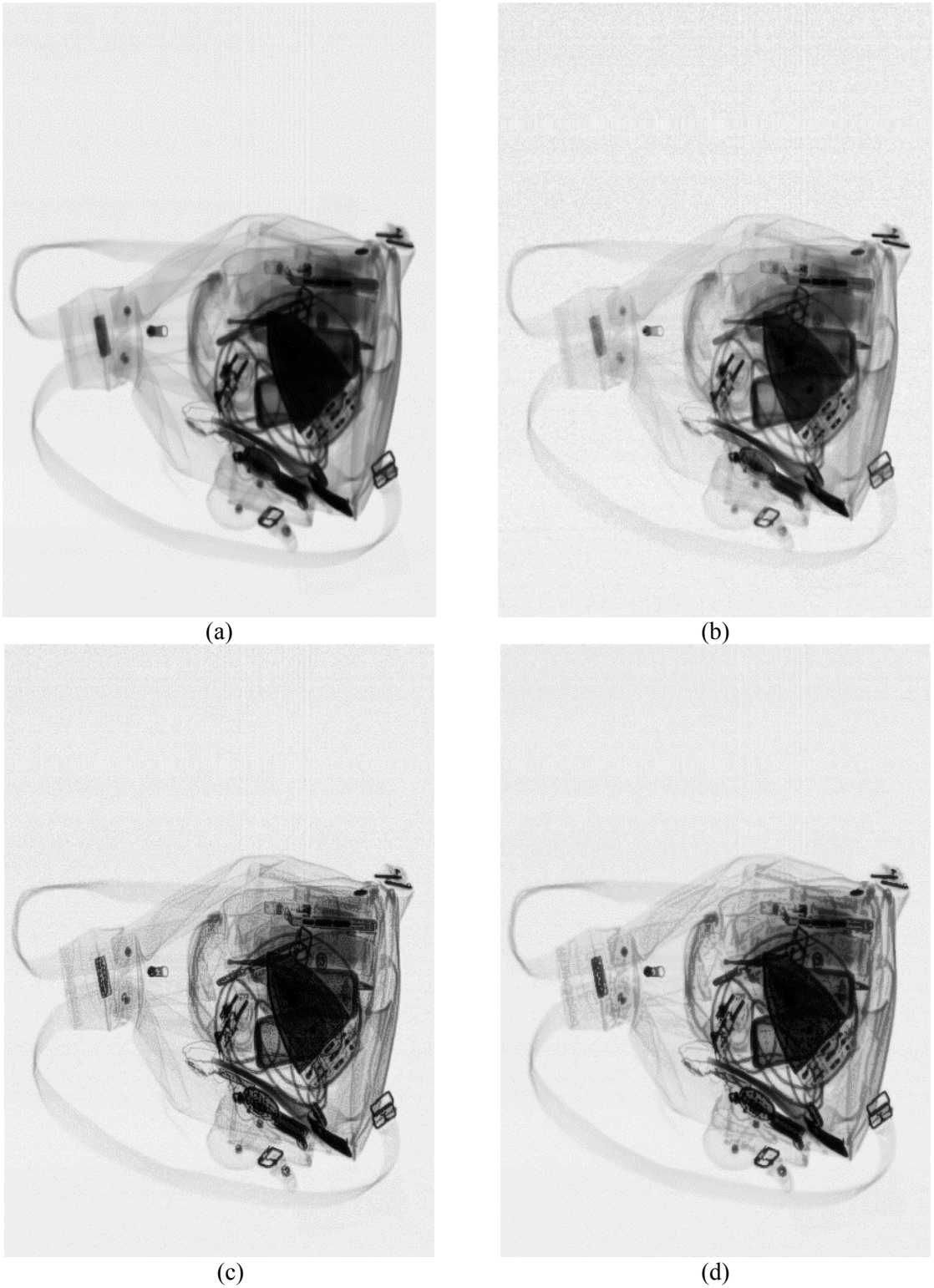

(a) (b)

(c) (d)

Figure 6.12 Dual-energy x-ray images and fused results generated using the algorithms presented in Section 6.1 (a) low-energy image, (b) high-energy image, (c) combined grayscale image, and (d) noise-reduced combined version.

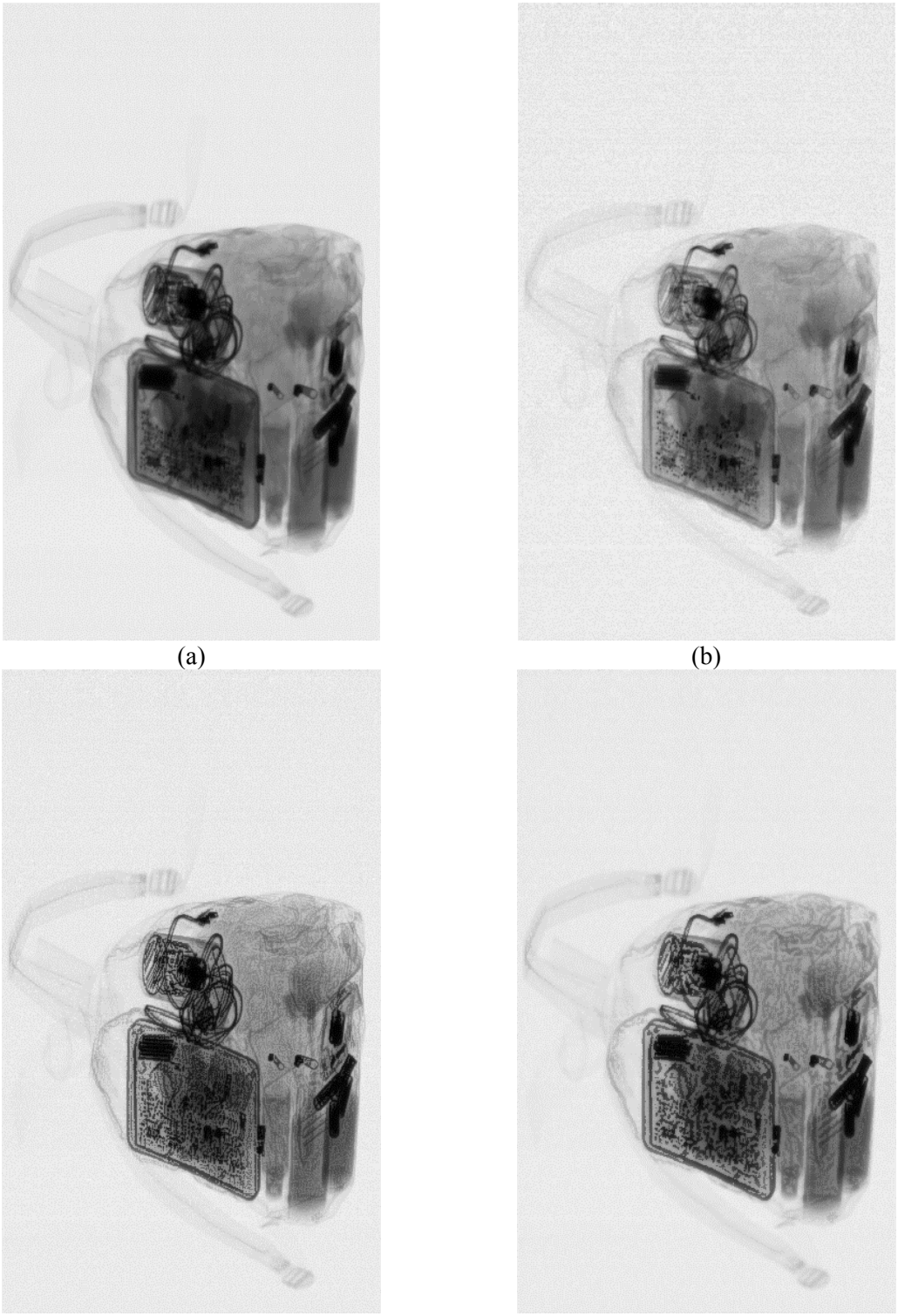

(a) (b)

(c) (d)

Figure 6.13 Dual-energy x-ray images and fused results generated using the algorithms presented in Section 6.1 (a) low-energy image, (b) high-energy image, (c) combined grayscale image, and (d) noise-reduced combined version.

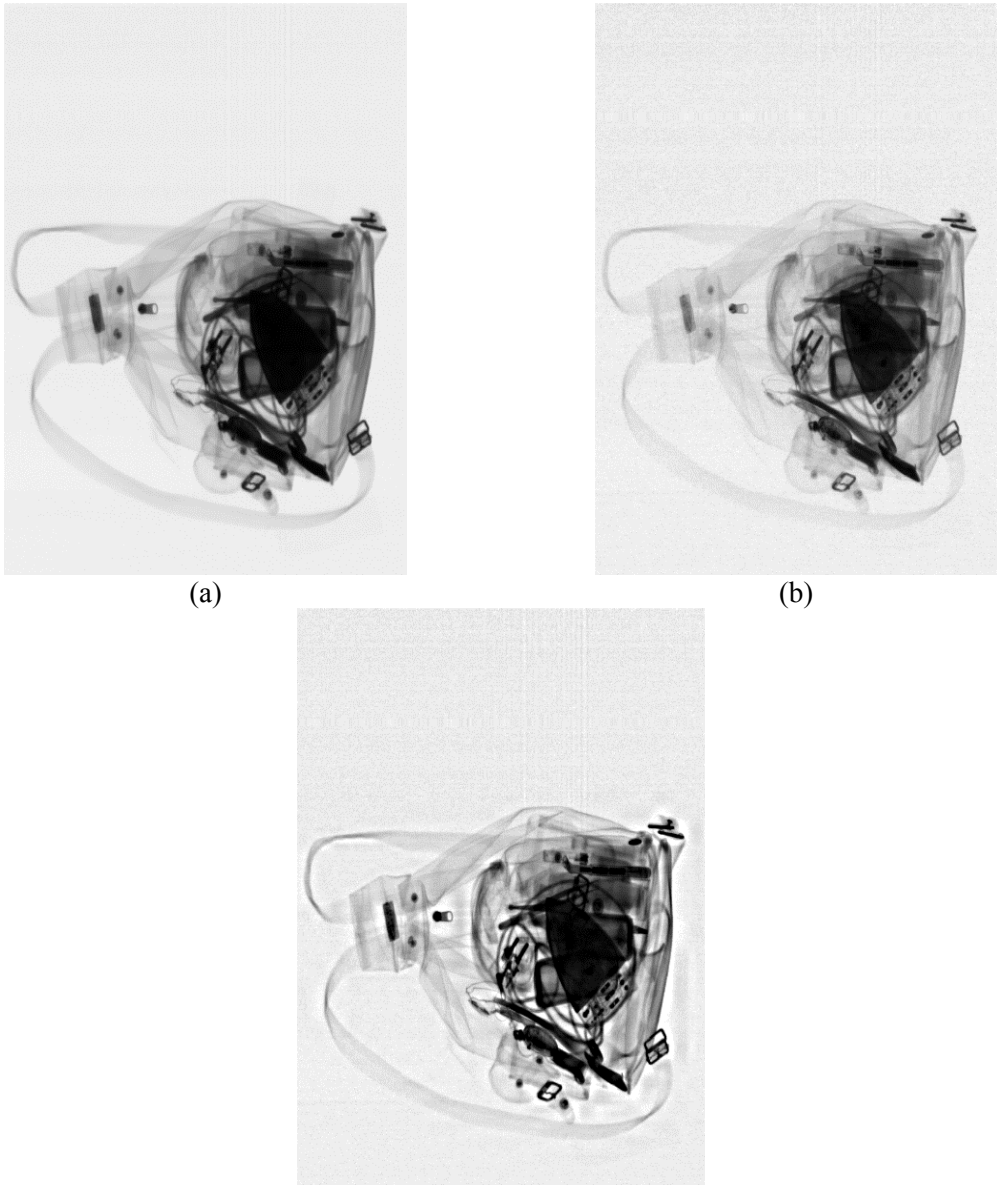

(a) (b)

(c)

Figure 6.14 Results of wavelet-based fusion algorithm, (a) low-energy x-ray image (b) high-energy x-ray image, (c) fused image generated by using wavelet-based fusion algorithm.

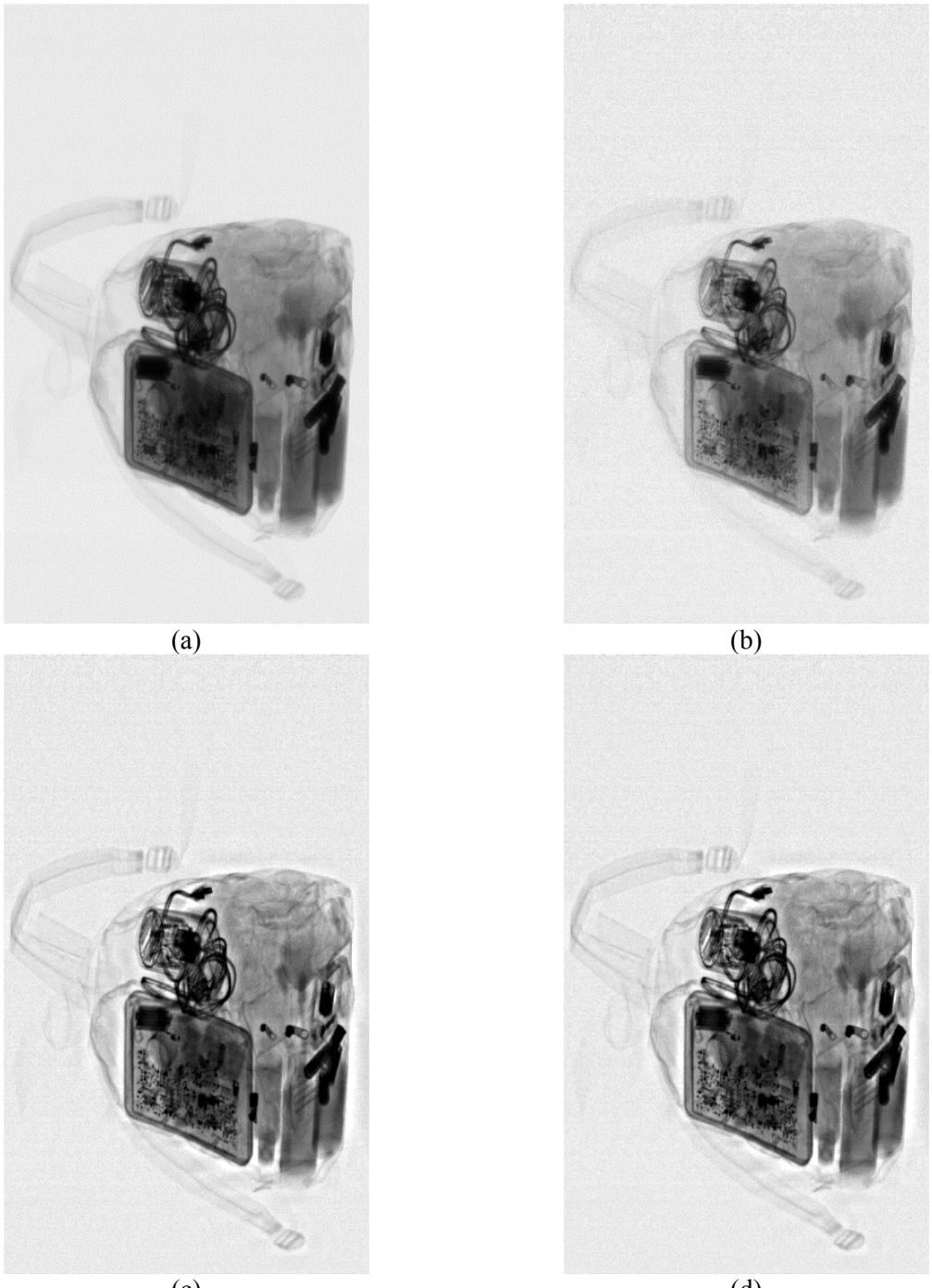

(a) (b)

(c) (d)

Figure 6.15 Results of wavelet-based fusion algorithm, (a) low-energy x-ray image (b) high-energy x-ray image, (c) fused image generated by using wavelet-based fusion algorithm, and (d) fused image version generated by incorporating noise-reduction step into the wavelet-based fusion algorithm.

image version, and the noise-reduced fused image version, of each one of the two luggage scenes.

6.4.3 Color Coding of Fused Images

We used three color-coding schemes to color the fused images obtained in the previous sections. The first scheme directly applies an established color scale to the fused version; The second applies an HSI-based color coding approach − constant saturation (CS) introduced in Section 5.4.2 of Chapter 5; and the third is the one presented in Section 6.3.

The "Warm" scale presented in Section 5.3.1 of Chapter 5 and Set 1 shown below (CS) were used to generate the color results in Figures 6.16 and 6.17.

Set 1:

Combined grayscale image → H
Constant 0.8→ S
Combined grayscale image + gamma correction →I

Several luggage scenes were color-coded using color Scheme 3. Preliminary experimental results for the two luggage scenes in Figures 6.18 (a) and (b) are shown in Figures 6.19 (a) and (b), respectively. Figures 6.18 (c) and (d) illustrate the histograms of difference images corresponding to luggage scenes in Figures 6.18 (a) and (b). We manually picked two thresholds, as indicated in Figures 6.18 (c) and (d) with red arrows, for segmenting items in each of the two luggage scenes. Three hues, white, yellow and green, were chosen and each of them in sequence was assigned to a class of items.

6.5 Objective Evaluation of Fused Images

In-house visual assessment of fused x-ray images, produced by applying the proposed fusion algorithms described in Sections 6.1 and 6.2 to a number of distinct luggage scenes, have indicated the effectiveness of such algorithms in differentiating different kinds of objects in luggage. As a large size of observers is required to obtain more reliable judging of the effectiveness of these fusion approaches, we attempted to seek objective image quality measures that correlate acceptably well with the perceived image quality. This will also reduce the overhead of human assessment.

Efficient image quality measures are sought among various existing IQMs, as described in Section 2.6, for the assessment of fused images. Because of the extreme difficulty in defining good reference images in our case, our focus was measures from the class of NRIQM.

Nill et al. [Nill et al., 1992] developed an NRIQM derived from the image power spectrum of normally acquired arbitrary scenes, utilizing previously known invariance property of the power spectra of arbitrary scenes. This measure is selected to evaluate our fused x-ray images because of the following features: (1) It is a rapid and automated

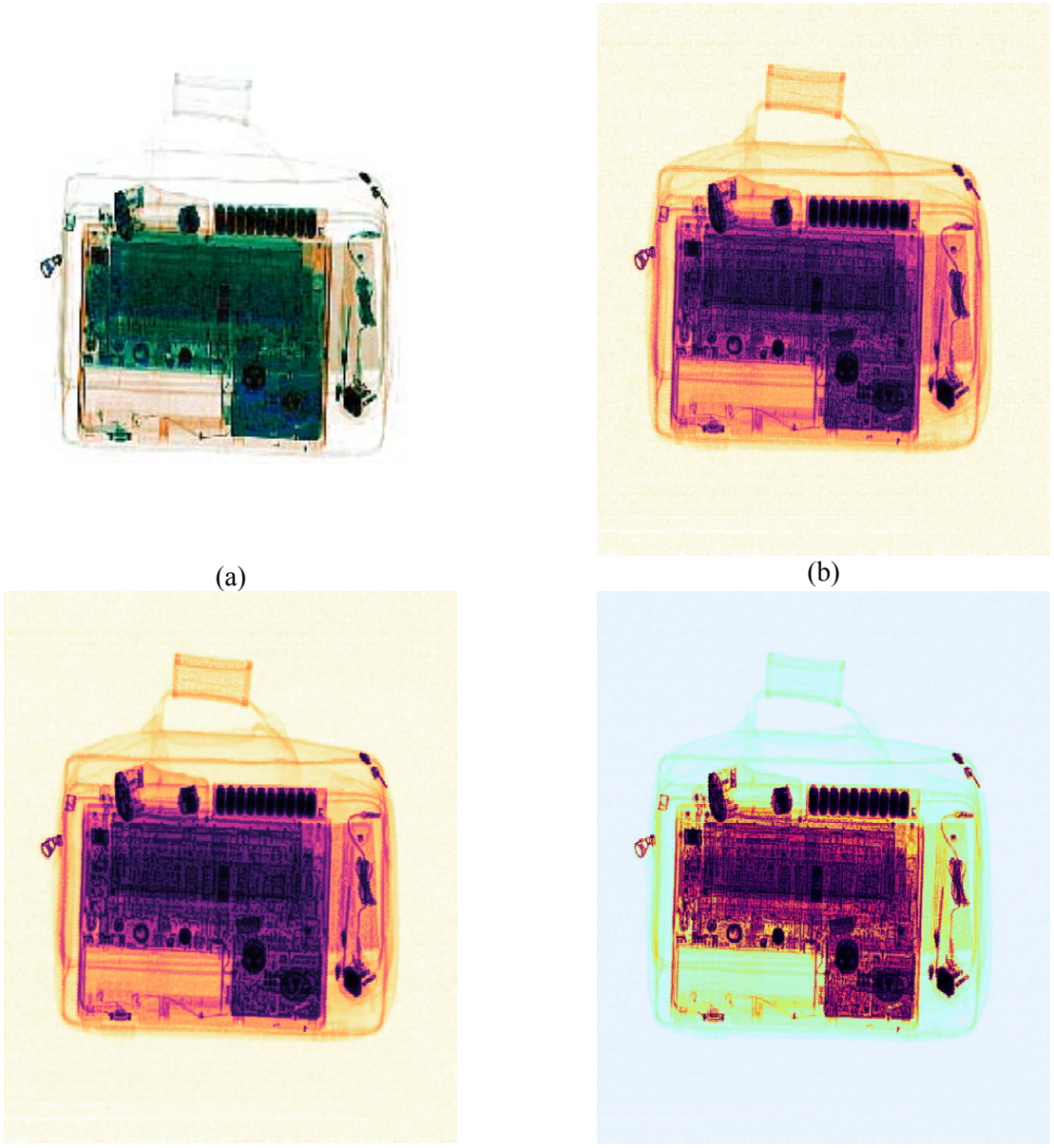

(a) (b)

(c) (d)

Figure 6.16 Color versions (a) manufacturer's color image, (b) & (c) color versions obtained by applying "Warm" scale to Figure 6.17 (c) and (d), respectively, (d) color version obtained by applying Set 1 to Figure 6.17 (c).

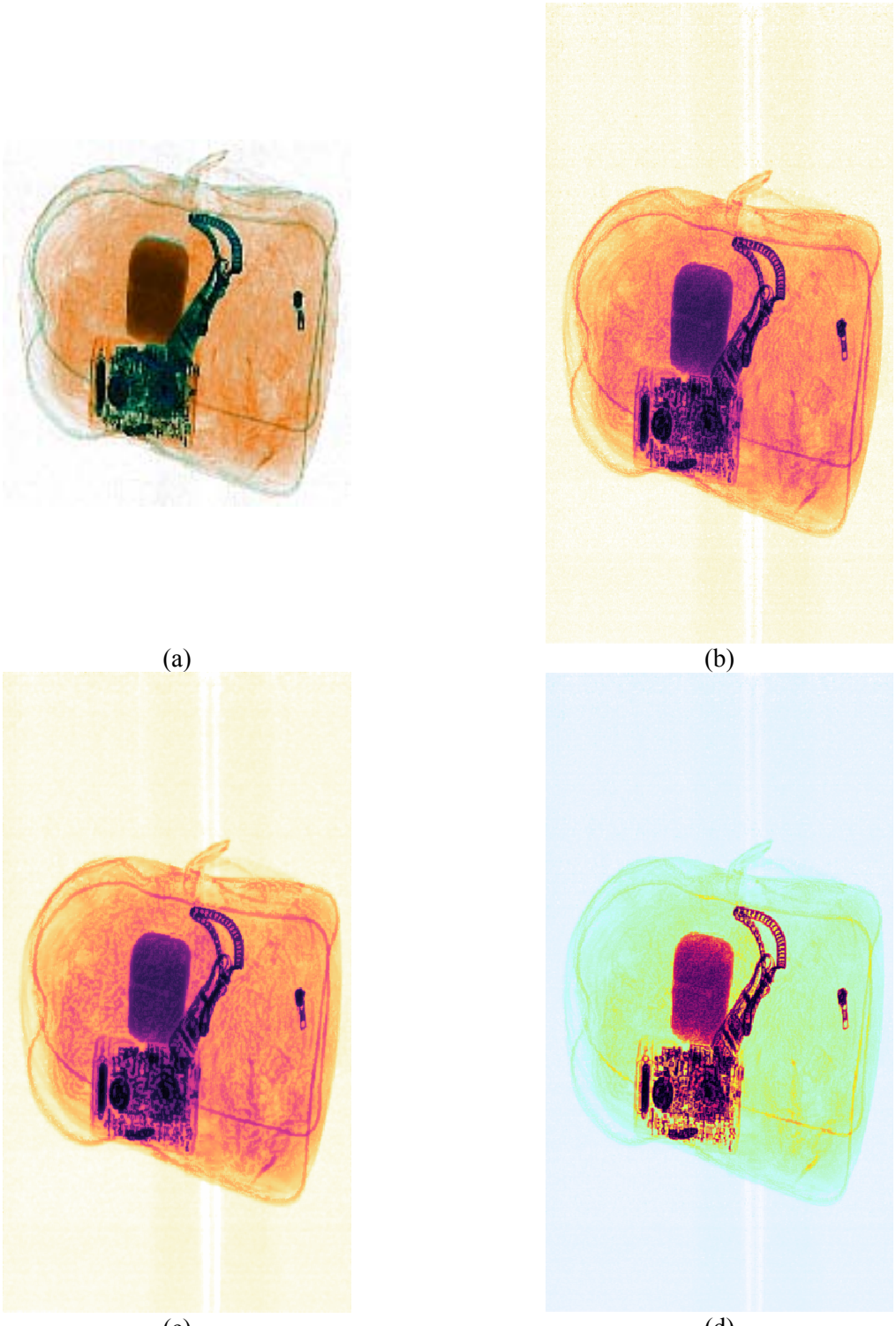

(a) (b)

(c) (d)

Figure 6.17 Color versions (a) manufacturer's color image, (b) & (c) color versions obtained by applying "Warm" scale to Figure 6.3 (c) and (d), respectively, (d) color version obtained by applying Set 1 to Figure 6.3 (c).

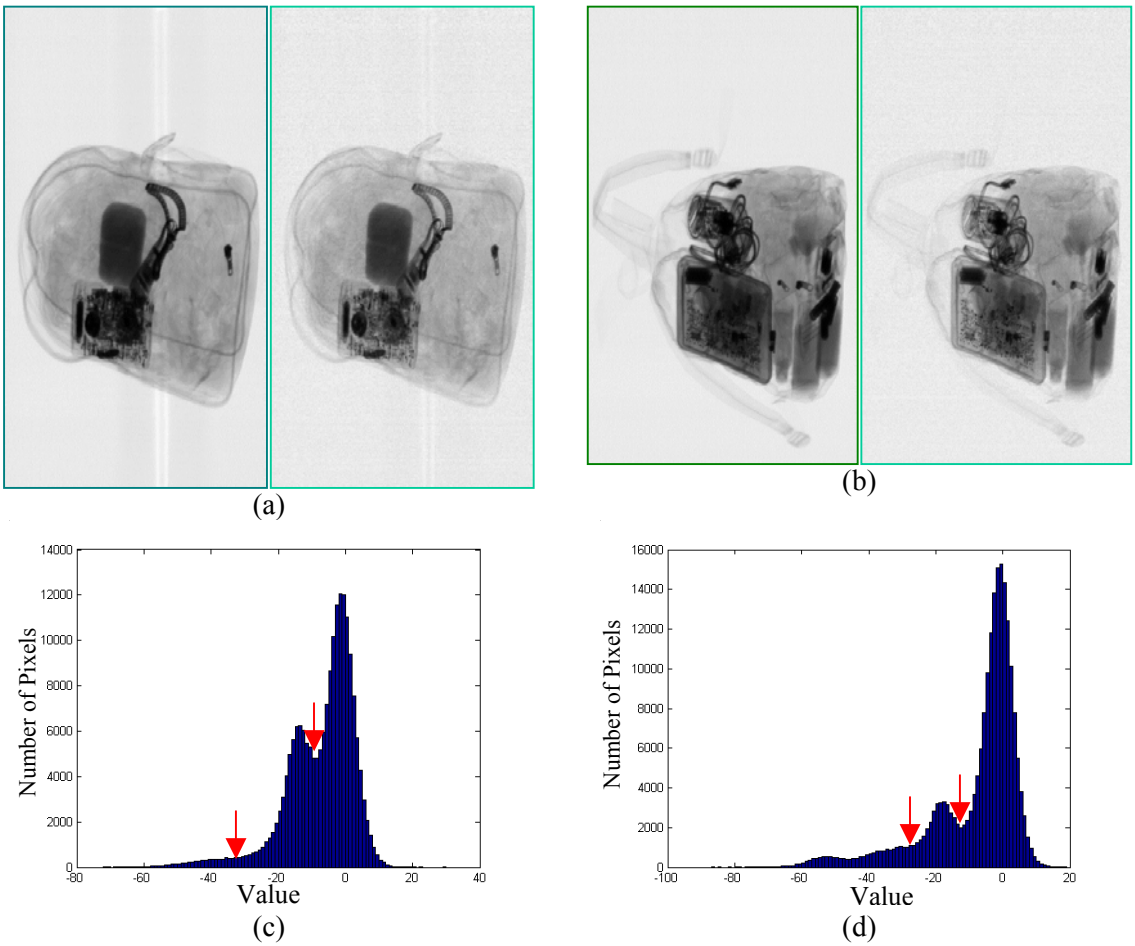

Figure 6.18 Histograms of difference images. (a) and (b) Two pairs of dual-energy x-ray images, (c) and (d) histograms of the difference images corresponding to (a) and (b).

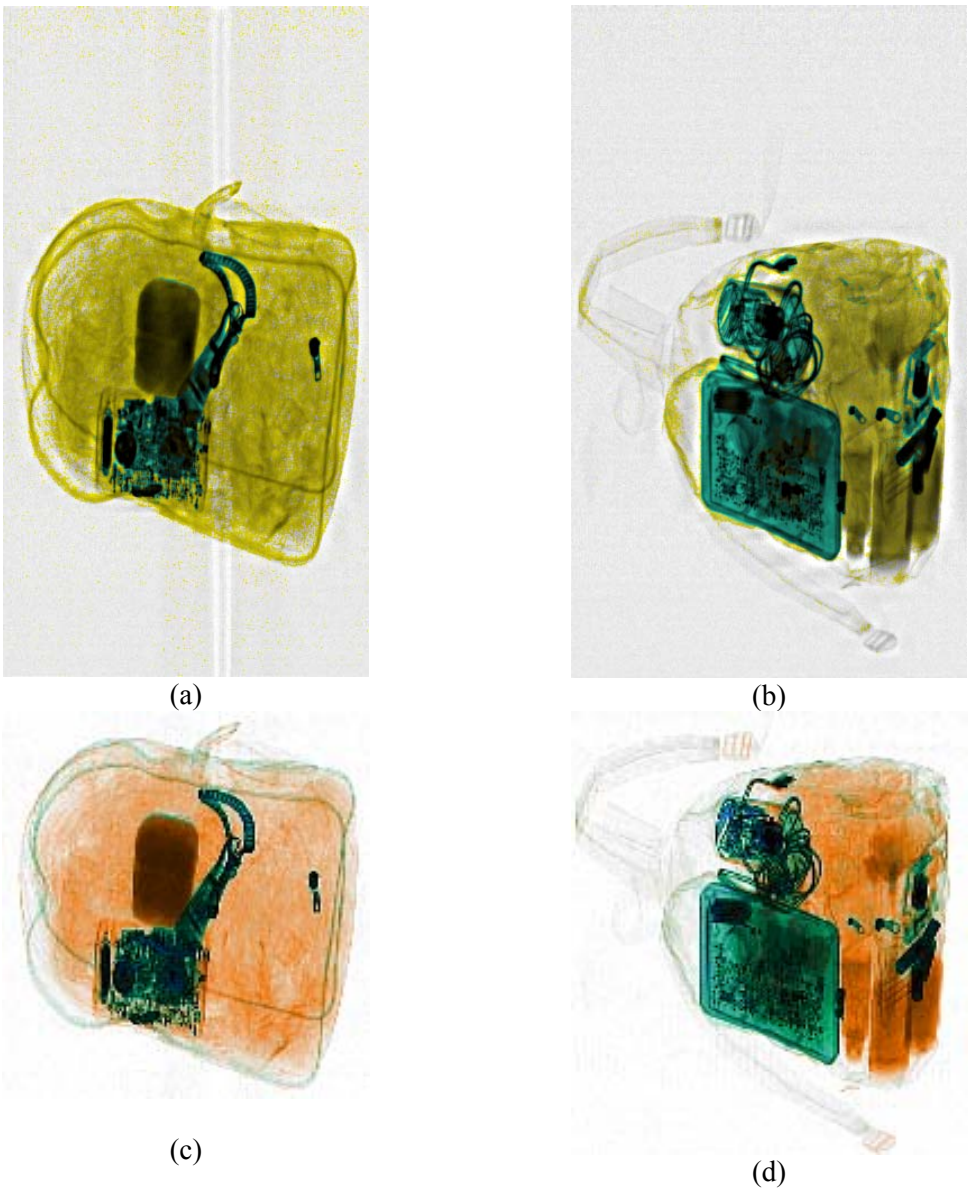

(a) (b)

(c) (d)

Figure 6.19 Color versions, (a) and (b) color images produced using color Scheme 3, (c) and (d) manufacturer's color images.

objective NRIQM; (2) Researchers' experimental verification demonstrates a very good correlation (r=0.9) of this objective quality measure with the visual quality assessment as shown in Figure 6.20; (3) It is applicable to the tasks of detection, recognition and identification of man-made objects in images.

The IQM of Nill et al. is derived from the normalized 2-D power spectrum $P(\rho,\theta)$ weighted by the square of the modulation transfer function of the human visual system $A^2(T\rho)$, the directional scale of the input image $S(\theta_1)$, and the modified parameter Wiener noise filter $W(\rho)$ [Nill et al., 1992]. The IQM is given by

$$\text{IQM}=\frac{1}{M^2}\sum\sum S(\theta_1)W(\rho)A^2(T\rho)P(\rho,\theta), \tag{6.7}$$

where M^2 is the image size in pixels; ρ,θ spatial frequency in polar coordinates.

Figures 6.21 and 6.22 show the results obtained by applying the above IQM to two pairs of x-ray luggage images, respectively, where IQMs computed with (6.7) are converted into National Imagery Interpretability Rating Scale (NIIRS) [NIIRS, 1998] to easily compare with the visual evaluation results. NIIRS is defined by the aerial imaging community to measure the quality of images and the performance of imaging systems. The NIIRS consists of 10 graduated levels referred to as 0 to 9, with several interpretation tasks or criteria forming each level. These criteria indicate the amount of information that can be extracted from an image at a given interpretability level. With a NIIRS 2 image, for example, analysts should be able to detect large buildings, while on NIIRS 6 imagery they should just be able to identify automobiles as sedans or station wagon [Guide, 1998].

As shown in Figures 6.21 and 6.22, NIIRS values of fused images in comparison with the NIIRS values of their corresponding original dual-energy images indicate image interpreters are able to identify more objects in a luggage scene from the fused image than from the original image. This demonstrates that x-ray image quality is effectively

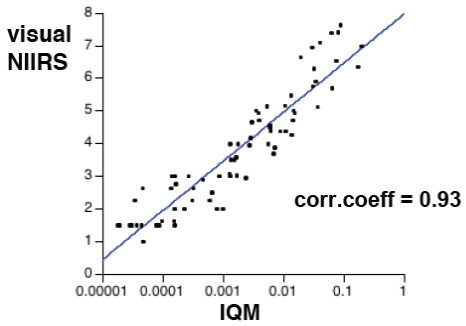

Figure 6.20 IQM vs. Visual National Imagery Interpretability Rating Scale (NIIRS) [Nill et al., 1992].

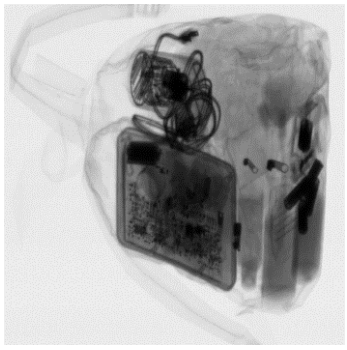

NIIRS = 7.40689
(a)

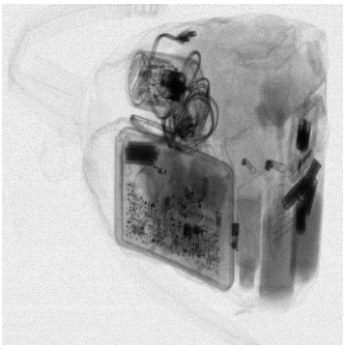

NIIRS = 7.24497
(b)

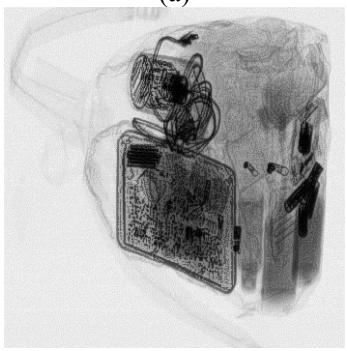

NIIRS = 7.91971
(c)

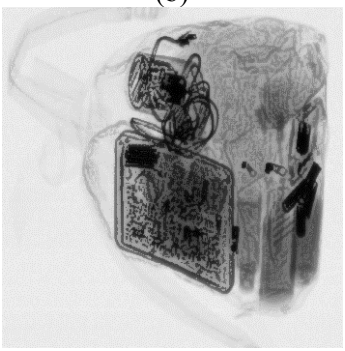

NIIRS = 7.76784
(d)

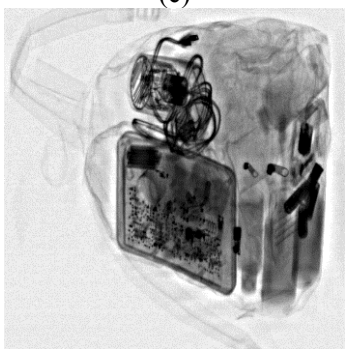

NIIRS = 7.94778
(e)

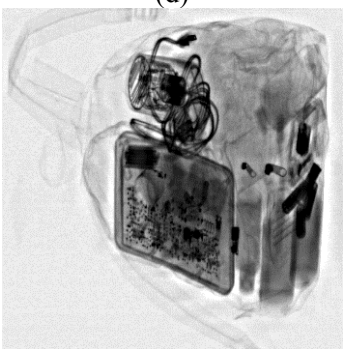

NIIRS = 7.94516
(f)

Figure 6.21 Evaluation results by applying the IQM of Nill's et al. to the luggage scene in Figure 6.3. (a) Low-energy image, (b) high-energy image, (c), (d) combined grayscale image and noise-reduced combined version generated using local-spatial-information based fusion algorithm, (e) fused image generated by using the wavelet-based fusion algorithm, and (f) fused image version generated by incorporating a noise-reduction step into the wavelet-based fusion algorithm.

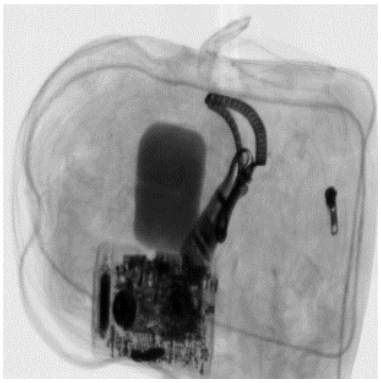

NIIRS = 7.51761
(a)

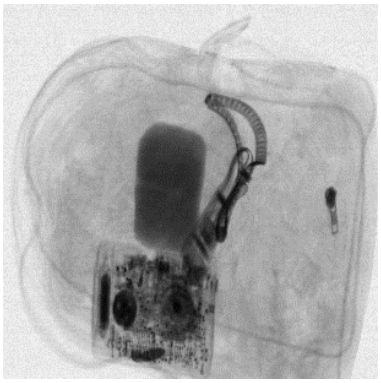

NIIRS = 7.32933
(b)

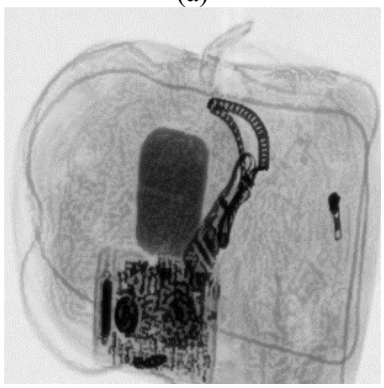

NIIRS = 7.90862
(c)

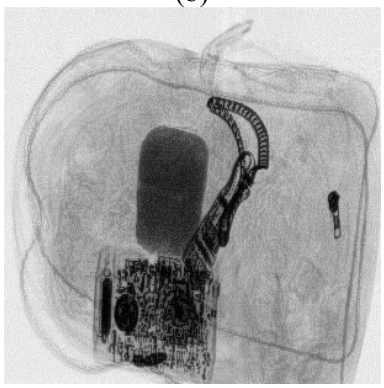

NIIRS = 7.70565
(d)

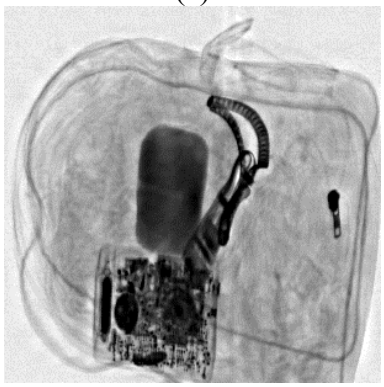

NIIRS = 8.04048
(e)

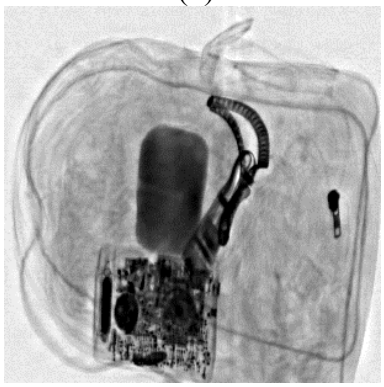

NIIRS = 8.03817
(f)

Figure 6.22 Evaluation results by applying the IQM of Nill et al. to the luggage scene in Figure 6.13. (a) Low-energy image, (b) high-energy image, (c), (d) combined grayscale image and noise-reduced combined version generated using local-spatial-information based fusion algorithm, (e) fused image generated by using the wavelet-based fusion algorithm, and (f) fused image version generated by incorporating a noise-reduction step into the wavelet-based fusion algorithm.

increased after using the two proposed fusion algorithms, which is consistent with our in-house visual evaluation results. When a noise-reduction step is incorporated into the fusion algorithms, the decrease in noise levels also resulted in a little loss of useful information. Comparing the four pairs of NIIRS values of Figures 6.21 (c) and (d), Figures 6.22 (c) and (d), Figures 6.21 (e) and (f), and Figures 6.22 (e) and (f), we see that the NIIRS value of the fused image before noise-reduction is slightly higher than the NIIRS value after noise-reduction. As noise may cause the fused images to exhibit many artificial details and therefore result in inaccurate image interpretation, we suggest to still have the noise reduction step incorporated into the fusion process anyway.

6.6 Summary

Two proposed approaches to dual-energy x-ray luggage image fusion − local spatial information based image fusion and wavelet-based image fusion, are presented in this chapter.

Local spatial information based image fusion classifies each pixel in a luggage scene into either background pixel or detail pixel, and then highlights which represents the features of interest in the luggage scene.

Wavelet based image fusion performs DWT on dual-energy x-ray images, and then processes their approximation coefficients and detail coefficients to produce the fused version. One of the most important features of dual-energy x-ray images is used as a basis of our wavelet based image fusion − distinct objects in a given luggage scene show similar general contours in both the high-energy and low-energy images. Therefore, details, uniquely exhibited in the low or high-energy x-ray images, can be incorporated into the fused version, and details existing in both low and high-energy x-ray images can be more visible in the fused version, through the addition of the detail coefficients of the low-energy and high-energy x-ray images.

The effectiveness of the preceding fusion approaches has been demonstrated by our in-house visual assessment and the use of objective evaluation measures to fused gray-level image versions. In the context of dual-energy x-ray image fusion, comparisons of our fusion approaches with other popular fusion approaches will be performed in further studies.

In addition, a new color-coding scheme for the fused images is presented. Some preliminary color results, produced using this scheme, indicate that this color-coding scheme is a very promising method to color-coded fused images. The next-step study of color-coding will involve the exploration of a powerful automatic segmentation algorithm to segment the difference images and selection of hue sequences that correspond to the segmented classes.

7 Application Software Development

7.1 X-ray Image Processing (XIP)

The objective of the development of the XIP application is to simplify the procedures of processing raw data of x-ray images of carry-on luggage using the image enhancement, image segmentation, and pseudo-coloring techniques presented in the previous chapters. The application will also ease the judging of methods and combinations which are more useful for the identification of potential threats. VC++ is used as the development tool for XIP, because of its versatility in creating friendly GUIs with desirable features and high efficiency in processing images.

A new generation of GUI of XIP is designed and implemented. The GUI shows the original image and the output image simultaneously so that it facilitates the comparison between the two. For the display of the two images, two different modes are provided, a side by side mode and top to bottom mode. When an image is opened, according to the ratio of width to height of the original image, XIP automatically selects an appropriate mode to display the original and resulting images.

As the original images obtained from the x-ray scanner of carry-on luggage are in tiff format, XIP is made to support 8-bit and 16-bit tiff image processing. Using XIP, the user can process an input image with one specific method or a sequence of methods. The satisfactory processed image can be saved as an 8-bit or 16-bit tiff image file, corresponding to the image format of the input image. Figure 7.1 shows the GUI of XIP, which contains an original single-energy image of a given luggage scene (top left), and its corresponding processed images generated by using XIP with one specific algorithm or a series of algorithms.

7.2 Wireless Tablet PC-Based Remote Supervision

The remote supervision system (RSS) is designed to remotely process tough scenes of luggage at the requests of screeners at front-end explosive detection systems (EDS) at airport luggage check points and to remotely check any selected front-end EDS remotely at the requests of the supervisor of back-end supervisory machines which are portable tablet PCs.

The system is implemented based on client-server mode with VC++ on Windows XP. Communication among EDSs, servers and supervisory machines (wireless tablet PCs), is fulfilled through connection-oriented sockets (TCP). Supervisory machines are able to process raw x-ray images loaded from EDSs with selected and designed image

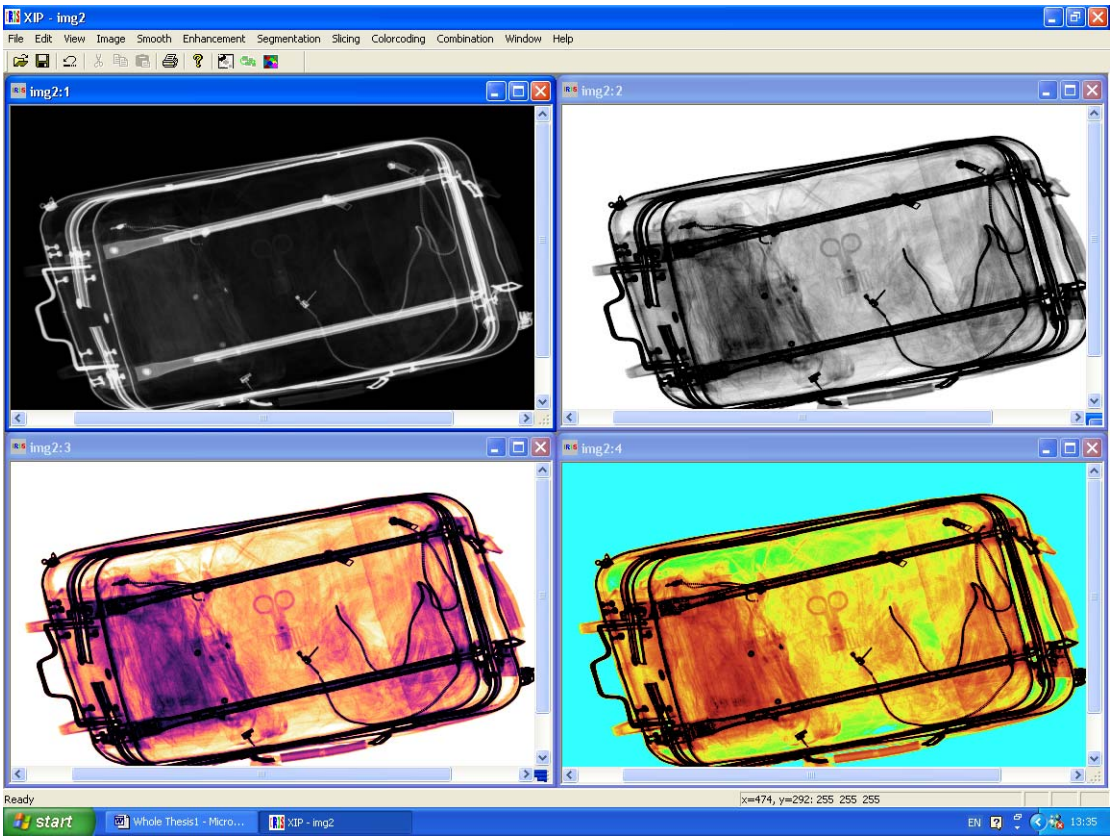

(a)

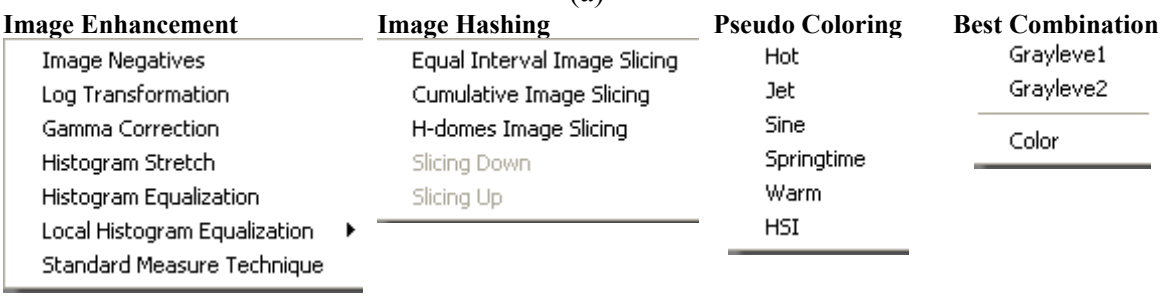

(b)

Figure 7.1 (a) The GUI of XIP, (b) XIP drop-down menus showing image enhancement and visualization algorithms implemented.

processing techniques and send back/save helpful resulting images to assist screeners in threat identification.

7.2.1 Introduction

New approaches have continuously been proposed for airport luggage inspection; however, because of the inherent complication of luggage scenes and the adoption of more sophisticated methods to conceal threat objects, it is close to impossible to have only one single or uniquely combined technique to successfully reveal different kinds of potential threats hidden in x-ray luggage scans. Besides, considering the speed requirement of luggage inspection, it is undesirable to have screeners apply several image processing approaches to every piece of luggage. Therefore, wireless tablet PC based remote supervision system, that can process tough pieces of luggage remotely at the requests of front-end EDSs at airport luggage check points and can remotely check the work of any chosen front-end EDS at the requests of back-end supervisory machines, is proposed as a solution to applying advanced image processing and visualization techniques to airport luggage inspection on need basis.

7.2.2 RSS Framework

RSS is designed based on client-server mode. As Figure 7.2 shows, EDSs reside at the front end of the entire system and are considered as special clients. The server and clients supervising EDSs reside at the back end of the system. For convenience and high efficiency of remote supervision, wireless tablet PCs are actually used as supervisory clients in RSS. In addition, through a set of simple settings, RSS can authorize a supervisor to process the requests of a particular group of screeners who are operating EDSs and also to supervise this group of screeners' work. That is, as illustrated in different colors in Figure 7.2, Client 1 has the authority to process the requests of the group of EDSs marked in pink and supervise their work; Client 2 processes the requests of the group of EDSs marked in white and supervises them, and so on. Advanced x-ray image processing methods are provided for supervisory clients, so tough luggage scans that front-end screeners cannot surely interpret will be interpreted by qualified supervisors via applying advanced x-ray image processing methods.

RSS is developed with VC++ 7.0 on Windows XP, consisting of client-end application and server-end application. Communication among EDSs, server and supervisory machines, namely wireless tablet PC, is fulfilled by using connection-oriented windows sockets (TCP). 8-bit and 16-bit gray-level and color TIFF format images are the image formats supported by RSS.

7.2.3 Communication of Server and Client

As mentioned in previous section, communications between server and client in RSS are implemented using connection-oriented windows sockets (TCP) technology. Socket is an essential network-programming concept. This section is about to introduce such concept, and then present how connection-oriented sockets are established and utilized in a typical client-server system.

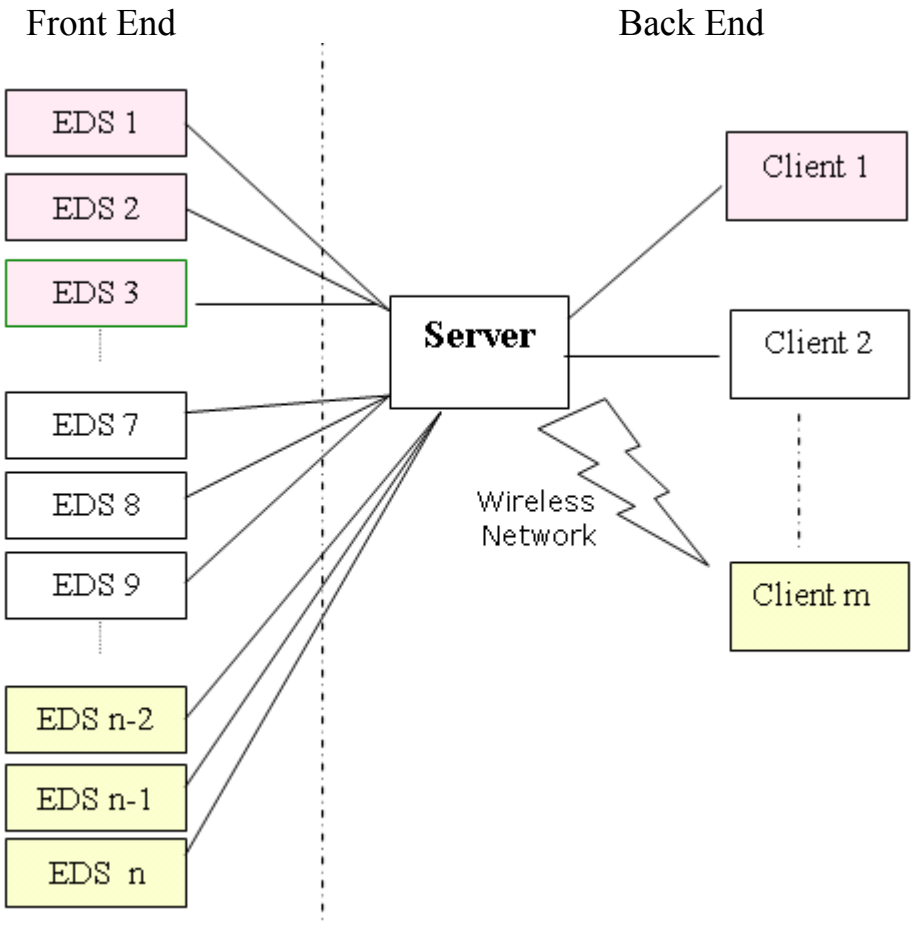

Figure 7.2 Schematic diagram of the Remote Supervision System (RSS).

7.2.3.1 Introduction to Sockets

A socket is a communication endpoint. It enables bidirectional communication between processes located on the same or different machines using standard mechanisms built into network hardware and operating systems [SU, 2004; Wol, 2004]. Commonly, processes residing on different machines rely on Internet for communications; hence, internet addresses, i.e. the familiar IP address, and port numbers (a 16-bit unsigned integer) are used to specify sockets. There are two commonly used types of sockets, datagram sockets and stream sockets. Datagram sockets use the datagram protocol (UTP) that provides unreliable transfer of data to communicate between client and server processes; Stream sockets, also called connection-oriented sockets, use the Transmission Control Protocol (TCP) that provides reliable, transfer for data to communicate.

7.2.3.2 Client/Server System

In a client-server system, the way a socket is used determines a process as either a client-end process or a server-end process. A server-end process establishes a socket with a known, or published, address, waits for incoming connections and presumably provides some service to client-end processes. In contrast, a client-end process creates an unnamed socket, connects to a server, usually to ask a server-end process to do something. Figure 7.3 shows how a typical interaction between a client and a server is performed using connection-oriented sockets.

7.2.4 RSS Functions

RSS functions can be grouped into three categories, client-server communication, image processing algorithms, and image access and display operations.

7.2.4.1 Client-Server Communication

Two kinds of data, image data and auxiliary data, are transferred between client and server. Auxiliary data helps the server application or client application know what it should do — for example, send an image or receive an image, and assist server application in identifying users, recording operation histories, and so on. For the transmission of an image, image data are disassembled two components, property information and pixels' value information. Property information includes such parameters as image size, pixel type and the total number of channels of the image. After correctly receiving property information and pixels' value information of an image, the two components are reassembled together at the receiving end.

Assume that the luggage image that an EDS requests for a supervisory machines to process has been stored on the server. Figures 7.4 and 7.5 give the flows on how to load an image from the server and how to send the processed image version back to the server in RSS.

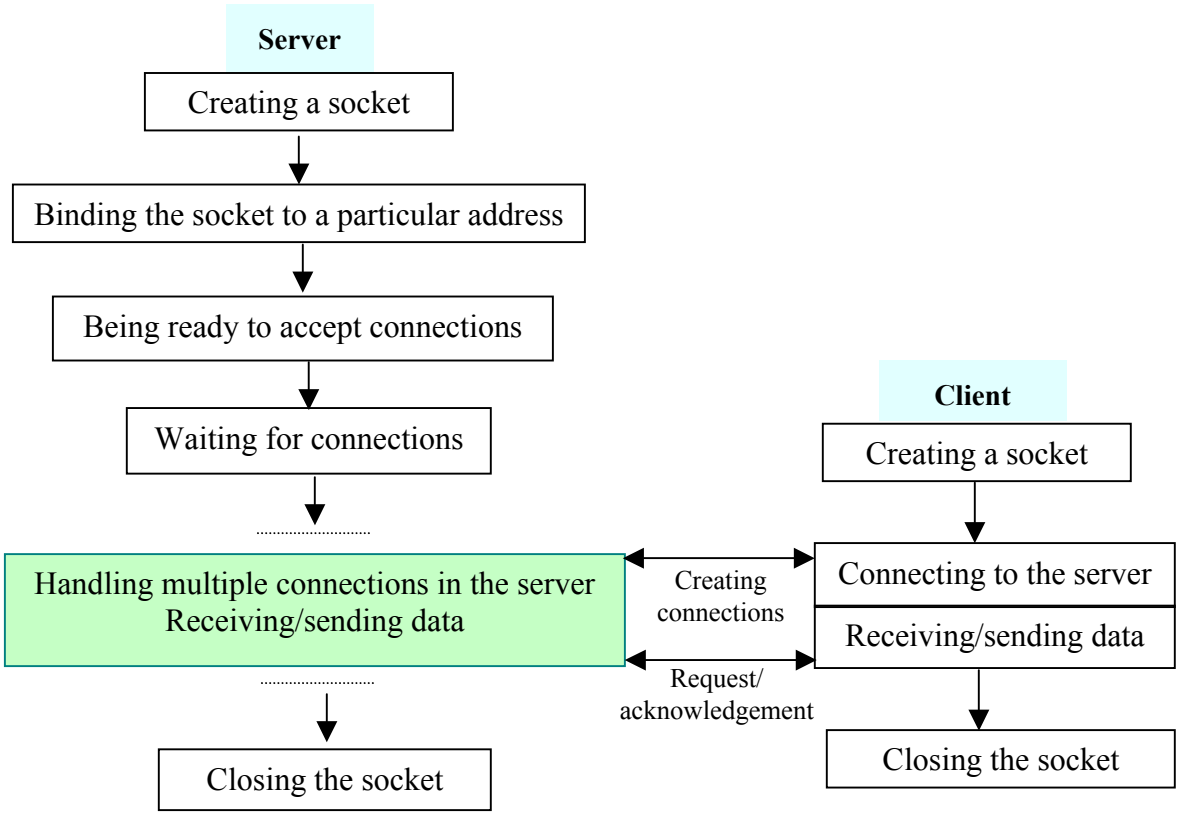

Figure 7.3 A typical interaction between a client and a server using connection-oriented sockets.

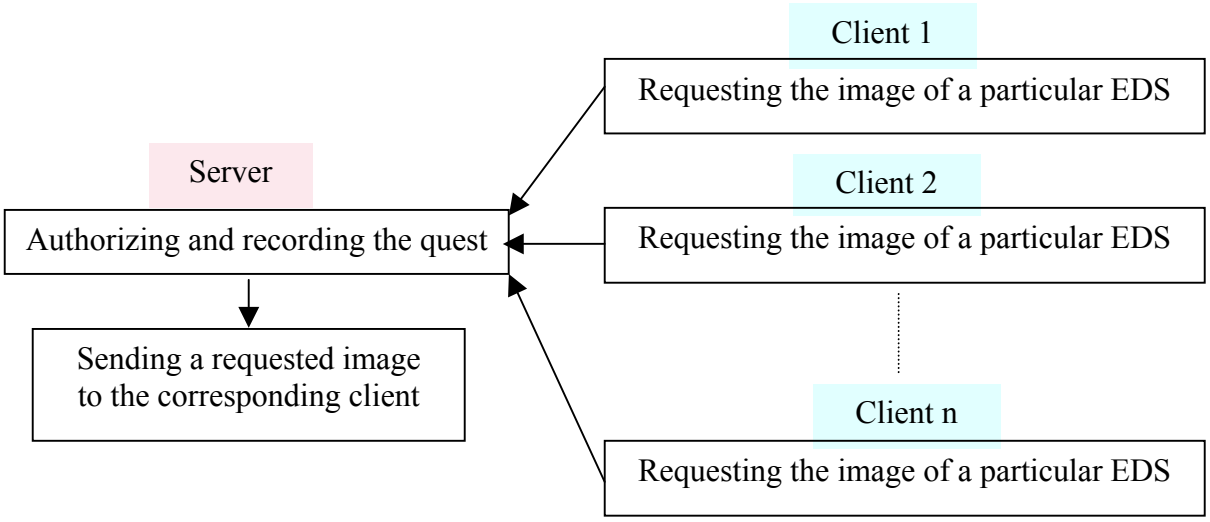

Figure 7.4 Flow of loading an image from the server.

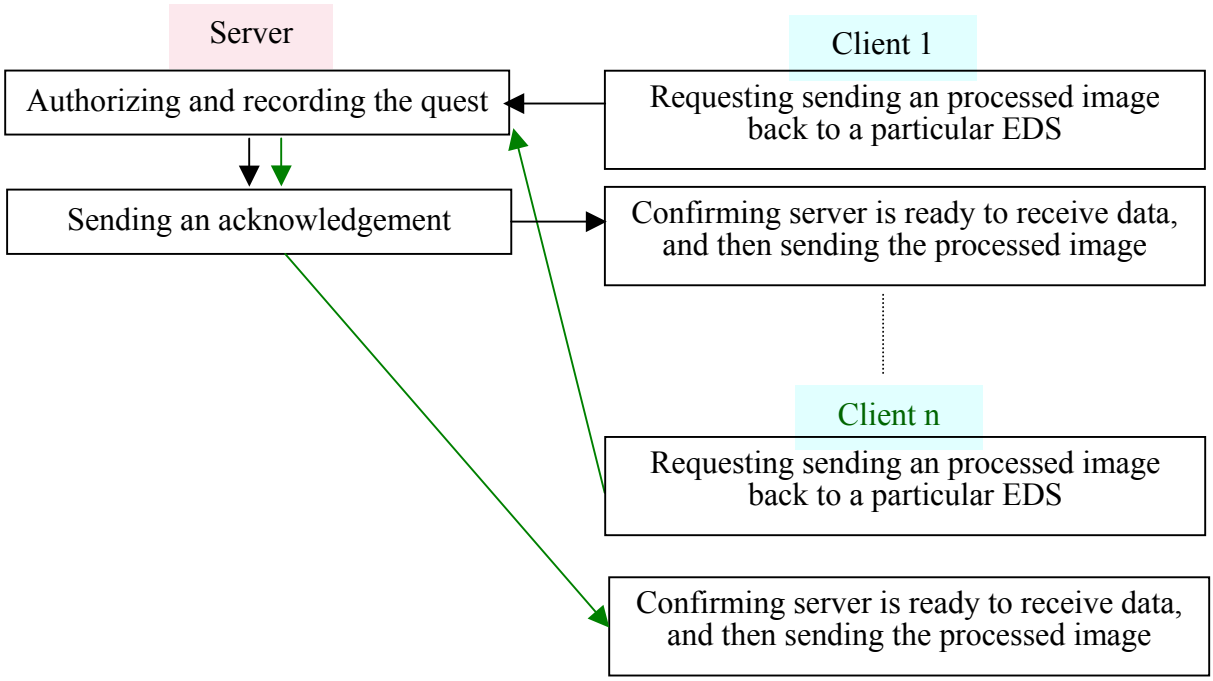

Figure 7.5 Flow of sending a processed image version back to the server.

7.2.4.2 Image Processing Algorithms

The client-end application used for the supervisory Tablet PCs provides image processing approaches to further process tough x-ray luggage scans. Techniques, on image enhancement, image segmentation, pseudo coloring and image fusion, that have been explored/proposed in our research and show effectiveness in visualizing different objects in luggage, especially potential threats, are incorporated in this application.

7.2.4.3 Image Access and Display

Local image access enables the client-end application used for supervisory machines to not only access images remotely but also to open local images, process them and save them locally.

7.2.5 RSS GUIs

RSS GUIs consist of the GUIs of client-end and server-end application. The server-end application can record and show requests from any clients. The client-end application, as shown in Figure 7.6, displays the original image and its corresponding processed version simultaneously for convenient comparison.

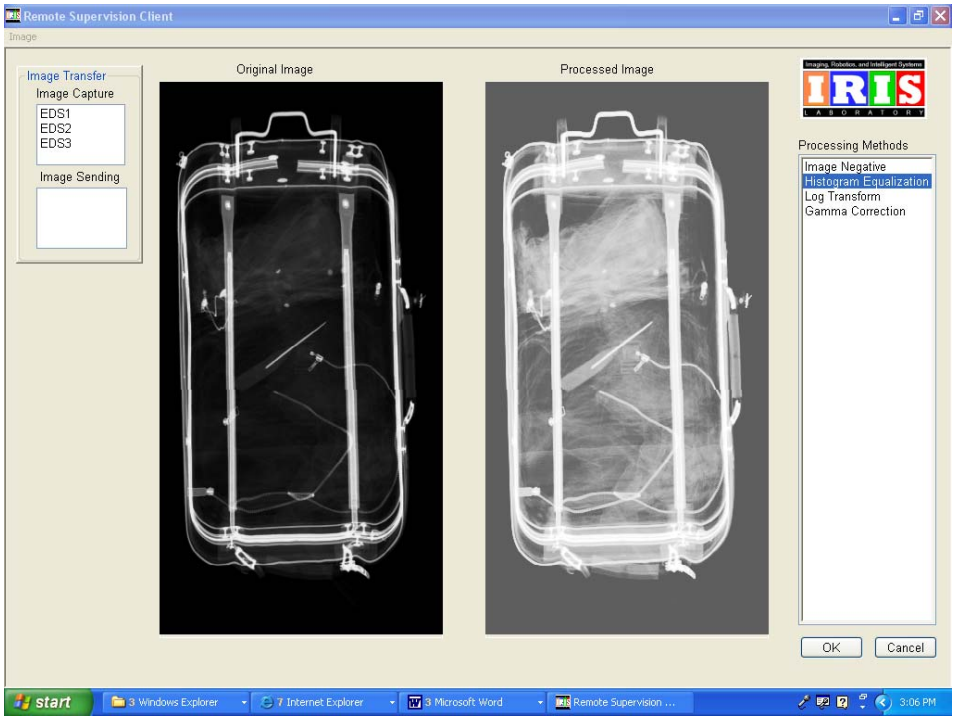

Figure 7.6 GUI of the client-end application.

8 Conclusions

In this thesis, we have presented several different aspects of improvement of airport carry-on luggage inspection using image processing and visualization technologies. Figure 8.1 graphically summarizes the main procedure we used to process single-energy x-ray images and dual -energy x-ray images.

8.1 Summary of Contributions

The primary contribution of our research as presented in this thesis includes the identification of optimized combinations of common segmentation and enhancement methods, HSI based color- coding methods and two dual-energy image fusion algorithms—local spatial information based image fusion and wavelet based image fusion.

Optimum combinations of common segmentation and enhancement methods: Several combinations of selected common image segmentation and enhancement methods were designed and applied to single-energy x-ray images. Two combinations, *logarithm transform* + *contrast stretching* and *image negative* + *hdome* + *contrast stretching*, are particularly effective in enhancing single-energy x-ray luggage images.

HSI based color-coding methods: A color scale called "Springtime" is designed to convey both value and shape information. This scale decreases the perceptual artifacts of the human visual system in general and simultaneous contrast in particular Additionally, constant saturation and variable saturation schemes based on the HSI model are proposed to color to preprocessed gray scale data, while decreasing the perceptual artifacts of the human visual system.

Dual-energy image fusion algorithms:
Local spatial information-based image fusion: The approach is based on classifying each pixel in the luggage scene into either background pixel or detail pixel, and then highlighting detail pixels based on the fact that detail pixels carry the main features of interest in the luggage scene.

Wavelet-based image fusion: One of the most important features of dual-energy x-ray images is used as a basis of the wavelet based image fusion; Distinct objects in a given luggage scene show similar general contours in both high-energy and low-energy images. This algorithm incorporates details, uniquely exhibited by the low-energy or high-energy

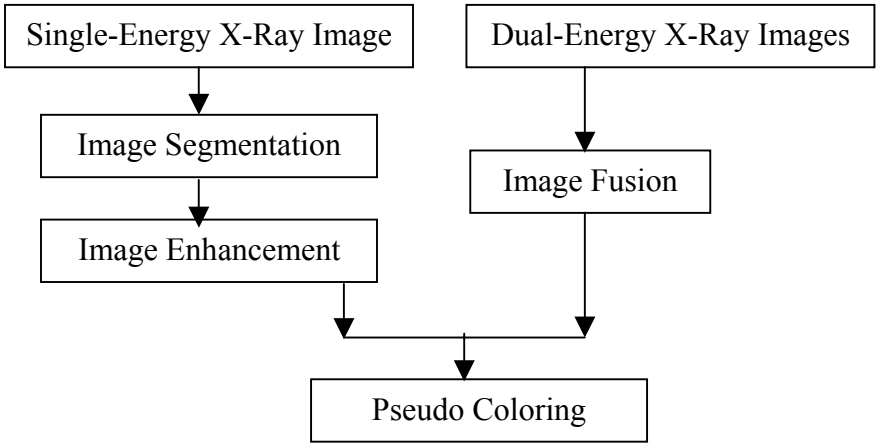

Figure 8.1 Main procedure used to process single-energy and dual-energy x-ray images.

x-ray image into the fused version, as well as details existing in both low-energy and high-energy x-ray images.

For each of these algorithms, qualitative and quantitative results have been presented to demonstrate their effectiveness in improving x-ray luggage images.

8.2 Future Work

Extensions to this work may involve the following: (1) More extensive testing the preceding algorithms in airports to acquire a more comprehensive feedback and to prompt further improvement of these algorithms; (2) Further exploration of objective image quality measures. Few existing image quality measures are widely accepted for the evaluation of enhanced x-ray images, although many image quality measures have been proposed. Therefore, to provide more reliable evaluation results and decrease the overhead of human assessments, objective image quality measures that correlate acceptably well with the perceived image quality are to be sought.

BIBLIOGRAPHY

[Abidi et al., 2004] B. Abidi, M. Mitckes, J. Liang, and M. Abidi, "Improving the detection of low density weapons in x-ray luggage scans using image enhancement and novel scene de-cluttering techniques," Journal of Electronic Imaging, Vol. 13, Issue 3, pp. 523-538, July 2004.

[Adobe] www.adobe.com/support/techguides/color/colormodels

[Besag, 1986] J. Besag, "On Statistical Analysis of Dirty Pictures," Journal of the Royal Statistical Society 48, No. 3, pp. 259-302, 1986.

[Billmeyer et al., 1981] F. W. Billmeyer and M. Saltzman, Principles of Color Technology, John Wiley & Sons (2nd edition), April 1981.

[Brown] T. J. Brown, An adaptive Strategy for Wavelet Based Image Enhancement.

[Butler et al, 2002] V. Butler and R. W. Poole, Jr., "Re-Thinking Checked-Baggage Screening," Policy Study No. 297, Reason Public Policy Institute, July 2002.

[Chang et al, 2002] Y. Chang, A.M.N. Fu, H. Yan, "A Hierarchical Approach in Multilevel Thresholding Based on Maximum Entropy and Bayes' Formula," Conferences in Research and Practice in Information Technology, Sydney, Australia, Vol. 11, 2002.

[Chang et al., 1994] C. Chang, K. Chen, J. Wang, M.L.G. Althouse, "A Relative Entropy-Based Approach to Image Thresholding," Pattern Recognition, Vol. 27, No. 9, pp. 1275-1289, 1994.

[Clark and Leonard, 1989] F.J. Clarke and J.K. Leonard, "Proposal for a Standardized Continuous Pseudocolor Spectrum with Optimal Visual Contrast and Resolution," Third International Conference on Image Processing and its Applications, pp. 687-691, 1989.

[Czerwinski et al., 1999] R. N. Czerwinski, D. L. Jones, and W. D. O'Brien, Jr., "Detection of Lines and Boundaries in Speckle Images - Application to Medical Ultrasound," *IEEE*

Transactions on Medical Imaging 18, No 2, pp. 126-136, February, 1999.

[Dai and Zhou, 1996] J. Dai and S. Zhou, "Computer Aided Pseudo-color Coding of Gray Image: Complementary Color Coding Technique," *Proceedings of the SPIE, The International Society for Optical Engineering*, Vol. 2898, pp. 186-191, 1996.

[Elbadawy et al, 1998] O. Elbadawy, M.R El-Sakka, M.S. Kamel, "An Information Theoretic Image-Quality Measure ," IEEE Canadian Conference on Electrical and Computer Engineering, Vol. 1, pp.169 – 172, 24-28 May 1998.

[Gonzalez and Woods, 2002] R. C. Gonzalez and R. E. Woods, Digital Image Processing, Prentice Hall (Second Edition), 2002.

[Guide, 1998] http://www.fas.org/irp/imint/niirs_c/guide.htm

[Hadhoud, 2001] M. M. Hadhoud, "X-Ray Images Enhancement Using Human Visual System Model Properties and Adaptive Filters," IEEE International Conference Proceedings on Acoustics, Speech, and Signal Processing (ICASSP '01), Vol.3, pp 2005 – 2008, May 2001.

[Hassanien and Bader, 2003] A. E. Hassanien, A. Bader, "A comparative study on digital mamography Enhancement algorithms based on Fuzzy Theory," International Journal of Studies in Informatics and Control, Vol.12, No. 1, pp. 21-31, SIC 2003.

[Healey, 1996] C. G. Healey, "Choosing Effective Colours for Data Visualization", IEEE Visualization Proceedings, pp. 263-270, October 1996.

[Heimann, 2004] Heimann Systems: www.heimannsystems.com

[HyperPhysics] hyperphysics.phy-astr.gsu.edu/hbase/vision/cie.html.

[Jain, 1991] A.K. Jain, "Fundamentals of Digital Image Processing," Englewood Cliffs, NJ, Prentice-Hall, 1991.

[Kapur and Wong, 1985] J.N. Kapur, A.K.C. Wong, "A New Method for Grey-Level Picture Thresholding Using the Entropy of the Histogram," Computer Graphics, Vision and Image Processing, Vol. 29, pp. 273-285, 1985.

[Kinape and Amorim, 2003] R.M. Kinape, M.F. Amorim, "A Study of the Most Important Image Quality Measures," Proceedings of the 25th Annual International Conference of the IEEE on Engineering in Medicine and Biology Society, Vol. 1, pp. 934 – 936,17-21 Sept. 2003.

[Lee and Wang, 1999] S.C. Lee, Yiming Wang, "Automatic Retinal Image Quality Assessment and Enhancement," Proc. of SPIE Vol. 3661, pp. 1581-1590, Medical Imaging: Image Processing, 1999.

[Lehmann et al., 1997] T.M. Lehmann, A. Kaser, R Repges, " A Simple Parametric Equation for Pseudocoloring Grey Scale Images Keeping their Original Brightness Progression," Image and Vision Computing, 15(3) pp. 251-257, 1997.

[Levkowitz and Herman, 1992] H. Levkowitz and G. Herman, "Color Scales for Image Data," IEEE Computer Graphics and Application, pp. 72-80, 1992.

[Levkowitz, 1988] H. Levkowitz, "Color in computer graphic representation of two-dimensional parameter distributions," Ph. D. Dissertation, Department of Computer and Information Science, University of Pennsylvania, Dec. 1988.

[Lewis et al, 2004] J.J. Lewis, R.J. O'Callaghan, S.G. Nikolov, D.R. Bull, C.N. Canagarajah, "Region-Based Image Fusion Using Complex Wavelets," The 7th International Conference on Information Fusion, pp. 555-562, June, 2004.

[Li et al, 1995] H. Li, B. S. Manjunath, S. K. Mitra, "Multisensor: Image Fusion Using the Wavelet Transform," Graphical Models and Image Processing, Vol. 57, pp 235-245, May 1995.

[Lin, 2001] K.C. Lin, "Fast Thresholding Computation by Searching for Zero Derivatives of Image Beteen-Class Variance," IECON'01: The 27th Annual Conference of the IEEE Industrial Electronics Society, Vol. 1, pp. 393 -397, 29 Nov.- 2 Dec., 2001.

[Lubbe, 1997] J. van der Lubbe, Information Theory, Cambridge University Press, UK, 1997.

[Luo and Tian, 2000] X. Luo, J. Tian, "Multi-Level Thresholding: Maximum Entropy Approach Using ICM," Proceedings of 15th International Conference on Pattern Recognition, Vol. 3, pp. 778 -781, Sept. 2000.

[MacDonald, 1999] L. W. MacDonald, "Using Color Effectively in Computer Graphics," IEEE Computer Graphics and Applications 19, No. 4, pp. 20-35, July-Aug. 1999.

[Mathworks, 1994] www.mathworks.com/access/helpdesk/help/toolbox/wavelet/wavelet.html

[Moore and Fitz, 1993] P. Moore, C. Fitz, "Gestalt theory and instructional design," Journal of Technical Writing and Communication 23, No. 2, pp. 137-157, 1993.

[Munteanu and Rosa, 2004] C. Munteanu, A Rosa, "Gray-Scale Image Enhancement as an Automatic Process Driven by Evolution," IEEE Transactions on Systems, Man and Cybernetics, Part B, Vol. 34, No. 2, pp.1292 – 1298, April 2004.

[Murch, 1984] G. M. Murch, "Physiological Principles for the Effective Use of Color," IEEE Computer Graphics and Applications, Vol. 4, No. 11, pp. 49-54, November 1984.

[NIIRS, 1998] http://www.fas.org/irp/imint/niirs.htm

[Nill and Bouzas, 1992] N.B. Nill, B.H. Bouzas, "Objecive Image Quality Measure Derived from Digital Image Power Spectra," Optical Engineering, Vol. 31, No. 4, pp. 813-825, April 1992.

[Ouerhani et al., 2004] N. Ouerhani, R. Wartburg, H. Hugli, R. Muri, "Empirical Validation of the Saliency-based Model of Visual Attention," Electronics Letters on Computer Vision and Image Analysis, Vol. 3, No. 1, pp.13-24, 2004.

[Pal and Pal, 1989] N. R. Pal, S. K. Pal, "Entropic Thresholding," Signal Processing, Vol. 16, pp. 97-108, 1989.

[Piella, 2003] G. Piella, "A general framework for multiresolution image fusion: from pixels to regions," Information Fusion, Vol. 4, No. 4, pp. 259-280(22), December 2003.

[Piella, 2004] G. Piella, "New Quality Measures for Image Fusion," The 7th International Conference on Information Fusion, pp. 542-546, June 28 to July 1, 2004.

[Pizer et al., 1982] S.M. Pizer, J.B. Zimmerman, R.E. Johnston, "Contrast Transmission in Medical Image Display," Proceedings of the 1st International Symposium on Medical Imaging and Interpretation, pp. 2-9, Oct. 1982.

[Plataniotis et al., 2000] K. N. Plataniotis and A. N. Venetlanopoulos, Color Image Processing and Applications, Springer, 2000.

[Pratt, 2000] W.K. Pratt, Digital Image Processing, New York, Wiley, 2000.

[Pun, 1980] T. Pun, "A New Method for Grey-Level Picture Thresholding Using the Entropy of the Histogram," Signal Processing, Vol. 2, pp.223-237, 1980.

[Rockinger and Fechner, 1998] O. Rockinger, T. Fechner, "Pixel-level Image Fusion: the Case of Image Sequenced," Proceedings of the SPIE, Vol. 3374, pp. 378-388, 1998.

[Rudaz et al., 1997] N. Rudaz, R. D. Hersch, V. Ostromoukhov, "Specifying color differences in a linear color space (LEF)," Proceedings of the Fifth Color Imaging Conference: Color Science, Systems and Applications, Scottsdale, 1997.

[Sankur and Sezgin, 2001] B. Sankur, M. Sezgin, "Image Thresholding Techniques: A Survey over Categories."

[Shao and Chen, 2001] Y. C. Shao, L. C. Chen, "Object segmentation in elevation space using mathematical morphology," Proceedings of the 22d Asian Conf. on Remote Sensing, Singapore, pp. 227-232, 2001.

[Shi et al., 2002] X. Q. Shi, P. Sallstrom, and U. Welander, "A Color Coding Method for Radiographic Images," Image and Vision Computing Vol. 20, pp.761-767, 2002.

[Singh and Singh, 2003] S. Singh, M. Singh, "Review Explosives Detection Systems (EDS) for Aviation Security," Signal Processing, pp 31-55, Vol. 83, 2003.

[Sobania, 1999] www.eee.ntu.ac.uk/research/vision/asobania

[SU, 2004] compnetworking.about.com/library/weekly /aa083100a.htm, Strayer University.

[Taylor and Murch, 1986] J. M. Taylor, G. M. Murch, "The Effective Use of Color in Visual Displays: Text and Graphics Applications", Color Research and Applications 11, pp. S3-10, Supplement 1986.

[Thompson, 1995] E. Thompson, Color Vision, "a Study in Cognitive Science and Philosophy of Perception," Routledge, 1995.

[Unser and Aldrouri, 1996] M.Unser, A. Aldrouri, "A Review of Wavelets in Biomedical Application," Proceedings of the IEEE, Vol. 84, No. 4, April 1996.

[Vincent, 1993] L. Vincent, "Morphological Grayscale Reconstruction in Image Analysis: Applications and Efficient Algorithms," IEEE Trans. on Image Processing, Vol. 2, No. 2, pp.176-201, 1993.

[Ware, 1988] C. Ware, "Color Sequences for Univariate Maps: Theory, Experiments and Principles," Computer Graphics and Application 18, pp. 41-49, 1988.

[Wei et al., 1997] G. Q. Wei, K. Arbter, and G. Hirzinger, "Automatic Tracking of Laproscopic Instruments by Color

Coding," Lecture Notes in Computer Science 1205, Aug. 1997.

[Wol, 2004] www.csis.gvsu.edu/~wolffe/socketTutorial.html

[Wright, 1997] P. Wright, D. Mosser-Wooley, B. Wooley, "Techniques & Tools for Using Color in Computer Interface Design," ACM CrossRoads, Spring 1997.

[Xue et al, 2002] Z. Xue, R. S. Blum and Y. Li, "Fusion of visual and IR images for concealed weapon detection," invited paper at International Conference on Information Fusion, Annapolis, Maryland, July 2002.

[Xydeas and Petrovic, 2000] C. Xydeas and V. Petrovic, "Objective Pixel-Level Image Fusion Performance Measure," Proceedings of SPIE, Vol. 4051, pp. 89-99, April 2000.

[Zhang and Blum, 1997] Z. Zhang, R. S. Blum, "Multisensor Image Fusion using a Region-Based Wavelet Transform Approach," Proceedings of the DARPA IUW, pp. 1447-1451, 1997.

Vita

Yue Zheng received her B.S. in July 1993 from Capital Normal University, Beijing, China, majored in computer science. She joined computing center of Beijing Foreign Studies University as a lecture and software developer in 1993. In 1998, she began her graduate study at the Department of Computer Science and Technology of Tsinghua University, Beijing, China.

Yue Zheng enrolled in Master's program in the Department of Electrical and Computer Engineering at University of Tennessee, Knoxville, TN, in 2003. She joined Imaging, Robotics, and Intelligent Systems Laboratory (IRIS) as a graduate research assistant, working on x-ray image processing and visualization. She will graduate with a M.S. in electrical engineering from the University of Tennessee in Dec. 2004.